ENHANCEMENT AND PREDICTION OF LONG-TERM ACID FRACTURE CONDUCTIVITY

BY

Mahmoud Hassan Desouky

A Thesis Presented to the
DEANSHIP OF GRADUATE STUDIES

KING FAHD UNIVERSITY OF PETROLEUM & MINERALS
DHAHRAN, SAUDI ARABIA

In Partial Fulfillment of the
Requirements for the Degree of

MASTER OF SCIENCE

In

PETROLEUM ENGINEERING

December 2019

KING FAHD UNIVERSITY OF PETROLEUM & MINERALS
DHAHRAN- 31261, SAUDI ARABIA
DEANSHIP OF GRADUATE STUDIES

This thesis, written by **MAHMOUD HASSAN DESOUKY** under the direction of his thesis advisor and approved by his thesis committee, has been presented and accepted by the Dean of Graduate Studies, in partial fulfillment of the requirements for the degree of **MASTER OF SCIENCE IN PETROLEUM ENGINEERING.**

Dr. Dhafer Al-Shehri
(Department Chairman)

Dr. Murtada Al-Jawad
(Advisor)

Dr. Salam A. Zummo
Dean of Graduate Studies

Dr. Theis Solling
(Member)

18\12\19
Date

Dr. Dhafer Al-Shehri
(Member)

“All that I am or ever hope to be, I owe to my angel mother.”

Abraham Lincoln

ACKNOWLEDGMENT

I owe my advisor ***Dr. Murtada Al-Jawad*** *with every single word in my thesis for his endless support, guidance and encouragement from day one of this research. Dr. Al-Jawad paved the way for me to get this work done and facilitated difficulties that arose while this research was proceeding.*

I am grateful to my committee member ***Dr. Theis Solling*** *for his second to none commitment, innovation and ability to solve intricate problems. I am also grateful to my committee member* ***Dr. Dhafer Al-Shehri*** *for his encouragement and support throughout the degree program.*

Sincere gratitude goes to ***Dr. Abduljamiu Amao*** *for his invaluable efforts, perpetual help and providing deep insights into theoretical concepts. I would like to appreciate* ***Dr. Khalid Al-Ramadan*** *for his spirit which inspired me.*

I would also like to thank the labs' heroes ***Mr. Eassa Abdullah****,* ***Mr. Bandar Al-Otibi****,* ***Mr. Abdullah Al-Qubalee*** *and* ***Mr. Habeeb Al-Abbas*** *for their technical assistance and guidance as needed during the experimental work.*

*Finally, I would like to thank King Fahd University of Petroleum & Minerals (****KFUPM****) and the College of Petroleum and Geosciences (****CPG****) for providing this scholarship.*

TABLE OF CONTENTS

LIST OF TABLES

LIST OF FIGURES

LIST OF ABBREVIATIONS

API	:	American Petroleum Institute
CC	:	Correlation Coefficient
ECOC	:	Error-Correcting Output Codes
EDS	:	Energy-dispersive X-ray spectroscopy
GPR	:	Gaussian Process Regression
LASSO	:	Least Absolute Shrinkage and Selection Operator
MSE	:	Mean Squared Error
NMR	:	Nuclear Magnetic Resonance
QEMSCAN	:	Quantitative Evaluation of Minerals by Scanning Electron Microscopy
R	:	Correlation Coefficient
RH	:	Relative Humidity
SEM	:	Scanning Electron Microscopy
XRD	:	X Ray diffraction
XRF	:	X Ray Florescence

ABSTRACT

Full Name : Mahmoud Hassan Desouky
Thesis Title : Enhancement and Prediction of Long-Term Acid Fracture Conductivity
Major Field : Petroleum Engineering
Date of Degree : December 2019

Acid fracturing is a widely used stimulation method in carbonate reservoirs that can enhance the production rate and ultimate recovery considerably. The reaction between the acid and fracture surface generates un-even surfaces due to rock heterogeneity. Asperities prop the fracture open after closure, leaving conductive flow paths. The created conductivity is governed by rock hardness, etching pattern and magnitude of closure stress which increases with reservoir depletion. Recent studies showed that the acid/rock reaction weakens the rock mechanical properties resulting in a sharp fracture conductivity decline. The research aims to restore the rock strength to endure high stresses and to sustain long-term fracture conductivity either by consolidation or mineralogy alteration. The restoration treatment was carried out by full immersion or impregnation of samples and the hardness was assessed before and after the treatment by a nondestructive technique. Nanocrystal solutions and Tetraethyl orthosilicate (TEOS) are consolidating agents which were employed to raise the rock hardness by 6% up to 19%. On the other hand, zinc sulfate was used to change the calcite into the harder mineral, smithsonite, which resulted in a 35% increase in rock hardness. The permeability of the samples treated with nanocrystal and zinc sulfate solutions suffered from a reduction in permeability by 45% up to 65%, whereas those treated with TEOS showed no reduction.

The other objective of this work was to implement machine learning tools to improve acid fracture conductivity prediction considering both rock type and etching patterns; an approach that was not considered previously. A literature review was conducted to collect consistent acid fracture conductivity data. Based on the rock type and treatment conditions, adequately trained multiclass error-correcting output codes (ECOC) model using decision tree learner was used to forecast the etching pattern with an accuracy of 95%. Multivariate linear regression with regularization was used to predict the fracture conductivity. As they usually develop roughness etching pattern, chalk and dolomite conductivities were predicted accurately with normalized mean squared errors (MSE) of 0.364 & 0.037 and correlation coefficients (CC) near 90% & 95%, respectively. Limestone requires less data conditioning and more what-if scenarios as it develops different etching patterns. Thus, its normalized MSE is higher than that of chalk and dolomite with a value of 0.555 and CC around 90%. It is found that acid fracture conductivity classification based on rock type and etching pattern improved the prediction accuracy of the fracture conductivity.

ملخص الرسالة

الاسم الكامل:محمود حسن دسوقي

عنوان الرسالة: تحسين وتنبؤ توصيلية التكسير بالحمض طويلة المدي

التخصص: هندسة البترول

تاريخ الدرجة العلمية: ديسمبر ٢٠١٩

التكسير بالحمض طريقة لتحسين الإنتاج وتستخدم بشكل واسع في خزانات الكربونات وبمقدورها تحسين معدل الإنتاج والعائد الأقصي كثيراً. التفاعل بين الحمض وسطح الكسر يولد سطحاً غير مستوياً نتيجة عدم تجانس الصخر. تُبقي السنون المدببة الكسر مفتوحاً بعد تطبيق إجهاد الغلق ويترك مساراً موصلاً للتدفق. التوصيلية الناشئة محكومة بصلابة الصخر، شكل التآكل وإجهاد الغلق المؤثر والذي يزيد بنضوب الخزان. دراسات حديثة أظهرت أن تفاعل الحمض والصخر يضعف خواص الصخور الميكانيكية وبالتالي تقل توصيلية الكسر بشكل حاد. يهدف البحث إلي استعادة صلابة الصخر ليتحمل إجهاداً أكبر وينتج توصيلية طويلة المدي إما بالدمج أو التغيير المعدني. معالجة الاستعادة إما بالغمر تماماً أو تشبيع العينات و قُيَمت الصلابة قبل وبعد المعالجة بتقنية غير مدمرة. محاليل الكريستالات النانوية ورباعي إيثيل أورثوسيليكات هما عناصر الدمج المستخدمة لزيادة صلابة الصخر بنسبة ٦ حتي ١٩٪. ومن ناحية أخري استخدم سلفات الزنك لتغيير الكالسيت للمعدن الأصلب السميثسونايت وأظهرت النتائج زيادة في الصلابة حتي ٣٥٪ من القيمة الأصلية. عانت نفاذية العينات المعالجة بمحلول الكريستالات النانوية وسلفات الزنك من نقص بمقدار ٤٥ لى ٦٥٪ بينما تلك المعالجة بتترا إيثيل أورثوسيليكات لم تظهرنقصاً.

الهدف الآخر من هذا العمل هو تطبيق تقنيات تعلم الآلة التقليدية لتحسين تنبؤ توصيلية التكسير بالحمض أخذاً في الإعتبار كلاً من نوع الصخر وشكل التآكل وتلك طريقة لم تستخدم سابقاً. مراجعة الأبحاث تمت لتجميع بيانات توصيلية التكسير بالحمض المتناسقة. اعتماداً علي نوع الصخر وظروف المعالجة، أكواد ناتج تصحيح الخطأ بشجرة القرارات المدربة بشكل كافٍ لديها القدرة علي تنبؤ شكل التآكل بدقة تصل إلي ٩٥٪. بشكل أساسي، استخدم الانحدار الخطي متعدد المتغيرات مع الضبط لتنبؤ توصيلية الكسر. كما هي العادة في الصخر الطباشيري والدولومايت في إنتاج سطح تآكل خشن، فإن توصيليتهم تم التنبؤ بها بسهولة بمتوسط خطأ تربيعي٣٦٤, و ٠٣٧, ومعاملات ارتباط ٩٠٪ و٩٥٪

علي الترتيب. حجر الجير يتطلب تكييف البيانات بشكل أقل وسيناريوهات ماذا لو بشكل أكثر لأنه ينتج كل أشكال التآكل. وهكذا، فإن متوسط الخطأ التربيعي له أكبر من الصخر الطباشيري والدولومايت بقيمة ٠,٥٥٥ ومعامل ارتباط ٩٠٪. وُجد أن تقسيم توصيلية التكسير بالحمض اعتماداً علي نوع الصخر وشكل التآكل قد حسن دقة التنبؤ بتوصيلية الكسر.

CHAPTER 1

INTRODUCTION

1.1 Stimulation Methods and Resulted in Conductivity

Various stimulation methods are utilized to enhance the production rate and ultimate recovery from carbonate reservoirs which can be categorized based on the main constituent as limestone, dolomite, and chalk. Due to carbonates acid-solubility, acid injection below the formation breakdown pressure generates wormholes that can bypass the near wellbore damage and improve the productivity, and this refers to matrix acidizing. On the other hand, fracturing happens when the treatment pressure exceeds the formation breakdown pressure. The minimum horizontal stress tends to close the resulting fractures upon pumping cessation. The mechanism to keep the fracture open differs depending on formation conditions and properties.

In the case of the high temperature deep homogeneous formation, propped fracturing is favoured. Inert fluid loaded with proppant is injected to create a long and deep fracture and the settled proppant keeps a conductive pathway for fluids to flow from the reservoir into the well. Alternatively, acid fracturing is preferred in low-temperature, naturally fractured, and heterogeneous formations. The pumped acid initiates a hydraulic fracture which might also activate natural fractures due to acid reactivity. Heterogeneity results in uneven surfaces when after closure leaving a conductive pathway from the formation to the wellbore (Williams et al., 1979; Asadollahpour et al., 2018). The undissolved regions prop the fracture open against the closure stress after releasing the treatment pressure.

The ability of the fracture to deliver fluids is referred to as conductivity which decreases with the increase in formation closure stress. A successful fracture job results in sufficient durable conductivity under the formation closure stresses. To get such sustainable conductivity, the propped acid fracture was proposed to combine both propped and acid fracturing features (Jeon et al., 2016; Karadkar et al., 2016). Nevertheless, there is no sufficient production history to assure that (Smith et al., 2018).

The conductivity decline is sharp at the beginning then decreases gradually with time. Figure 1 shows the conductivity decline comparison between acid and acid propped fractures at different closure stresses. At low stresses, the acid fracture outperforms acid propped fracture, but at high stresses, the asperities fail to support the closure stress as proppant. Thus, the acid propped fracture conductivity is higher than that of acid fracture. Figure 2 shows the conductivity decline comparison between propped and acid propped fractures at different stresses. At any stress, the propped fracture conductivity is higher than acid propped fracture (Zhang et al., 2018).

The decline rate of conductivity under closure stress varies from fracturing method to another (Suleimenova 2016). The mechanical properties of fracture surfaces after treatment directly impact the decline rate (Cooke, 1975; Bartko et al., 2003; Garrouch and Jennings, 2017; Zhong et al., 2018; Jafarpour et al., 2019). The proppant contact area with the fracture faces in proppant fracturing is larger than the asperities from acid fracturing. Thus, the load on a single proppant grain is less than that on an asperity of an acid fracture. Therefore, proppant usually sustain better fracture conductivity.

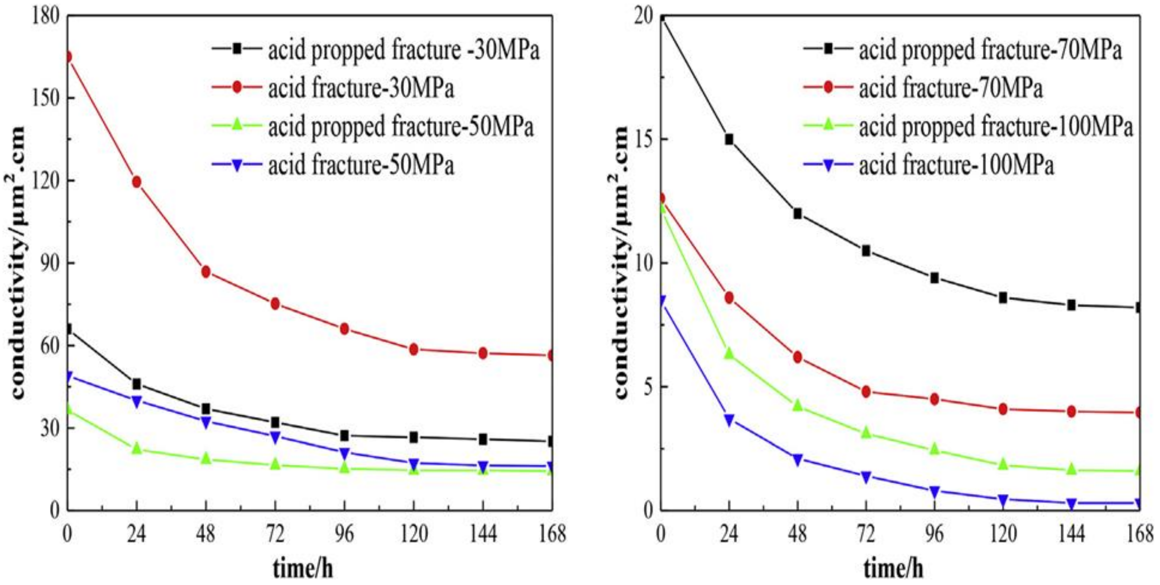

Figure 1: Propped and acid propped fracture conductivity decline with time (Zhang et al., 2018).

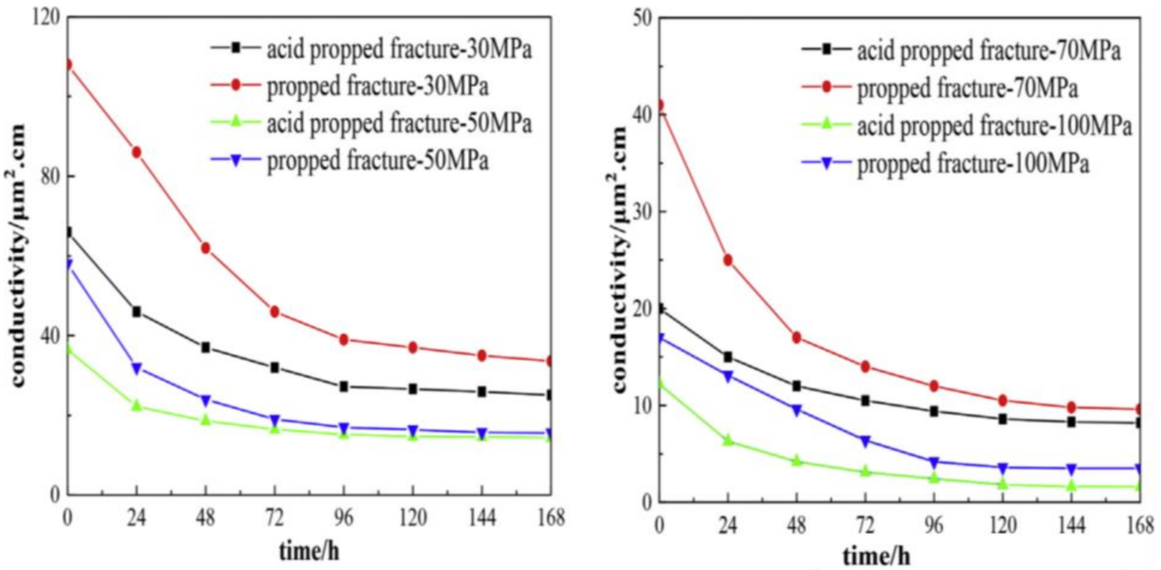

Figure 2: Acid and acid propped fracture conductivity decline with time (Zhang et al., 2018).

1.2 Problem Description

Productivity decay in an acid-fractured well is due to the lumped effect of the elastic, plastic, and creeping responses of the fracture asperities to the applied stress. Primary creeping causes roughly 30-40% production rate decline in a short time due to rock softening after acid fracturing (Abass et al., 2006). Also, the dissolution of minerals by acid destroys the rock structure (Bemer and Lombard, 2010; Chen et al., 2014; Kang et al., 2014; Liu and Mostaghimi, 2017; Lu et al., 2017). Depletion makes the situation worse as the effective closure pressure increases, enhancing the possibility of compressive failure of supporting asperities. The resulting fine particles may also plug the conductive path. Rock strength is a significant factor in maintaining fracture conductivity. For instance, dolomite is harder in nature, it shows sustainable conductivity at high closure stress compared to the limestone and the chalk. Chalk suffers the most from conductivity decline due to rock softness. Thus, improving the rock surface hardness after acidizing will reduce asperities deformation and the conductivity will be maintained.

The etching of the rock with acid is a stochastic process and depends on a lot of parameters. The prediction of the resulted conductivity is challenging. The empirical models are simple but do not include the etching pattern effect. The theoretical ones require a lot of parameters that are hard to be obtained.

1.3 Research Objectives

The goal of this research was to perform systematic experimental work to enhance etched-rock hardness. Ideally, it should be done without reducing the rock permeability, thus enhancing the hydraulic conductivity in the long term. The second objective was to create a predictive model of acid fracture conductivity considering both the etching patterns and rock mineralogy. The goal was to use machine learning tools to improve the understanding of acid fracture conductivity.

CHAPTER 2

LITERATURE REVIEW

Acid fracture job consists of three major steps; the first step is pumping viscous fluid at a pressure higher than formation fracture pressure to initiate a fracture with rough surfaces and cool down high-temperature formations. This fluid is called pad and is pumped to increase the fracture width, to form a filter cake that controls fluid loss, and to enhance the penetration depth of acid along the fracture. The second step is pumping acid that usually gelled, viscosified, foamed, or emulsified to allow acid to penetrate deep by controlling the acid diffusion and leak-off rate (Navarrete et al., 1998). Acid etches some areas that form a fluid flow pathway later, whilst the undissolved regions endure the closure stress after treatment. The last step is flushing to displace the acid deeper in the formation and reduce the corrosion.

2.1 Acid Fracturing Conductivity

Many researchers studied the resulting acid fracture conductivity and the factors affecting it to find a reliable model or correlation to predict it.

Broadus et al. (1968) studied the etching process experimentally. They concluded that there are an optimum acid quantity and acid-rock contact time that will yield maximum conductivity beyond them the rock softens and can’t support the closure stress. They found that acid etching is a function of the temperature, acid type, concentration, contact time, and rock properties. In some experiments, the regular HCl over etched the permeable limestone due to high reactivity which reduced the conductivity while the retarded acid improved it. Also, the retarded acid gave the highest conductivity at high temperature when reacted with the low permeable formation.

Conductivity correlations can be driven through different approaches. Table 1 summarizes most of the popular ones. The empirical correlations which depend on experimental studies are conveniently applied and their parameters can be attained easily. The analytical correlations that are based on theoretical derivations are complicated and require a lot of sophisticated parameters. Some parameters require experimental results to tune them through regression analysis. The artificial intelligence models require accurate and consistent data. The accuracy of these type of models improves with the increase in the data set size.

Table 1: Conductivity correlations summary.

Analytical	**Numerical**	**Empirical**	**Artificial Intelligence**
Gangi, 1978	Deng-Mou, 2010	Nierode-Kruck, 1973	Akbari, 2017
Walsh, 1981	Kamali, 2015	Nasr-Eldin, 2006	Eliebid, 2018
Gong, 1997		Pournik, 2009	Motamedi-Ghahfarokhi, 2018

In 1973, Neirode and Kruk came up with a widely-used acid fracture conductivity model that is based on experimental studies. They estimated the conductivity based on dissolved rock amount, rock embedment strength, and closure stress as can be seen in Equations 2.1 to 2.4.

$$k_f w_i = C_1 e^{-C_2 \sigma_C} \tag{2.1}$$

Where

$$C_1 = 1.47 \times 10^7 w_i^{2.47} \tag{2.2}$$

$$C_2 \times 10^3 = 13.9 - 1.3 \ln(S_{RE}), for: 0 < S_{RE} < 20{,}000\, psi \tag{2.3}$$

$$C_2 \times 10^3 = 3.8 - 0.28 \ln(S_{RE}), for: 20{,}000 < S_{RE} < 50{,}000\, psi \tag{2.4}$$

Where k_f is the fracture permeability (in md), w_i is the ideal fracture width, $k_f w_i$ is the conductivity (in md-ft), σ_C is the closure stress (in psi) and S_{RE} is the rock embedment strength (in psi).

For all models, C_1 can be thought of as conductivity at zero closure stress and calculated from the ideal width. They assumed that the acid will etch the rock leaving a fracture like a slab and from material balance, the ideal width can be calculated by simply divided the total volume of rock dissolved by the fracture area. They assume that the larger the amount of dissolved rock the higher the conductivity, but this is not always true because the etching may be uniform and when the closure stress is applied the fracture faces will fit over each other. Besides this, the larger the amount of dissolved rock because of longer contact time with acid may soften the fracture surface. Hence, the fracture conductivity dies sharply with the increase in the closure stress. The effect of rock softening and etching pattern wasn't considered in their work. The other constant, C_2, control the rate of conductivity decrease with the closure stress. They considered two big categories based on initial rock embedment strength. The first category includes the rocks that have rock embedment strength below 20,000 psi, whereas the second category includes that have rock embedment strength above 20,000 psi up to 50,000 psi. They didn't allow leak-off in their experiments. Thus, its effect is absent in conductivity calculation. Also, samples dimensions were too small to develop any etching pattern rather than roughness.

Gangi (1978) provided a theoretical model where he included the surface asperities distribution (C_3) as a parameter in calculating the conductivity.

$$\left(k_f \mathrm{w}\right)^{1/3} = C_1 - C_2(\sigma_C)^{C_3} \tag{2.5}$$

Walsh (1981) gave another theoretical model as shown:

$$\left(k_f \mathrm{w}\right)^{1/3} = C_1'' - C_2'' \ln{(\sigma_C)} \tag{2.6}$$

The previous theoretical models predict the change in conductivity under different closure stresses with suitable $C_1$and C_2 values. Pournik (2008) found that they are less accurate than Neirode and Kruk correlation.

Anderson and Fredrickson (1989) stated that conductivity is primarily influenced by the amount of rock removed and the removal pattern. While the quantity of rock dissolved is affected by kinetic parameters like acid type concentration, temperature, contact time, and flow regime, the etching pattern is governed by the rock mineralogical composition.

The pattern of rock removal has a crucial effect on the hydraulic fracture conductivity, rather than the amount of dissolved rock. For instance, the conductivity is higher when the acid fracture treatment generates channels instead of the rough surface giving that these channels withstand the closure stress (Van Domelen et al., 1994; Ruffet et al., 1998; Beg et al., 1998; Nieto et al., 2006; Melendez 2007; Pournik 2008; Antelo 2009; Cash 2016; Kamali et al., 2016; Lu et al., 2017). Also, the leak-off of acid into the formation matrix can result in more heterogeneous fracture surface that boosts the conductivity in case the rock mechanical properties are kept unharmed (Beg et al., 1998).

Equation 1.7 presents a theoretical model developed by Gong (1997) that predicts conductivity values closer to experimental results when compared with Neirode-Kruk empirical one, but this model needs more parameters which are difficult to obtain e.g., a measurement of the surface roughness distributions after acidizing. The fracture deformation model considers both the surface roughness and the rock mechanical properties. The fracture closure under stress is modelled as plastic deformation of asperities. Then, the fracture conductivity can be estimated by the next cubic law:

$$k_f w_i = \left(k_f w_i\right)_0 \left[1 - \left(\frac{\gamma}{1+\gamma}\right)\left(\frac{2\sigma_c}{c\sigma_Y}\right)^{1/\gamma}\right]^6 \tag{2.7}$$

where $\left(k_f w_i\right)_0$ is the fracture conductivity at zero stress (md-ft), σ_Y is the rock yield stress (psi), γ is a parameter for the shape of the distribution function curve of the asperities, and c is the stress correction factor.

Nasr-Eldin (2008) separated the original Neirode-Kruk correlation based on lithology into two correlations for limestone and dolomite and used the experimental data to find new C_1

and C_2 values. Pournik (2008) categorized the etching pattern after acidizing rock samples into five categories as shown in Figure 3. The roughness etching pattern happens when the acid etches the rock leaving asperities distributed in the fracture surface. The channelling etching pattern is characterized by the V-shape where the acid etches the middle part more than the edges. The cavity and turbulence etching patterns are similar in the pockets formed by the acid etching, but the later happens in more reactive formations and may develop wormholes. The uniform etching pattern may be generated due to low reactivity of the rock with acids or the rock itself has a pure mineral that uniformly reacts with acids. For the same acid system, contact time may influence the etching pattern. It is more likely to generate roughness when acidizing smooth surfaces, but acidizing rough surfaces deepens the valleys and smoothens the peaks (Al-Momin et al., 2014). As the contact ratio between the fracture two faces increases the resulting conductivity increases. Pournik considered both the theoretical and empirical methods in developing a conductivity correlation for roughness etching pattern considering each rock type separately.

Also, the acid concentration changes along the fracture length influence the change in the amount of rock dissolved and etching pattern (Pournik et al., 2013). Unspent acid creates the major amount of etching and more conductive etching patterns.

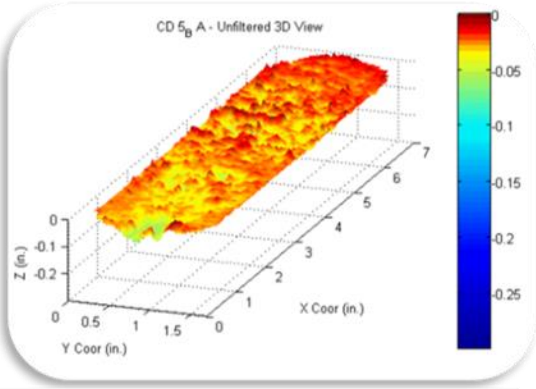

a) Roughness

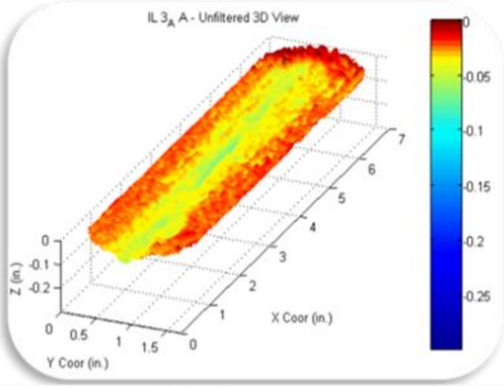

b) Channeling

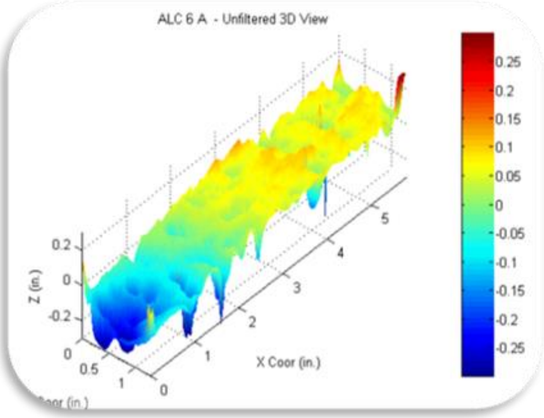

C) Turbulent

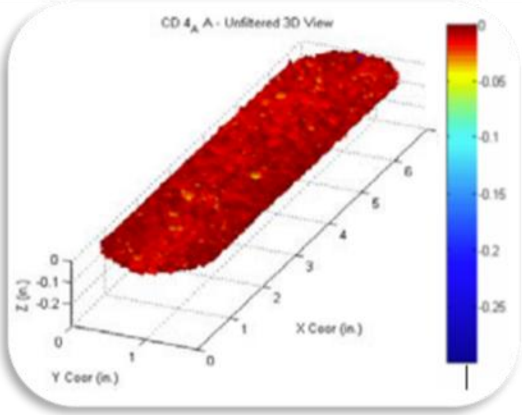

d) Uniform

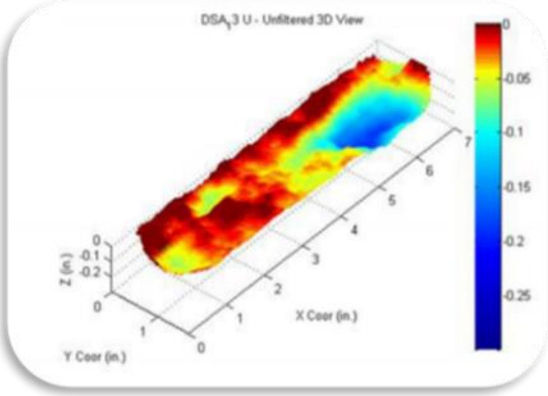

e) Cavity

Figure 3: Etching patterns (Pournik, 2008).

The previous models do not account for the contribution of channels to the conductivity. They provide higher conductivity at low stress and durable conductivity after the closure of the fracture. The large channels dimensions make the flow easier and the pressure drop lower. Deng and Mou (2012) tried to capture it through numerical studies and managed to enhance the conductivity prediction. They classified the etching pattern into three categories: permeability distribution dominant, mineralogy distribution dominant, and competing effect of permeability and mineralogy distributions. To apply their correlations, six parameters are needed: The ideal fracture width, the ideal Young’s modulus, the calcite fraction, the horizontal and vertical correlation lengths, and the standard deviation for permeability distribution. Almomen (2013) showed that rough-surface fractures generate higher conductivity by an order of magnitude compared with a smooth-surface fracture at low-closure stress. Thus, ignoring such factors surely will give simple models but these models will be inaccurate and biased.

Akbari et al. 2017 used 106 data points from the 25 experiments done by Nierode and Kruk to develop their conductivity models. The data set was used to modify Nierode and Kruk correlation based on the genetic algorithm. Also, the data was divided based on the rock embedment strength into two groups to generate two more models. The developed correlations slightly improved productivity prediction.

Eleibid et al. (2018) used artificial neural networks and adaptive network-based fuzzy inference system to develop a precise intelligent model. The same data set of Nierode and Kruk was used in building their conductivity model. They achieved a higher accuracy level, but the main problem is that the Nierode and Kruk experimental data was generated from small samples. The different etching pattern was ignored as the only observed one on the tested samples was roughness etching pattern.

2.2 Factors Affecting Rock Mechanical Properties After Acid Exposure

Many parameters are used to represent the rock strength such as Young's modulus, Poisson's ratio, confined and unconfined compressive strength, rock embedment strength, and Brinell hardness. Measurements of the last two parameters are similar. Brinell hardness is measuring the load for a given predetermined indentation while the second measuring the indentation for a given load. Also, in elastic region, Poisson's ratio is the ratio of the proportional decrease in a lateral measurement to the proportional increase in length in a stretched sample while Young's modulus is the ratio of stress to strain. Correlations between the different strength parameters exist and explained in the literature (Eissa et al., 1988; Aggistalis et al., 1996; Joel et al., 2011; Morsy et al., 2015; Teklu et al., 2017). Barri et al. (2016) the effect of chelating agents on Indiana lime and Austin chalk and found that the later is more affected due to more diffusivity of the chelating agents into it.

Many scholars studied the effect of acidizing on the deterioration of rock mechanical properties (Gou et al., 2019; Morsi et al., 2015). The following factors affect the rock strength after acidizing:

2.2.1 Formation Type and Degree of Cementation

Generally, dolomite has the highest hardness magnitude among carbonate rocks while chalk has the lowest and limestone is in between. Acid fracturing requires a precise selection of the acid type and treatment conditions. There are optimal acid type, concentration, contact time and treatment conditions that do not severely deteriorate the rock mechanical properties. Experimental study shows that limestone strength is more vulnerable to acidizing than dolomite (Al-Mutairi et al., 2008, Zhang et al., 2018).

Based on experimental data, Gong (1997) found that the deterioration of rock mechanical properties impacted the acid fractured rock conductivity. The degree of deterioration depends on the acidizing condition, especially leak-off flux. An increase in Poisson’s ratio and decrease in Young’s modulus and rock hardness has been reported by Gong.

Zhang et al. (2018) carried out a series of experiments to quantify the reduction in the mechanical properties of limestone and dolomite by gelled acid. They categorized the rocks based on the cementation strength and mineral composition. Due to the reactivity of limestone, it suffered the highest reduction in uniaxial and triaxial compressive strength after acidizing as shown in Figures 4 and 5.

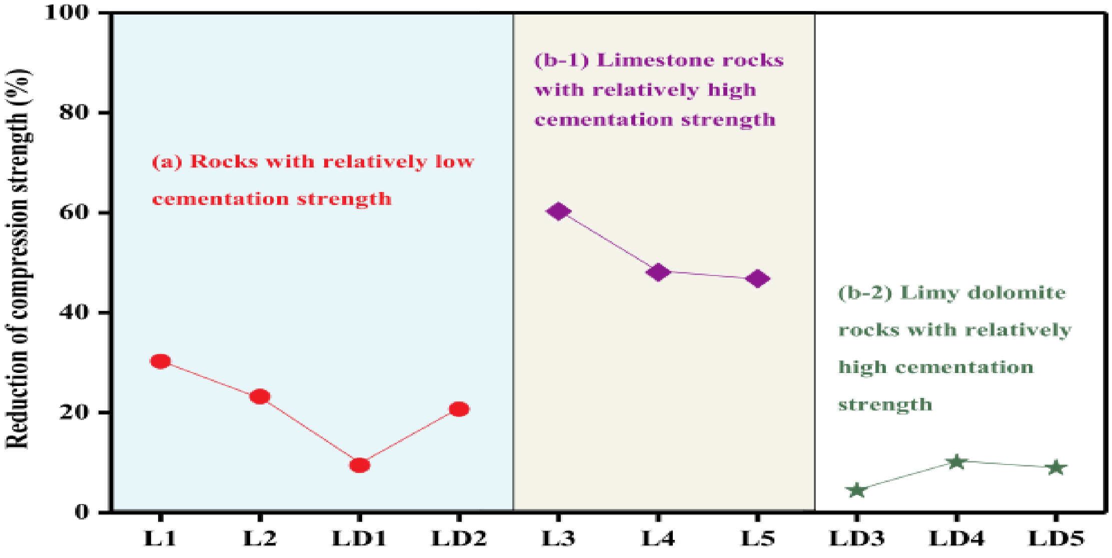

Figure 4: Reduction in the uniaxial Compressive strength of acidized rocks (Zhang et al., 2018).

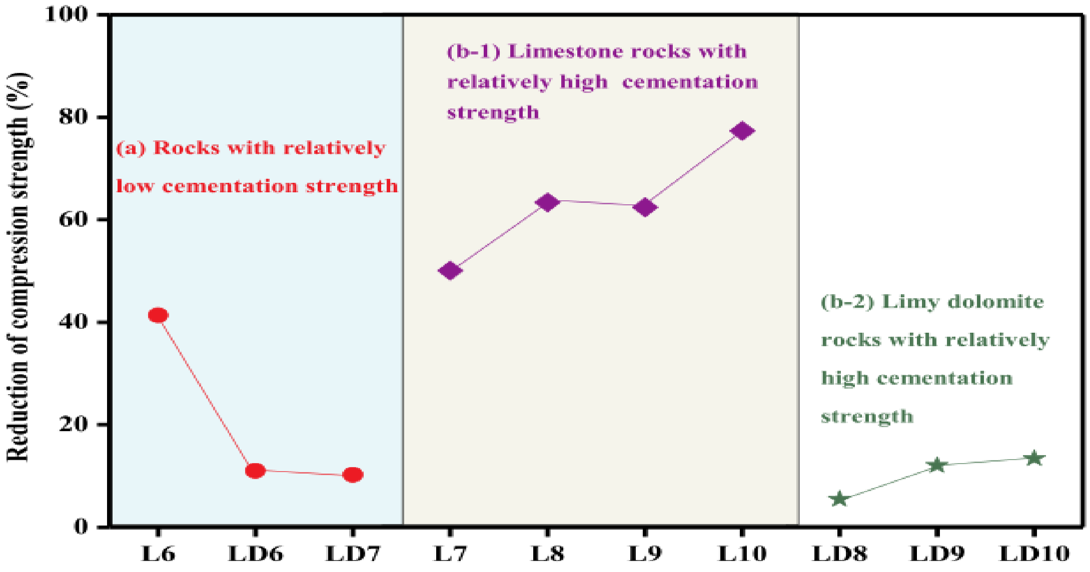

Figure 5: Reduction in the triaxial compressive strength of acidized rocks (Zhang et al., 2018).

2.2.2 Acid concentration

Bartko et al. (1992) investigated the effect of different acid types on the conductivity to specify the optimal acid type that gives a long-term conductivity. The laboratory study indicated that the optimal treatment would be obtained by using emulsified acid. Increasing acid concentration from 10% to 15% caused a 60% reduction of core strength and consequently resulted in lower conductivity.

2.2.3 Acid contact time

Longer contact time does not usually give the higher conductivity even though it may result in more rock dissolution (Beg et al 1998; Melendez 2007; Pournik 2010).

2.2.4 Acid Type

studied the effect of different acids on rock hardness. Acid softening after acidizing with plain HCl was more than that of emulsified and gelled acids because of the high leak-off rate to the formation. Production history for stimulated carbonate wells showed that emulsified acid system outperforms the plain acid and in-situ crosslinked acid in terms of initial production and decline rate (Nasr-Eldin et al., 2006; McDuff et al., 2018).

It is obvious that the rock exposure to acid reduces the rock hardness, but in some cases at some locations, the rock hardness improves. This results from the dissolution of the soft areas which expose the harder ones below it. In rough surfaces, the high points will be responsible for keeping the fracture open. The rock embedment strength of these high points matters the most because they will support the closure stress (Melendez 2007; Gomaa et al., 2009; Asadollahpour et al., 2018).

2.3 Acid Conductivity Decline Rate

Acid conductivity decay is due to a combination of elastic response, asperities failure and creeping. Young’s modulus governs the elastic response of rock. If the asperities compressive strength is higher than the closure stress, they will be deformed elastically resulting in decreasing in the fracture width. Otherwise, they will fail. The creeping is a slow time-dependent deformation under continuous load (Abbas et al., 2006).

Creeping test of acid fracture samples involves applying progressive stresses for a prolonged time and observe the strain behaviour for three cycles of loading. The elastic behaviour and time-dependent creeping are shown in Figure 6. The total deformation for three cycles of loading is clarified in Figure 7.

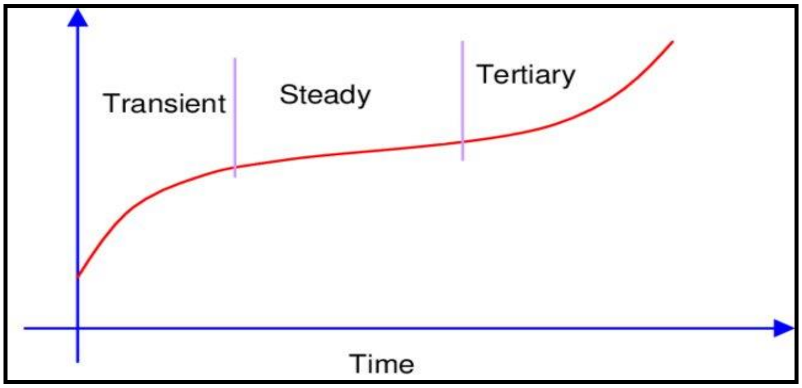

Figure 6: Creep vs time (Abbas et al., 2006).

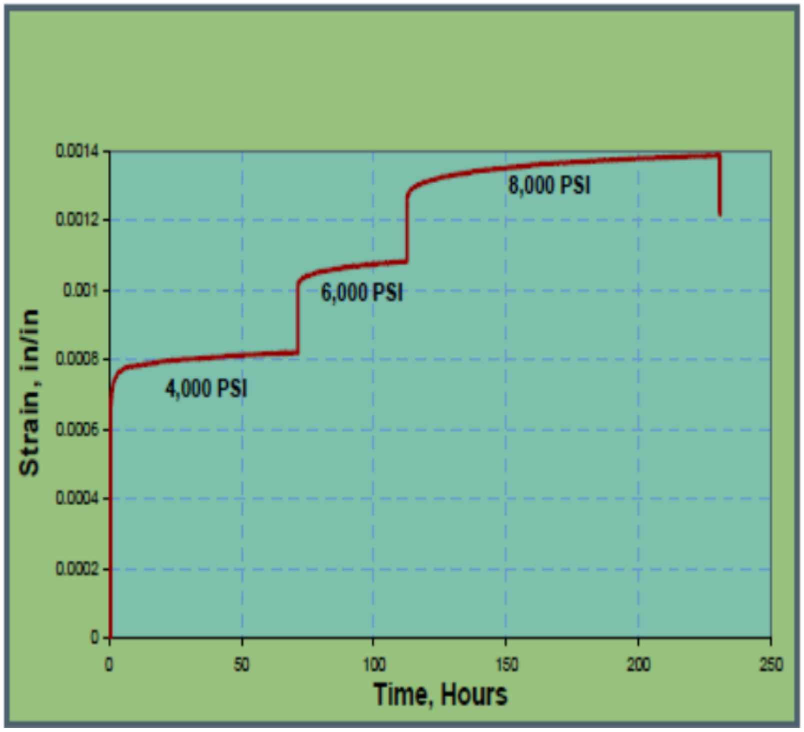

Figure 7: Time and the observed strain behavior for three cycles of loading (Abbas et al., 2006).

Deng et al. (2012) studied the effect of rock mechanical properties numerically. They fixed all other parameters and only changed the Poisson's ratio from 0.1 to 0.4. They found that the Poisson's ratio has no significant effect on the conductivity as shown in Figure 8.

They did the same to study the effect of Young's modulus. A dramatic two orders of magnitude increase on the conductivity value was observed when doubling Young's modulus (see Figure 9). As the figure shows, the rock strength became more important at high closure stresses.

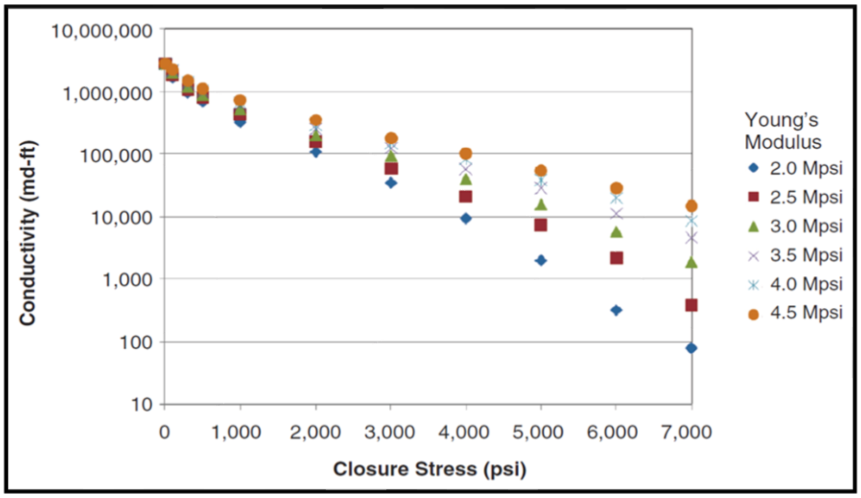

Figure 8: Young's modulus effect on fracture conductivity

(Deng et al. 2012).

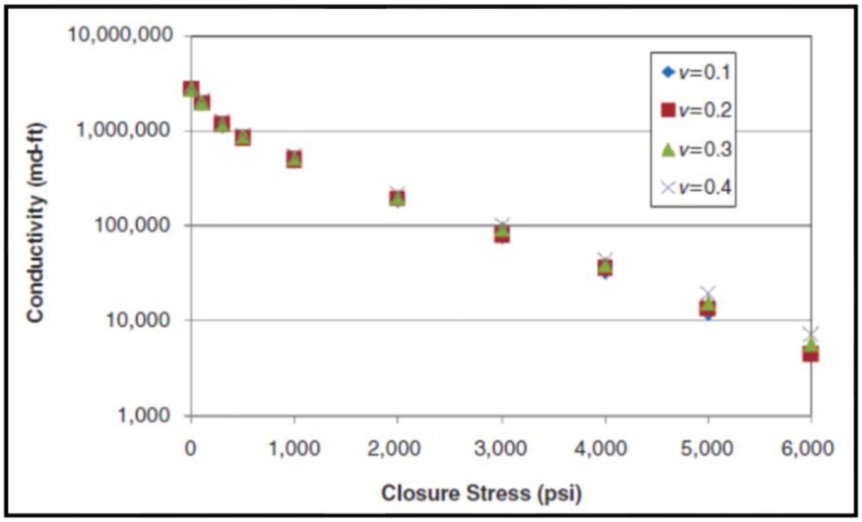

Figure 9: Poisson's ratio effect on fracture conductivity

(Deng et al., 2012).

2.4 Approaches to Restore the Rock Strength

2.4.1 Consolidation

Calcium hydroxide nanocrystals have been used to repair the deteriorating historic buildings. Calcium hydroxide nanoparticles fill the pores and inter-crystalline grain contacts. The crystallization of the calcium hydroxide depends on temperature and relative humidity (RH) as illustrated by X-ray diffraction (XRD) in Table 2 (P. López-Arce et al 2010). At low humid environment, the nanoparticles precipitate as portlandite $Ca(OH)_2$. Whereas at a high humid environment, portlandite $Ca(OH)_2$ transforms to vaterite ($CaCO_3$), monohydrocalcite ($CaCO_3 \cdot H_2O$) and calcite ($CaCO_3$), resulting in significant improvement in rock strength (P. López-Arce et al 2011). The porosity decreases after treatment because of lining the pores with the nanocrystals and the ultrasound velocity significantly increases. Also, nuclear magnetic resonance (NMR) analysis showed that the pore size decreased.

Calcium hydroxide nanocrystals react with carbon dioxide and the moisture of the atmosphere to form calcium carbonate polymorphs in place (Ossola et al., 2012). The formation of calcium carbonate polymorphs occurs according to the following reactions:

The diffusion of CO_2 in the gas/liquid interface, when carbon dioxide dissolves in water, it exists in chemical equilibrium with carbonic acid

$$H_2O + CO_2 \rightleftarrows H_2CO_3$$

$$H_2CO_3 + H_2O \rightleftarrows HCO_3^- + H_3O^+$$

$$HCO_3^- + H_2O \rightleftarrows {CO_3}^{2-} + H_3O^+$$

The dissolution of solid $Ca(OH)_2$, releasing calcium Ca^{2+} and hydroxyl OH^{-} ions, and the precipitation of Ca^{2+} with $CO3^{2-}$ forming $CaCO_3$.

The overall reaction can be expressed as:

$$Ca(OH)_2 + CO_2 \rightarrow CaCO_3 + H_2O$$

Table 2: XRD quantification of portlandite and calcium carbonate polymorphs depending on RH and exposure time (P. López-Arce et al 2011).

RH	**Time**	**Portlandite**	**Calcite**	**Vaterite**	**Aragonite**	**MHC**
		2	**3**	**3**	**3.5-4**	
(%)	(days)	(%)	(%)	(%)	(%)	(%)
33	7	96	4	N/d	N/d	N/d
	28	84	8	N/d	N/d	8
54	7	92	N/d	8	N/d	N/d
	28	36	N/d	52	7	5
75	7	N/d	3	20	41	36
	28	N/d	11	39	23	27
90	7	N/d	32	37	N/d	31
	28	N/d	37	25	24	16
N/d (Not detected), MHC (monohydrocalcite).						

Also, tetraethyl orthosilicate (TEOS) is being used as a consolidation agent for deteriorating limestone of ancient historical monuments (Pinto et al., 2012). The chemical compound formula is $Si(OC_2H_5)_4$. TEOS solution has no colour and degrades in water and most prevalent alkoxide of silicon. Its effectiveness comes from hydrolysis-condensation reactions, that lead to the formation of amorphous silica inside stone pores. The compatibility of the deposited silica gel with silicate substrates and its ability to form strong Si-O-Si bonds. TEOS effectiveness, however, is known to be dependent on the presence of quartzitic fractions inside the substrate, allowing for chemical bonding. Thus, it is more impactful in sandstone than limestone (Graziani et al., 2015).

2.4.2 Mineral Alteration

The purpose is to change the minerals on the rock surface to harder ones. Table 3 shows various minerals that have higher hardness than calcite. A filtration process was carried out on the carbonate minerals to decide which reaction is appropriate. Some basic requirements need to be fulfilled in the targeted hard mineral to increase the possibility of transformation reaction. The hardness of carbonate minerals varies from 1 to 6, and their hardness, to some degree, is a function of the mineral hydration level. In carbonates of monovalent and divalent cations, minerals lacking H_2O or non-hydrated, have a hardness between 1.5 to 5; nevertheless, the hydrated ones have a hardness magnitude up to 4. More hydrated minerals have hardness magnitude below 3. This relationship is present within the pure carbonates, regardless of whether they contain OH^- (Railsback 1999). Thus, to pick a mineral which is harder than calcite it should not be hydrated and has a simple chemical formula. There are complex carbonate minerals that have high hardness values, but forming them in the lab may not be possible. Also, toxic hard minerals should be avoided in addition to the minerals which have a higher solubility than the calcite as the target is to form a safe and stable hard mineral. Having the same lattice system increases the possibility of the calcite to transform into the harder mineral.

Natural calcite seeds are used to precipitate zinc from water in the water purification process. Smithsonite is formed directly on calcite due to the close values of the lattice constants of them (Aziz et al., 2008; Zhizhaev et al., 2008).

Zinc precipitation in the exchange reaction yields gypsum (Zhizhaev et al., 2014).

$$Zn^{2+} + SO_4^{2-} + CaCO_3 \xrightarrow{2H_2O} ZnCO_3 \downarrow \ + CaSO_4.2H_2O \downarrow \ .$$

Table 3: Summary of various carbonate minerals properties.

Name	Chemical Formula	Mohs Hardness	Crystallography		Cell Dimensions			
			System	Class Name	a	b	c	Z
Calcite	$CaCO_3$	3	Trigonal	Hexagonal Scalenohedral	4.989		17.062	6
Alstonite	$CaBa(CO_3)_2$	4-4.5	Triclinic		17.38	14	6.123	10
Magnesite	$MgCO_3$	4	Trigonal	Hexagonal Scalenohedral	4.63		15.15	6
Siderite	$FeCO_3$	4	Trigonal	Hexagonal Scalenohedral	4.72		15.46	6
Smithosonite	$ZnCO_3$	4-4.5	Trigonal	Hexagonal Scalenohedral	4.653		15.028	6

CHAPTER 3

Setup and Procedure of the Experimental Work

In this chapter, the used apparatuses and procedures to enhance the rock surface hardness are described. The sequence of experimental work is summarized in Figure 10.

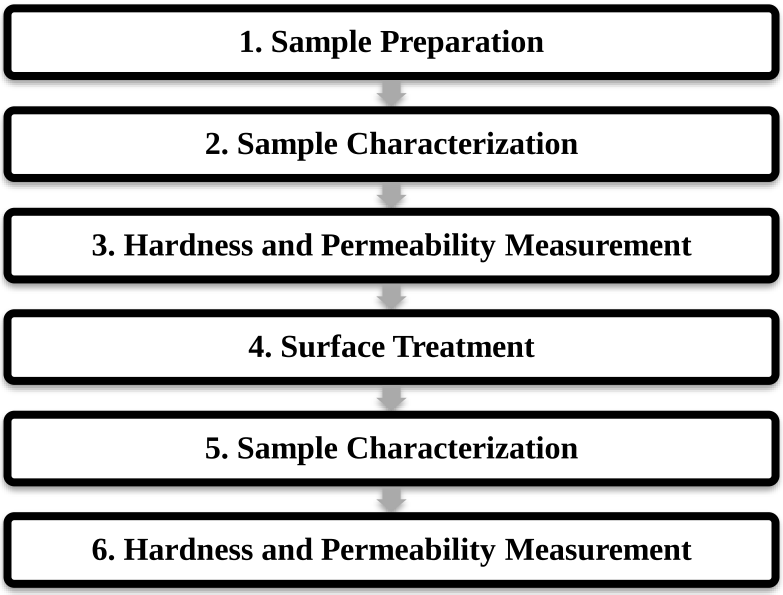

Figure 10: Experimental work summary.

3.1 Rock Samples Preparation

- Specify the required rock samples and formations for the desired experiments.
- Gather the needed number of samples to perform the experiments on. The samples were gathered from Khuff formation outcrop near Qassim. Also, another set of Indiana limestone cores have been utilized.
- Cut Khuff rock samples into similar rectangular blocks with a cross-section of 3.3×3.3 in and a thickness of 1 in. Indiana limestone cores with diameters of 2.5 and 1.5 in were

cut into plugs with lengths of 3 and 1.5 in respectively by an electric saw. The dimensions were selected to suit the apparatuses used and summarized in Table 4.

- Label and weigh the rock samples
- Measure the lengths of the samples and store them.
- Cut smaller cubic samples to be scanned with quantitative evaluation of minerals by scanning electron microscopy (QEMSCAN) and scanning electron microscopy (SEM).

Table 4: Summary of samples dimensions and the required analyses.

Shape	Dimensions (in)	No.	ID	Target Analysis
Rectangular parallelogram	3.3×3.3×1	6	1:5 & 5.1	Hardness, permeability, and porosity
Cylindrical	1.5 Dia. & 1.5 length	8	1S:6S	Hardness, permeability, porosity and XRF
Cylindrical	2.5 Dia. & 3 length	8	1L:8L	Hardness, permeability, porosity and XRF
Cubic	0.02×0.02×0.02	5	1:5	QEMSCAN and SEM

The hardness will be measured at several points as shown in Figure 11.

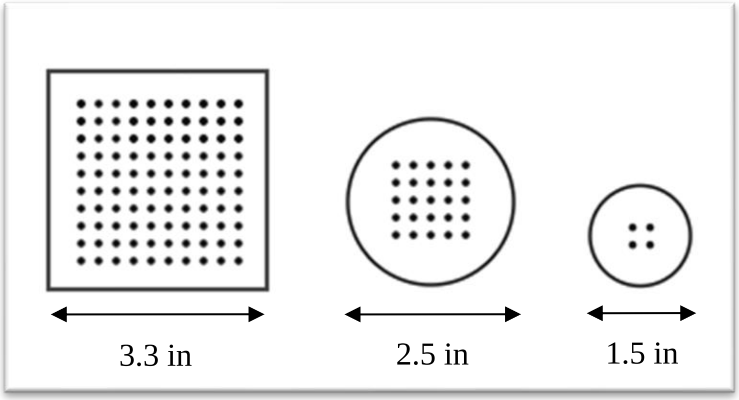

Figure 11: Points of measurements.

3.2 Samples Characterization

3.2.1 Scanning Electron Microscopy (SEM)

To track the changes that occurred on the rock surface at microscale level after treatment, the samples were studied by QEMSCAN and SEM. Thus, high-resolution images were acquired for both fresh and treated samples for comparison purposes. The steps that were taken to prepare the samples for imaging are:

- Clean the stubs with acetone.
- Use double face glue paper to fix the samples on the stub's tops.
- Wrap the samples with aluminium paper as illustrated in Figure 12.
- Coat the samples with carbon using Quorum Q 150TE.

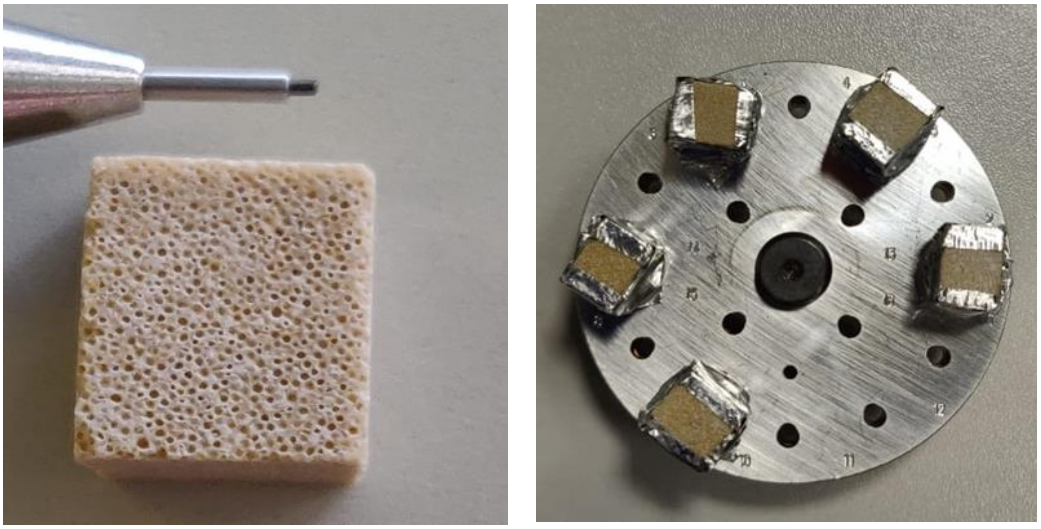

Figure 12: Samples preparation for SEM scanning.

3.2.2 X-ray fluorescence (XRF)

M4 TORNADO X-ray fluorescence was employed for the information regarding rock composition and element distribution. The samples to be scanned before and after the treatment with the chemicals to study their effect on the surface elements of the rock. When seeking alteration of surface minerals, the XRF analysis is useful to prove if a treatment solution causes a certain mineral enrichment or impoverishment on the surface.

3.2.3 Gas Permeameter

GP-101AE gas permeameter consists of core holder, inlet and outlet pressure gauges, confining pressure gauge, hand pump and mass flow controller.

- Turn the unit on and allow it to warm up for 5 minutes then put the dry 1.5 in diameter core plug in the core holder.
- Open the confining pressure valve (V2) and operate the hydraulic pump to achieve the desired confining pressure then close the valve.

- Make sure the pressure regulator knot is in the furthest “decrease” position.
- Place the protection valve in “Open” position.
- Slowly turn the regulator to allow the gas to enter the core through the inlet end. The inlet pressure gauge will show the pressure at which the gas is entering the core.
- Record the stabilized inlet pressure by hand. The flow rate is available from the software, which is recorded automatically.
- Increase the inlet pressure to obtain another stabilized outlet flow rate and repeat this step three or four times and the gas permeability was calculated as mentioned later in Appendix A.
- Close the gas source valve and adjust the pressure regulator to decrease position.
- Open valve (V2) and release the confining pressure.
- Unscrew the bottom end of the chamber and remove the core sample.

3.2.4 Helium Porosimeter

TPI-219 helium porosimeter is a volume - measuring instrument based on Boyl’s law.

The following steps are used to fill the provided data sheet for porosity calculation:

- Calibrate the device before usage.
- Weigh clean, dry and perfect cylinder core sample using a balance and record the sample diameter and length.
- Set the sample on the tabletop. Create a stack of billets next to the sample that is equal in height or slightly taller than the sample height.
- Place the remaining billets inside the cup.

- Place the sample on top of the billets in the cup and place the cup with the sample inside the frame opening. Open the VENT valve and the TO CORE valve then, close the cup to the sealed position.
- Read the pressure and record it as ZERO PRESSURE in the SAMPLE DATA section.
- Close the TO CORE and the VENT valves.
- Open the SUPPLY HELIUM GAS valve to allow the reference section of the system to pressurize between 92 to 95 psi then, close the valve.
- Record the stabilized digital pressure readout value as the SYSTEM REFERENCE PRESSURE under the SAMPLE DATA section.
- Open TO CORE valve and allow the pressure to stabilize then, record the digital pressure readout value as the CUP SAMPLE PRESSURE under the SAMPLE DATA section.
- Open the VENT and TO CORE valves to deplete the pressure and use the provided sheets to calculate the porosity as mentioned later in Appendix B.

3.3 Hardness and Permeabilirt Measurement by AutoScan

The main hardware component is a robotic crossbar that permits automatic positioning of the probe(s) of measurement using an XY-reference frame for table measurements as shown in Figure 13.

AutoScan base components include:

- AutoScan software and computerized data acquisition system
- Robotic XY-Table and gantry with at least one Z-axis actuator
- Laser Displacement Sensor

- Pneumatic Control System
- One of the multiple probes can be mounted on the scanner head such as permeability head to measure the steady-state gas permeability or impulse hammer head to measure the surface Young’s modulus.

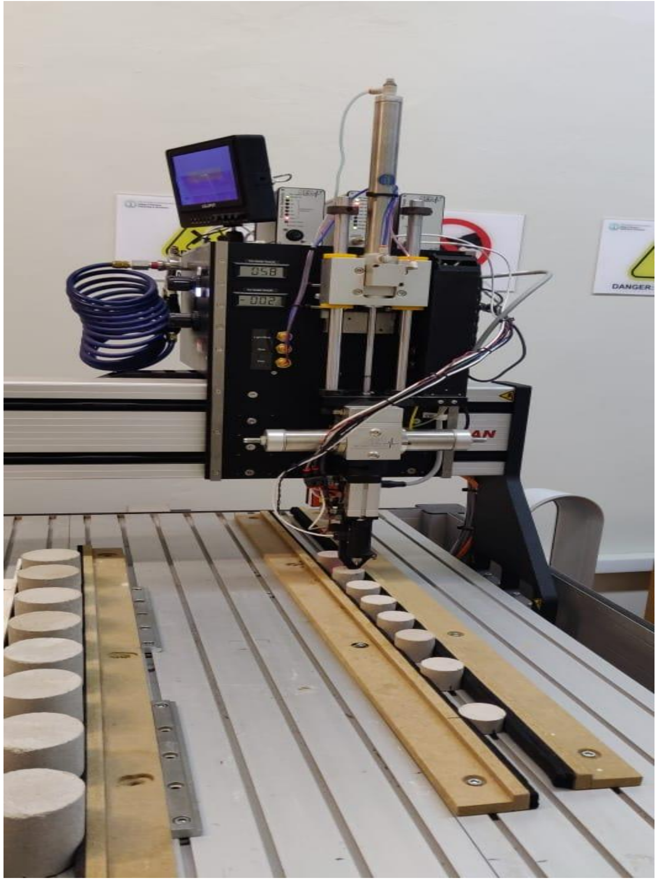

Figure 13: Measurement of Indiana limestone permeability by AutoScan.

The hardness of the surface and the permeability measurements are performed before and after the surface treatment step on the surface of the rock which was exposed to treatment fluid to track the change in these properties.

3.3.1 Permeability

Using a steady-state gas injection technique, permeability can be measured. Permeability values ranging from 0.1 md to 3 d are measured with the standard 4.0 mm Permeability Tip.

3.3.2 Impulse Hammer

To characterize the elastic stiffness variability along with the mechanical strength, the Impulse Hammer Probe is used. The probe measures an elastic stiffness that in the elastic regime is dominated by Young’s modulus. The probe can be configured to produce an additional strength index as well.

To make measurements by the AutoScan software, the following procedures are performed:

- Fix the head relevant to the property you need to measure e.g., impulse hammer, permeability, etc.
- Place samples on the table between any two steel or wooden bars. Fix the bars with screws and nuts to the table.
- Turn on the power for both the hardware and software systems.
- The AutoScan Measurement Program is first initiated by selecting the AutoScan program icon usually located in the taskbar.

- Select the data directory and with laser tip, select tip files corresponding to hardware tips attached
- to the Z-Head and used in measurement session.
- The “Move Tips’’ window will appear. This window is used to manually move the Z-head around the XY-Table and perform manual measurements. The Z-Head can be moved either by entering coordinates for the Z-Head or by using the Joystick for manual motion control.
- Press “Add Sample” tab
- Define the sample dimensions and location coordinates by moving the laser to one of the sample corners and press “Use Current” button in “Origin (mm)” tab then repeat this for the opposite corner.
- Select the area and the number of requested points to be measured for each sample from “Add Measurement Tile”.
- Enter measurement variables and acquisition parameters.
- Save measurement layout for future use (optional) and press start measurements.
- Process and export data files saved to the directory.

3.4 Sample Treatment

3.4.1 Microemulsion

The first attempt to enhance the rock strength was to use the anchoring primer used in painting application (see Figure 14).

Figure 14: Anchoring primer used in painting applications.

4 samples from Khuff formation were treated according to the next steps:

- The samples were cut with slab saw. The samples had a smooth square surface of 10×10 cm. Two of them were extremely tight and the other two were porous.
- To get a resembling measurement of samples hardness, a grid of 10×10 was made to get as many measurements as possible. The total number of points was 100 then hardness was measured by AutoScan.
- The samples were immersed in the microemulsion to their halves. Sample 1&3 were dry and dipped in the microemulsion for 72 hours (see Figure 15). Samples 2&4 were saturated with deionized water before dipping them in the microemulsion for 24 hours.

- All samples were dried in the vacuum oven for a sufficient time to prepare them for hardness measurement again.

Figure 15: Treatment of Khuff limestone with microemulsion.

3.4.2 Nanocrystals Solutions

Khuff limestone samples were treated in the open air without controlling the humidity levels by the next steps:

- Dropping 10 ml of ethanol $Ca(OH)_2$ nanoparticles solution on sample 4.1 wet surface and 10 ml of isopropyl $Ca(OH)_2$ nanoparticles solution on sample 4 dry surface.
- Leaving the sample in the open air for 48 hrs.
- Repeat the previous steps one time.

The carbonation process of calcium hydroxide nanocrystals requires controlling the alcohols evaporation and carbon dioxide to proceed. Thus, Humidity level had to be controlled to drive the reaction and this can be done by temperature and humidity oven.

- Impregnate the Indiana limestone core plugs surface with the nanocrystal solutions.
- Put the samples in the humidity chamber for 48 hrs. at 25 ^{o}C and 75% relative humidity (see Figure16).
- Impregnate the samples again with the nanocrystal solution.
- Put the samples in the humidity chamber for 72 hrs. at the same conditions.
- Dry the samples in the oven at 90 ^{o}C for 4 hrs.

Figure 16: Treatment of Indiana limestone with nanocrystals solutions in the humidity chamber to control alcohols evaporation.

3.4.3 Zinc Solutions

Indiana limestone was treated with the zinc solutions with the aim of incorporating the zinc atoms in the calcium atoms' places in calcite crystals. The goal of these treatments is to turn the calcite into smithsonite by following the next consecutive steps:

- Prepare the solutions by dissolving 3.41gm of zinc chloride in 250 ml of water to get a concentration of 0.1 M.
- Prepare another solution by dissolving 3.41gm of zinc chloride and 3.55 gm of sodium sulfate in 250 ml of water to get a concentration of 0.1 M of zinc sulfate and use magnetic stirrer as needed.
- Measure the pH of the solutions before the immersion.
- Immerse the samples in solutions for 48 hrs. (Figure 17).
- Measure the PH of the solutions after this time and remove the samples.
- Dry the samples in the oven at 90 ^{o}C for 4 hrs.

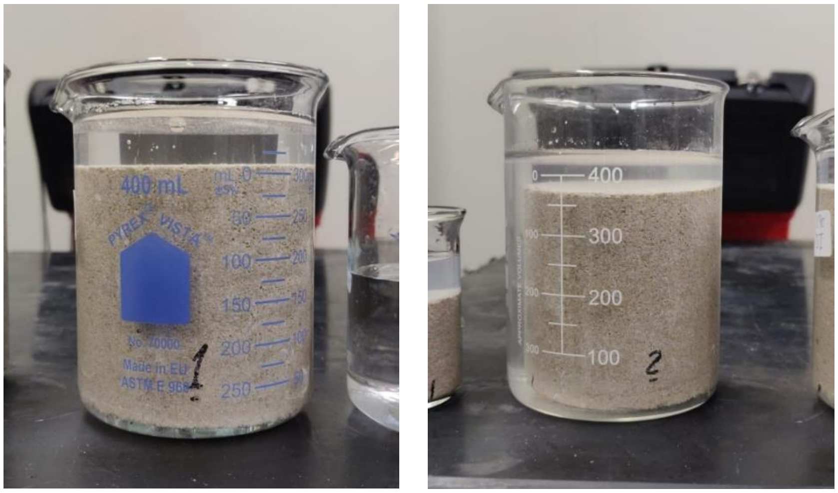

Figure 17: Treatment of Indiana limestone with zinc solutions.

3.4.4 Tetraethyl orthosilicate (TEOS) solution

The treatment of Indiana limestone samples with TEOS was similar to that of zinc solutions. The unit volume of raw TEOS was diluted with a 10 volume of water and the samples were dipped for 48 hrs. the samples were dried up in a vacuum oven for 90 ^{o}C for 4 hrs (see Figure 18). Sample 8L was the only sample to be impregnated with the raw TEOS without dilution.

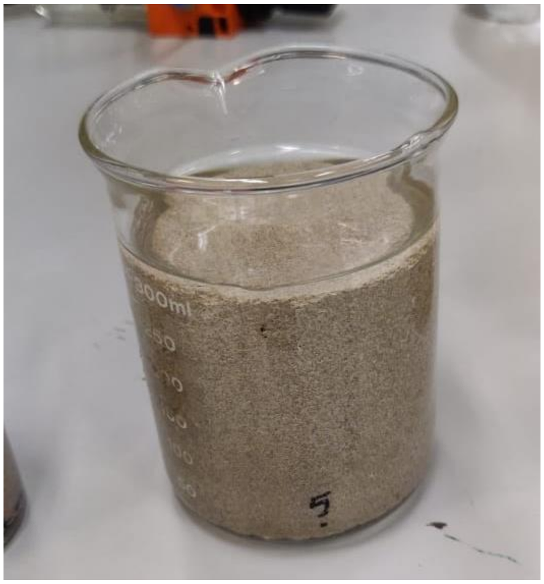

Figure 18: Treatment of Indiana limestone with a TEOS solution.

CHAPTER 4

EXPERIMENTAL RESULTS AND DISCUSSION

Selecting the proper samples is crucial in getting precise and consistent results. To conduct the experiments, the minimum requirements should be fulfilled (e.g., high homogeneity on the macroscopic scale, medium to fine-grained). Khuff and Indiana limestone samples consist mainly of calcium carbonate. The samples showed no bedding planes and the original porosities were around 29% and 17%, respectively. The high porosity of Khuff limestone is due to the vuggy nature of the samples. The samples were machined to a geometry that allowed taking as much measuring points as possible.

Surface Young's modulus measurement using the AutoScan showed varying values but within a range. Also, these values are normally distributed and centred around a value which can be safely assumed to be representative of the sample strength when performing a quick comparison. When repeating the measurement several times, it gave nearly the same range around the same centre.

Young's modulus is the ratio between the stress and the strain in the elastic region as the stress is the instantaneous load applied to the material divided by its cross-sectional area. The greater the modulus, the stiffer the material and the smaller the strain. Hardness is a measure of a material's resistance to deformation by surface indentation. The plastic deformation is caused by the motion of dislocations in the atomic structure of a material. The yield strength of a material may be changed by inhibiting dislocation motion through imperfections or grain boundaries. Thus, Assessing the strength of rock by Young's modulus is more reliable and general than rock embedment strength and Brinell hardness. The first includes the bulk of a specific material while the later is measured at specific points and susceptible to imperfections or grain boundaries.

Experiments were conducted with three different fluids on two different formations (Table 5). Some experiments were repeated to investigate the consistency and reproducibility of the results. Khuff formation samples are rectangular with a square cross-section that was wide enough to take 100 measurement points. Whereas Indian limestone samples were cylindrical with 2.5 in circular cross-section that allowed making 25 measurement points. Khuff limestone was treated in addition to standard Indian limestone as the acid fracturing is common in the first.

Smaller Indian limestone cylindrical samples were used for different purposes. First is to double-check the hardness results of the larger Indian limestone samples which were treated with the same fluid system. The second purpose is to investigate the change of porosity and permeability that might happen during treatment with the known conventional methods (e.g., helium porosimeter and gas permeameter). The last purpose was to assess the measurement of permeability results from the AutoScan.

Table 5: Summary of samples origin, names, no. of measurement points and their treatment solutions.

Treatment System		Formation	Sample Code	Count
Microemulsion		Khuff	1	100
			2	
			3	
			4	
Nanocrystal	**Ethanol**	Khuff	5.1	100
		Indiana	3L	25
			3S	4
	Isopropyl	Khuff	5	100
		Indiana	4L	25
			4S	4
			7L	25
			6S	4
Zinc	**Zinc Chloride**	Indiana	1L	25
			1S	4
	Zinc Sulfate		2L	25
			2S	4
			6L	25
TEOS		Indiana	5L	25
			5S	4
			8L	25

4.1 Microemulsion Solution

The first trial to enhance the samples mechanical properties was not perfect. The tight samples were muddy limestone and did not resemble the Khuff formation as supposed to be. The porous sample weight was roughly half the weight of the tight one and showed heterogeneity. Also, the tight samples were much harder than the porous ones. In addition, the permeability measurement for these samples was not reliable because of the tightness or heterogeneity.

Khuff sample 1 exhibited a minute enhancement in Young’s modulus, less than 3%, after the treatment with the microemulsion solution (see Table 6). It was hard from the start and proving the hardening of hard rock was challenging.

Table 6: Statistical summary of sample 1 Young's modulus measurements.

Parameter	**Microemulsion Solution**	
	Young's Modulus Before (Gpa)	**Young's Modulus After (Gpa)**
Mean	24.8	25.5
Standard Deviation	1	3.3
Range	5.1	17.9
Minimum	22	13.4
Maximum	27.1	31.3
Count	100	

Khuff sample 2 mean and maximum values of Young’s modulus after treatment decreased (see Table 7). The saturation of this sample with deionized water might erode this muddy sample and weakened it.

Table 7: Statistical summary of sample 2 Young's modulus measurements.

Parameter	Microemulsion Solution	
	Young's Modulus Before (Gpa)	Young's Modulus After (Gpa)
Mean	25.3	24.4
Standard Deviation	0.8	0.7
Range	5.5	4
Minimum	21.6	21.8
Maximum	27.1	25.8
Count	100	

Khuff sample 3 mean and minimum values of Young’s modulus after treatment increased (see Table 8). But, the range of measurement was extremely large and emphasized the heterogeneity of this sample.

Table 8: Statistical summary of sample 3 Young's modulus measurements.

Parameter	Microemulsion Solution	
	Young's Modulus Before (Gpa)	Young's Modulus After (Gpa)
Mean	7.5	8.1
Standard Deviation	3.5	3.7
Range	22.7	19.3
Minimum	2	2.5
Maximum	24.7	21.8
Count	100	

All the parameters of Khuff sample 4 decreased after the treatment e.g., mean, maximum, etc. (see Table 9). Generally, Young's modulus of the samples saturated with deionized water prior to the treatment reduced after treatment.

The left image of Figure 19 is the SEM of the Khuff formation sample before the treatment with the microemulsion. The carbon coating could be distinguished inside the yellow circles and it caused the brightness of the SEM images. After the treatment, the grains seemed like they were rapped by a plastic film as displayed in the right image. The little enhancement in sample 1 and sample 3 was a result of the glueing of the grains together by the microemulsion.

Table 9: Statistical summary of sample 4 Young's modulus measurements.

Parameter	Microemulsion Solution	
	Young's Modulus Before (Gpa)	Young's Modulus After (Gpa)
Mean	7.9	6.1
Standard Deviation	1.4	1.1
Range	6.6	6
Minimum	5.3	2.2
Maximum	11.9	8.2
Count	100	

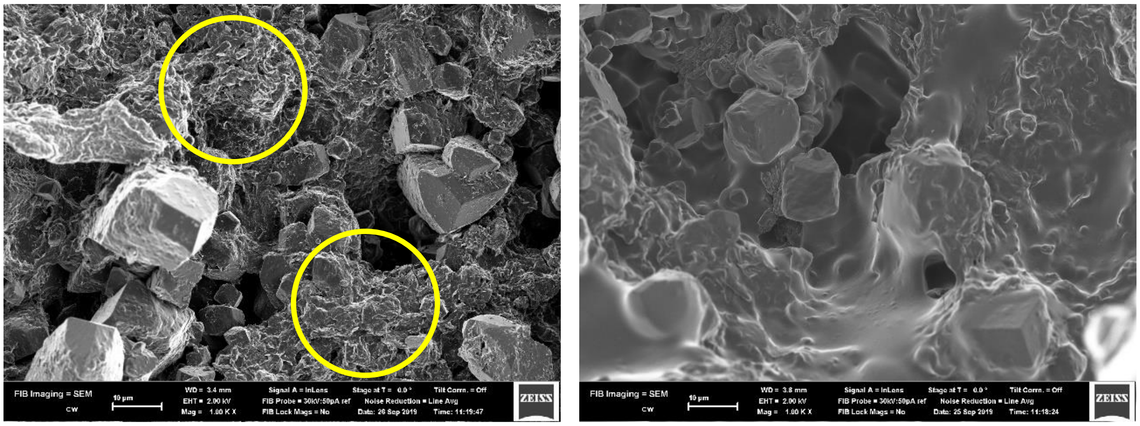

Figure 19: SEM images of the Khuff samples before and treatment with microemulsion solution.

4.2 Nanocrystals Solutions

Two colloidal dispersions of nanometric $Ca(OH)_2$ were used in this study and employed as consolidating products. The nanocrystals have hexagonal plate-shape (100 nm in size) and a concentration of 25 g/l immersed either in ethanol or isopropyl alcohol.

4.2.1 Calcium Hydroxide Nanoparticles Immersed in Ethanol Solution

Starting with Khuff limestone, sample 5.1 was saturated with deionized water then impregnated with the nanocrystal particles dispersed in ethanol twice and left in the open air for 5 days. The hardness was not improved (see Table 10), and the mean value decreased by 5% (see Figure 20). The maximum value of the measurement remained the same whereas the minimum value increased by 35%.

Table 10: Statistical summary of sample 5.1 Young's modulus measurements.

Parameter	Ethanol $Ca(OH)_2$	
	Young's Modulus Before (Gpa)	Young's Modulus After (Gpa)
Mean	6	5.7
Standard Deviation	1.1	1.3
Range	6.7	5.9
Minimum	2.4	3.2
Maximum	9.1	9.1
Count	100	

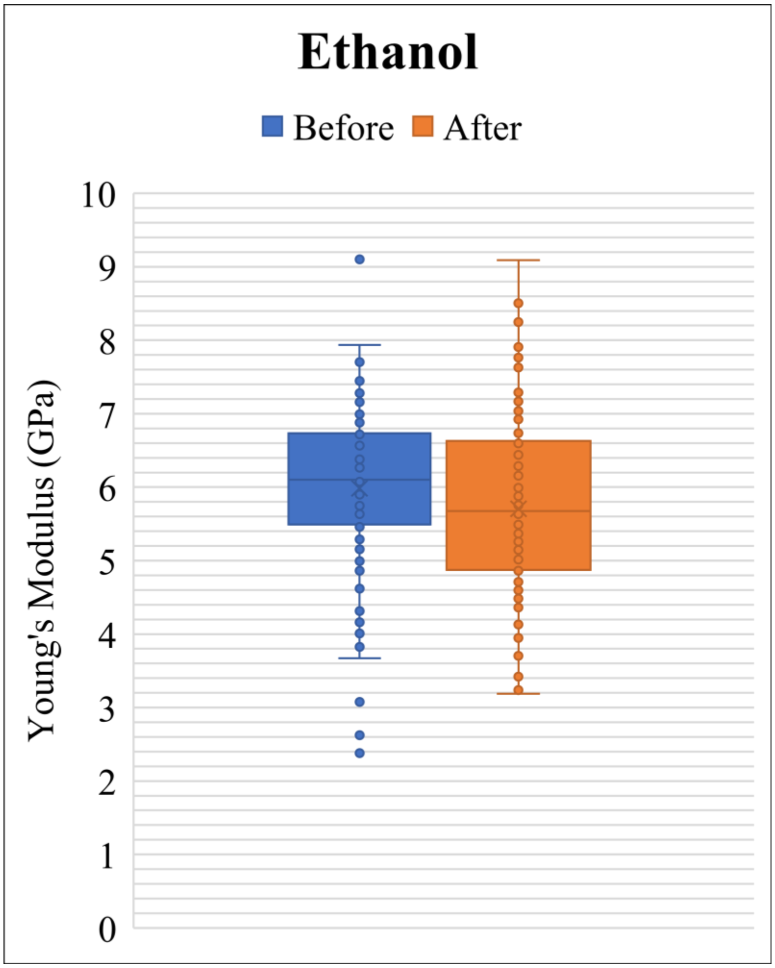

Figure 20: Khuff sample 5.1 Young's modulus before and after treatment with nanocrystals in ethanol at ambient RH.

Khuff sample 5.1 was treated after saturating it with water to study the effect of different initial conditions of samples on the consolidation process. The reduction in the sample strength may be due to the corrosive effect of water on the sample. Another reason that may explain this reduction is the instability of the nanocrystals in water. Thus, no sample had been saturated in the next set of experiments before the treatment with the nanocrystals solutions.

The treatment of Indiana limestone samples 3L and 3S was performed at slightly different conditions. The samples were dry and after impregnation with the solution they were left in temperature humidity oven for 5 days at ambient temperature and 75% RH.

Mean values of hardness measurements of the small and large samples increased by 9.56% and 9.12% respectively (see Figures 21 and 22). The permeability mean values of these samples underwent a decrease of 54.92% and 52.13%.

The box chart compares the whole data sets of the large Indiana limestone sample hardness measurement before and after the treatment.

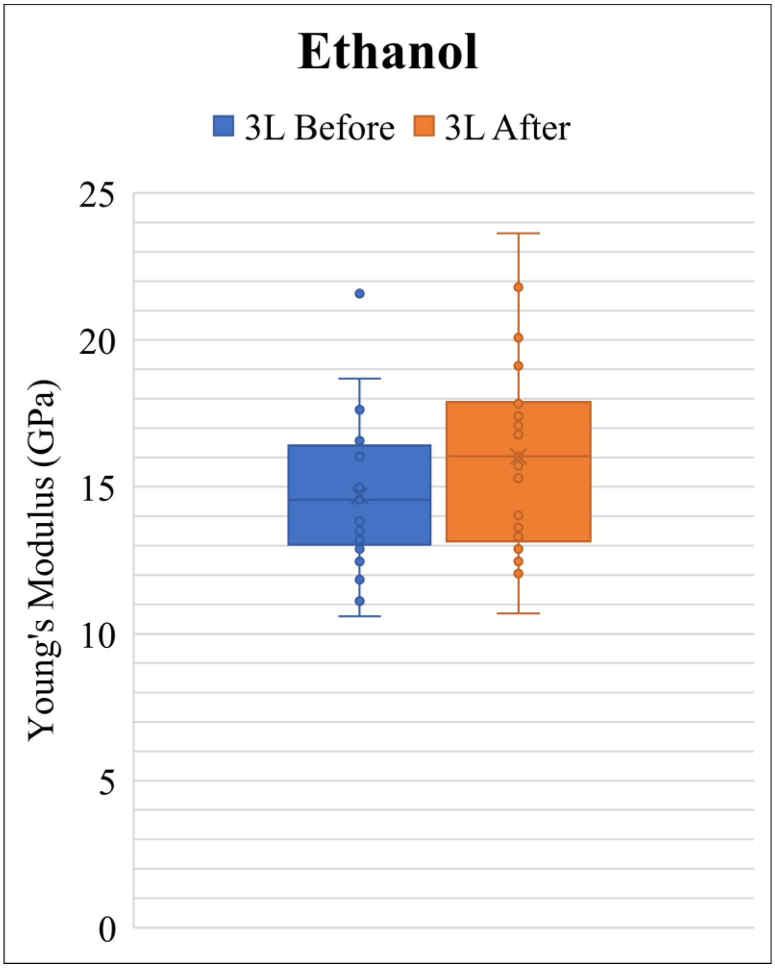

Figure 21: Indiana limestone sample Young's modulus before and after treatment with nanocrystals in ethanol at ambient RH.

Also, the next histograms in Figure 22 compare the distribution of these measurement sets. The shifting of the measurement values at x-axis to the right after treatment represents the enhancement in Young’s modulus happened with treatment. For instance, the maximum value of Young’s modulus before treatment was 19 GPa then became 21 GPa after the treatment. Also, the count increased from 1 to 3 which confirmed the enhancement of the rock strength.

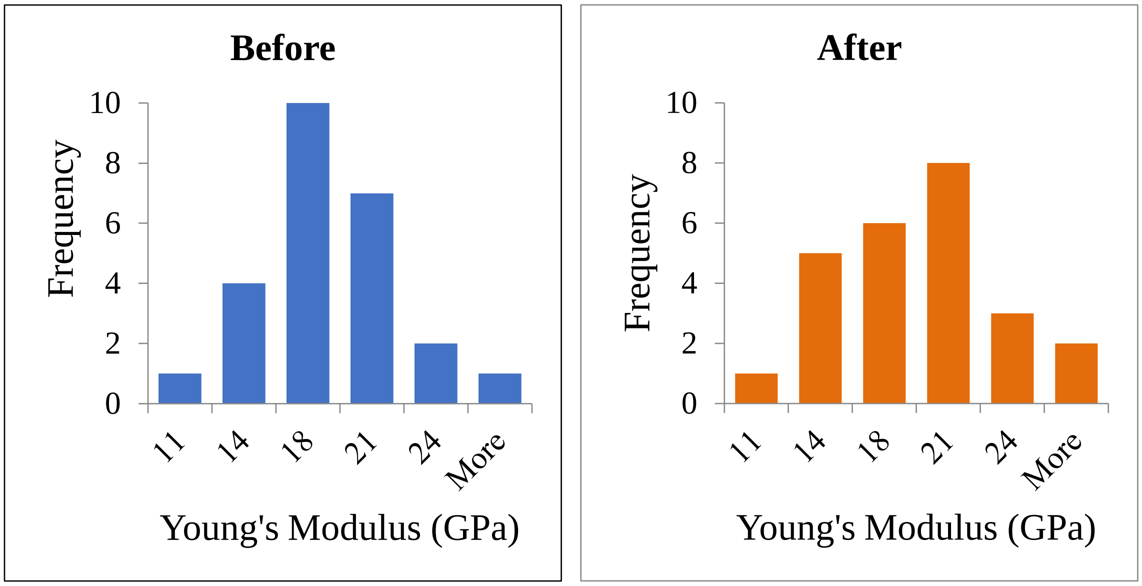

Figure 22: Comparison of the distribution of Indiana limestone Young's modulus measurements before and after treatment with nanocrystals in ethanol at ambient RH.

4.2.2 Calcium Hydroxide Nanoparticles Immersed in Isopropyl Solution

Khuff Limestone sample 5 was dry when treated with the nanocrystals in isopropyl solution. An increase of 14.59% between Young's modulus mean values before and after treatment was observed (see Table 11).

Table 11: Statistical summary of sample 5 Young's modulus measurements.

Parameter	Isopropyl $Ca(OH)_2$	
	Young's Modulus Before (Gpa)	Young's Modulus After (Gpa)
Mean	5.6	6.4
Standard Deviation	1.3	1.1
Range	6.3	5
Minimum	2.6	4.1
Maximum	8.9	9
Count	100	

Also, the minimum value of Young's modulus before treatment was 2.6 GPa and has increased to 4.1 GPa after the treatment. This is a dramatic increase of 58% while the maximum values before and after the treatment remained almost the same as shown in Figure 23.

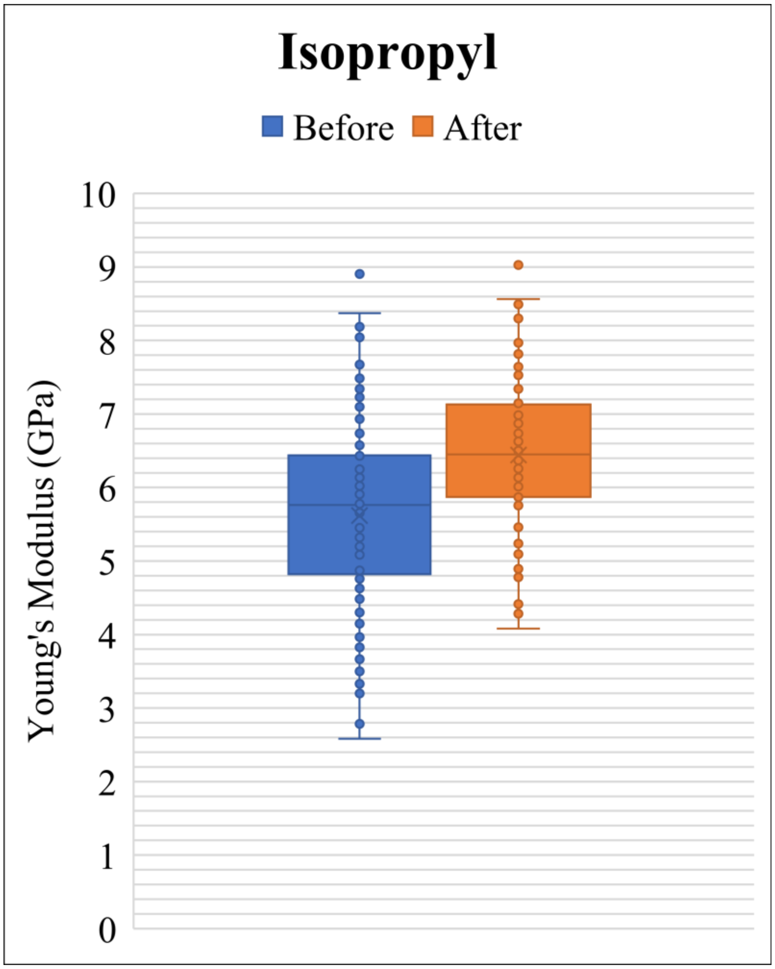

Figure 23: Khuff sample Young's modulus before and after treatment with nanocrystals in isopropyl at ambient RH.

For Indiana limestone samples 4L and 4S, the results of the small and the large samples were consistent with the khuff formation results as they increased by 16.95% for the small one and 15.77% for the large one (see Figures 24 and 25). Young's modulus minimum and maximum values of Indiana limestone large sample 4L before and after treatment with Isopropyl nanocrystals experienced similar change as these of Khuff. Young’s modulus minimum value increased by 37% after the treatment. Also, the decrease in permeability is roughly similar to the samples treated with ethanol nanocrystals solution with a decrease equals to 53.82% for the small sample and 47.32% for the large one.

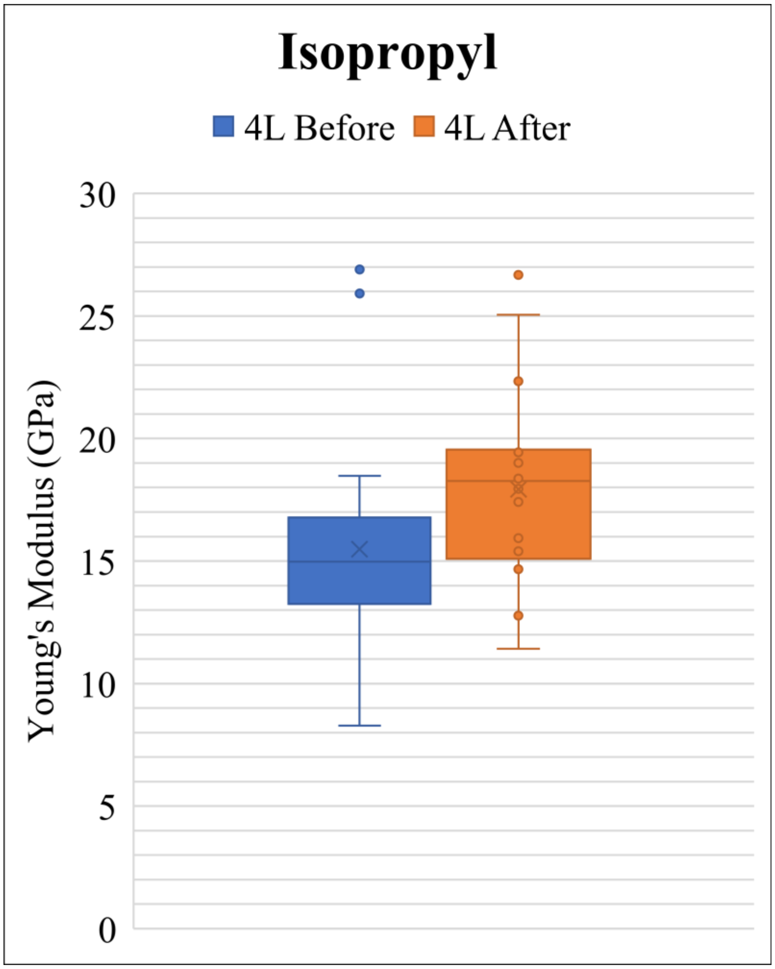

Figure 24: Indiana limestone sample Young's modulus before and after treatment with nanocrystals in isopropyl at 75% RH.

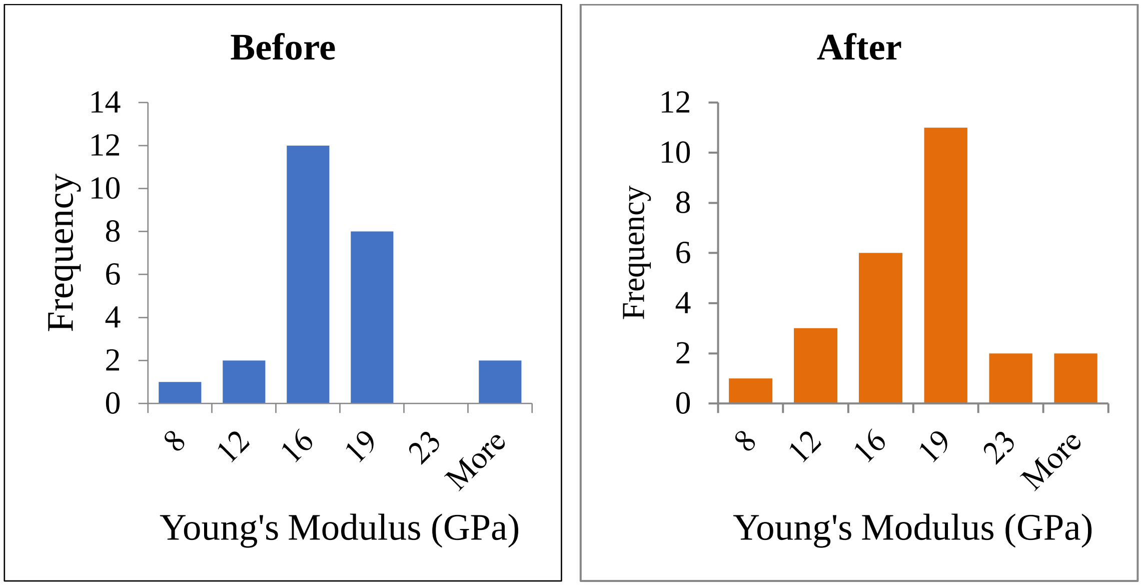

Figure 25: Comparison of the distribution of Indiana limestone Young's modulus measurements before and after treatment with nanocrystals in isopropyl at 75% RH.

The Indiana limestone samples 7L and 6S were treated at vacuum oven with 0% RH. The mean values of Young’s modulus after treatment increased by 13.48% and 38.56% for the large and the small samples respectively. The humidity role in the consolidation process is to lessen the evaporation of the alcohols so that the crystallization happens gradually. This emphasized the repeatability of treatment at different humidity values as illustrated in Figure 26.

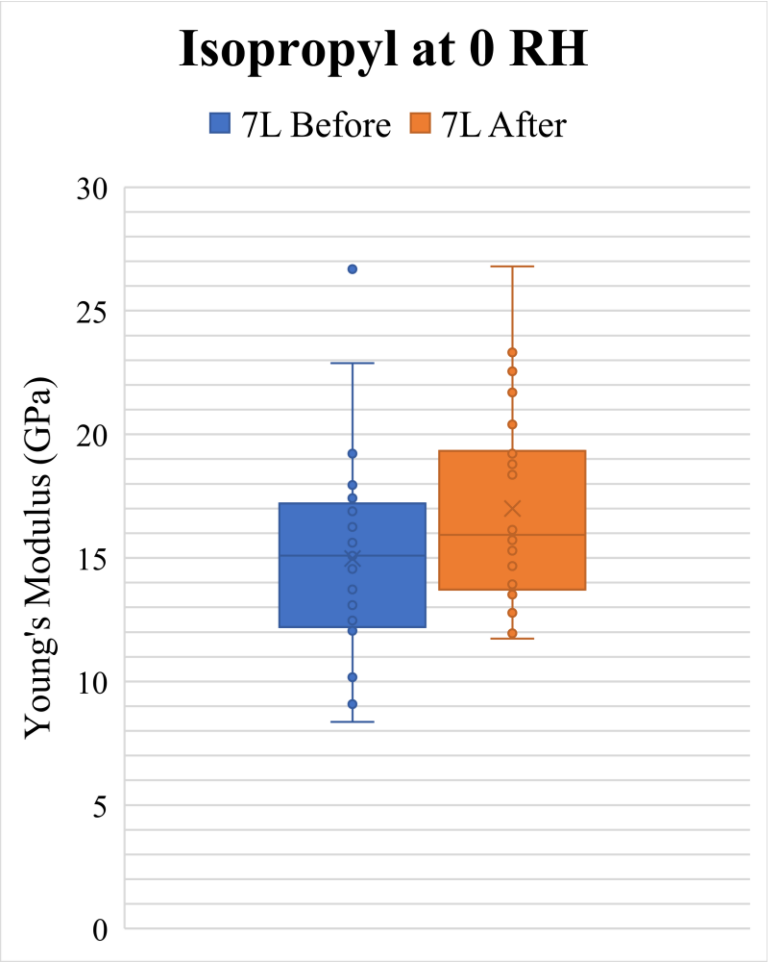

Figure 26: Indiana limestone sample Young's modulus before and after treatment with nanocrystals in isopropyl at 0 RH.

SEM image of cubic khuff sample 1 before the treatment showed the calcite grains obviously as illustrated in the left image of Figure 27. Also, some salt crystals inside the yellow circles can be seen scattered on the surface of the grains. The salts might be deposited from the tap water that cooled the cutting slab of the electric saw during cutting the samples. The debris between the grains of calcite resulted from the grinding effect of the slab. The right image of Figure 27 illustrates how the cubic sample 2 surface changed after the treatment with nanocrystal solutions. The nanocrystals almost covered the sample surface and filled the pores. This filling reduced the permeability by different amounts.

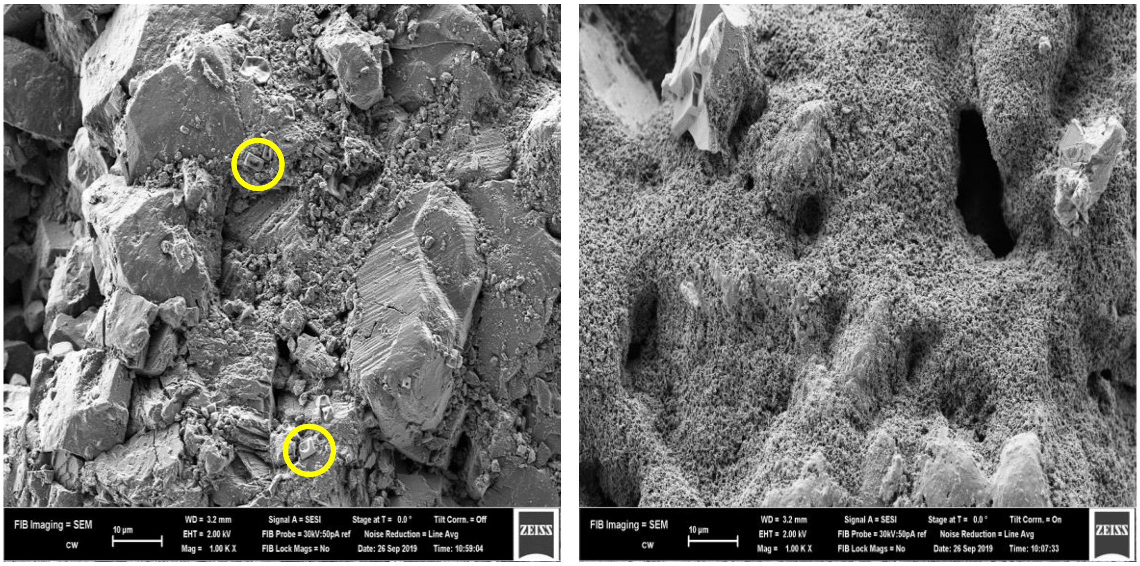

Figure 27: SEM images of the Khuff samples before and treatment with nanocrystals solutions.

A closer look at the treated surface of cubic sample 3 reveals that different calcium carbonate polymorphs have been formed (see Figure 28). The left image crystals take the lens or needle shape which is a habit of vaterite. The right image shows calcite with rhombohedral shape inside the yellow circle in addition to the branching shape. This could be aragonite but more investigation like Raman spectroscopy should be done to ensure that. Also, XRD could be useful in specifying the different calcium carbonate polymorphs. A micro-drill could be used to pick the crystals to be analyzed by XRD. The enhancement of the rock strength came from the crystallization of the nanocrystals. The interlock of the deposited calcium carbonate strengthened the surface.

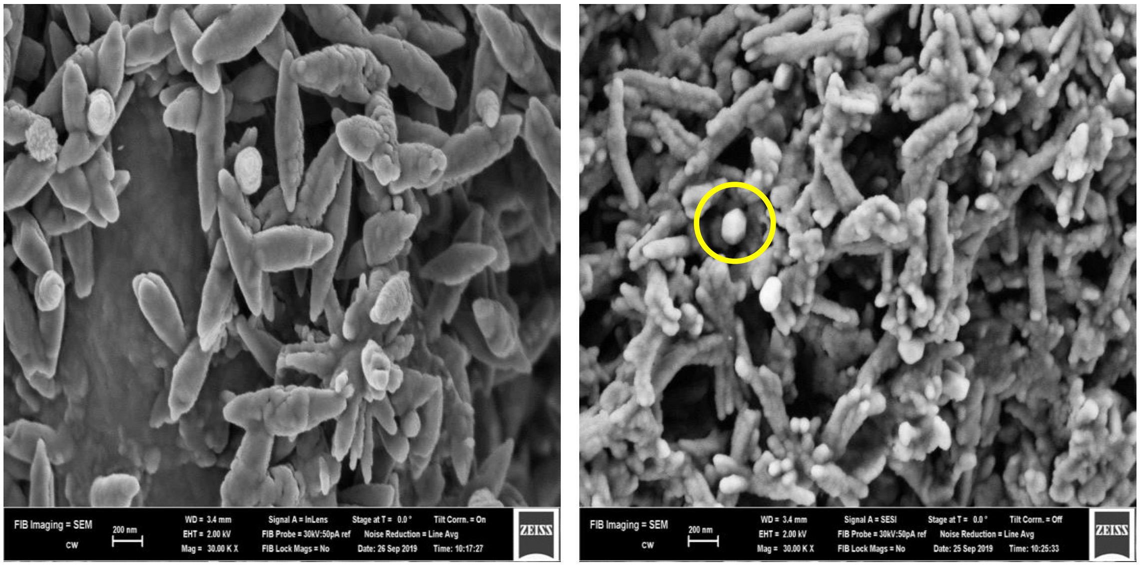

Figure 28: Different types of calcium carbonate crystals formed on the surface of the sample after treatment with nanocrystals solutions.

4.3 Zinc Solutions

The aim of using zinc chloride solutions is to incorporate the zinc instead of the calcium in the calcite crystals. Different zinc solutions were tried to accomplish the transformation of calcite ($CaCO_3$) to smithsonite ($ZnCO_3$).

4.3.1 Zinc Chloride

Indiana limestone samples 1L and 1S were dipped in the zinc chloride solution for 48 hrs. A decrease in the samples weights was observed after treatment as the zinc chloride dissolution in water formed an acidic solution that resulted in dissolving of the calcite. The zinc chloride solution etching process is described in the next equations:

The first equilibrium generated free protons and carbonate group.

$$ZnCl_{2\,(s)} + CaCO_{3\,(S)} \overset{H_2O}{\rightleftarrows} (Zn[OH]_2)_{(aq)} + (2Cl^- + Ca^+) \downarrow + (CO_3^{2-} + 2H^+)$$

The protons and the carbonate group formed another equilibrium with a proton and bicarbonate group. Finally, the carbonic acid dissociated into water and carbon dioxide.

$$(CO_3^{2-} + 2H^+) \rightleftarrows HCO_3^- + H^+ \rightleftarrows H_2CO_3 \rightarrow H_2O_{(l)} + CO_{2\,(g)} \uparrow$$

As a result of this etching, the strength of the rock was decreased after the treatment by 7.07% for the small samples and 8.53% for the large samples. Figure 29 shows how the mean value of sample 1L Young's modulus lessened.

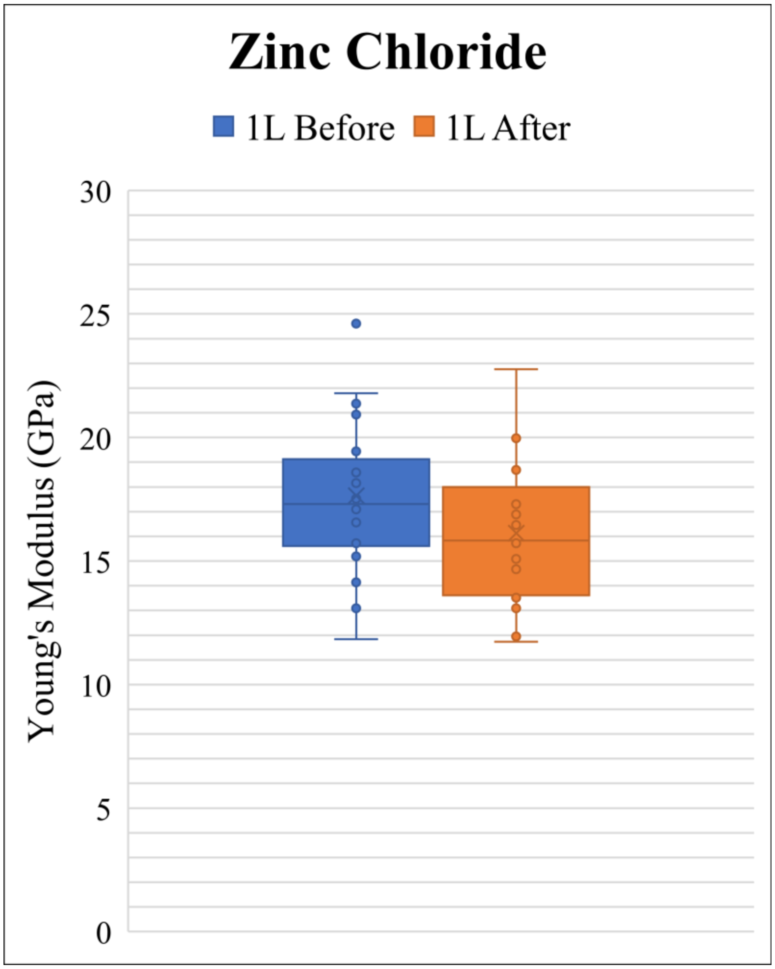

Figure 29: Indiana limestone sample Young's modulus before and after treatment with zinc chloride.

In Figure 30, SEM image of cubic khuff sample 1 before the treatment is placed next to cubic sample 4 which was treated with the zinc chloride. Deposition of white compound covered roughly half of the surface area. XRF showed chlorine and zinc enrichment on the surface of the treated samples when compared with the untreated on. Scanning the surfaces of plugs from the same core showed variations in the elements and their amounts on these surfaces. Thus, the white compound deposited on the surface couldn’t be identified due to these variations. To avoid the confusion that might happen due to these variations, the rest of the samples were scanned by XRF before and after each treatment.

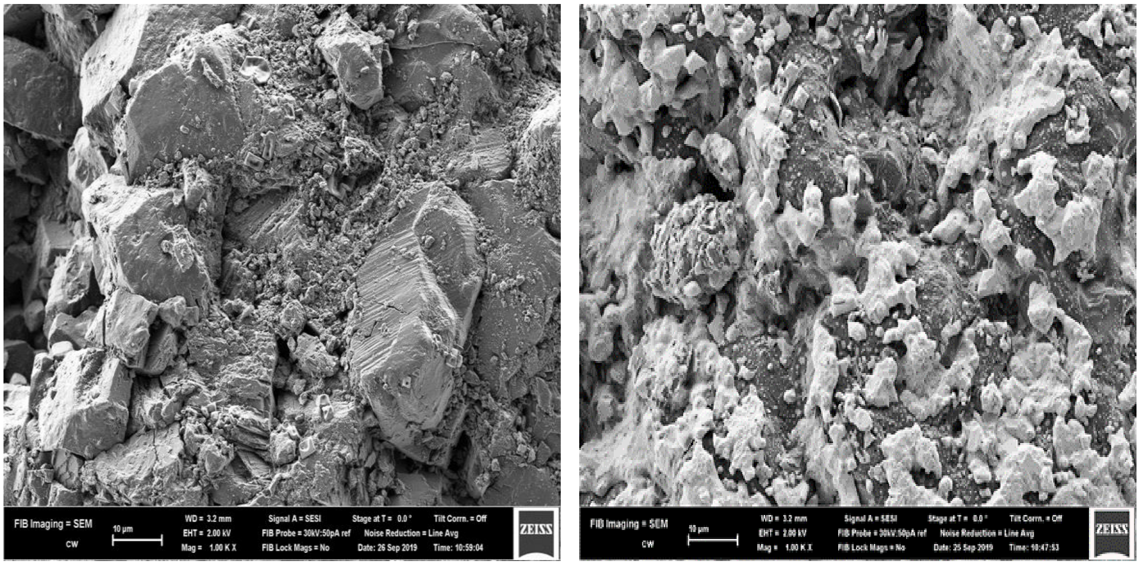

Figure 30: SEM images of the Khuff samples before and treatment with zinc chloride solution.

4.3.2 Zinc Sulfate

At first, the small Indiana limestone sample 2S after treatment showed an increase in strength by 35% whereas the large sample 2L only increased by 3% (see Figure 31). The treatment fluid volume was not enough to completely react with the sample surfaces. Thus, the treatment was repeated again with a larger zinc sulfate solution to ensure a full reaction with sample 6L.

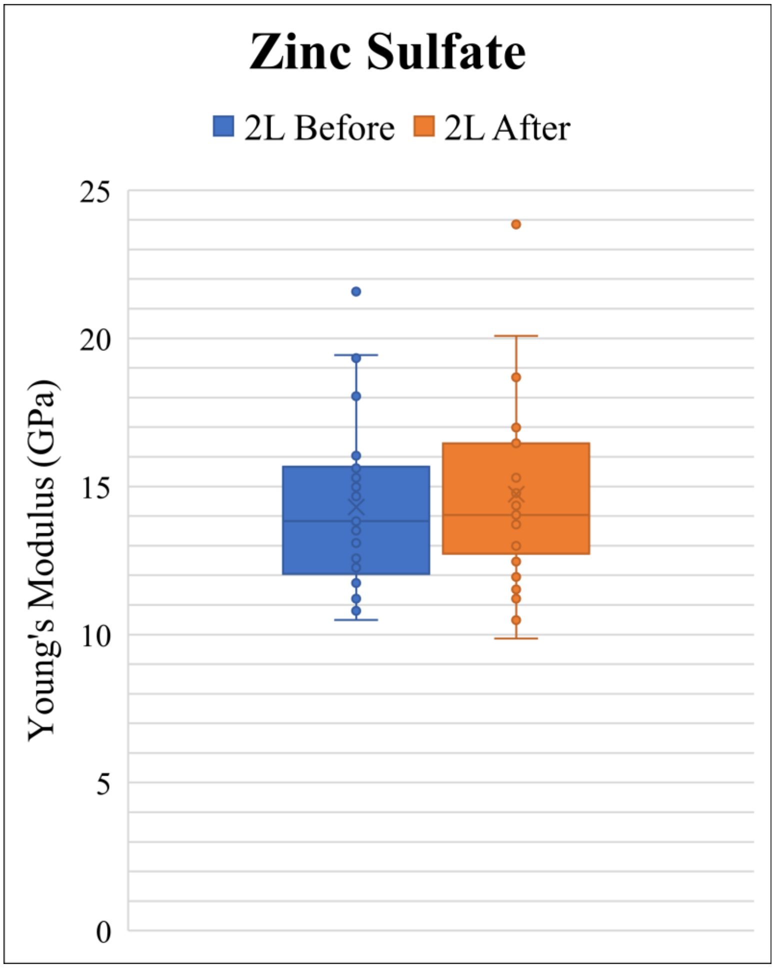

Figure 31: Indiana limestone sample Young's modulus before and after treatment with zinc sulfate.

As a result of repeating the treatment with a larger volume of zinc sulfate solution, the mean value of Young's modulus measurements increased by 25.8% (see Figure 32).

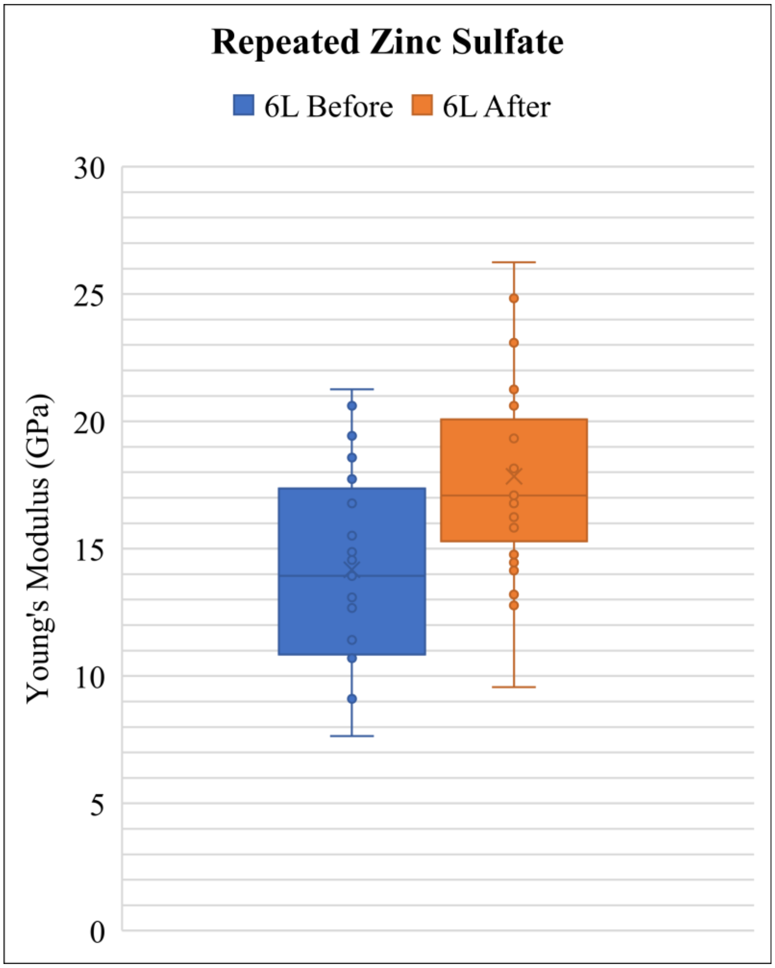

Figure 32: Indiana limestone sample Young's modulus before and after repeated treatment with zinc sulfate.

The treated and untreated Indiana limestone samples were put next to each other for comparison in Figure 33. In the left, SEM image of untreated Indiana limestone where the grains are obvious. In the right, the treated surface of another sample shows different crystals covering the surface.

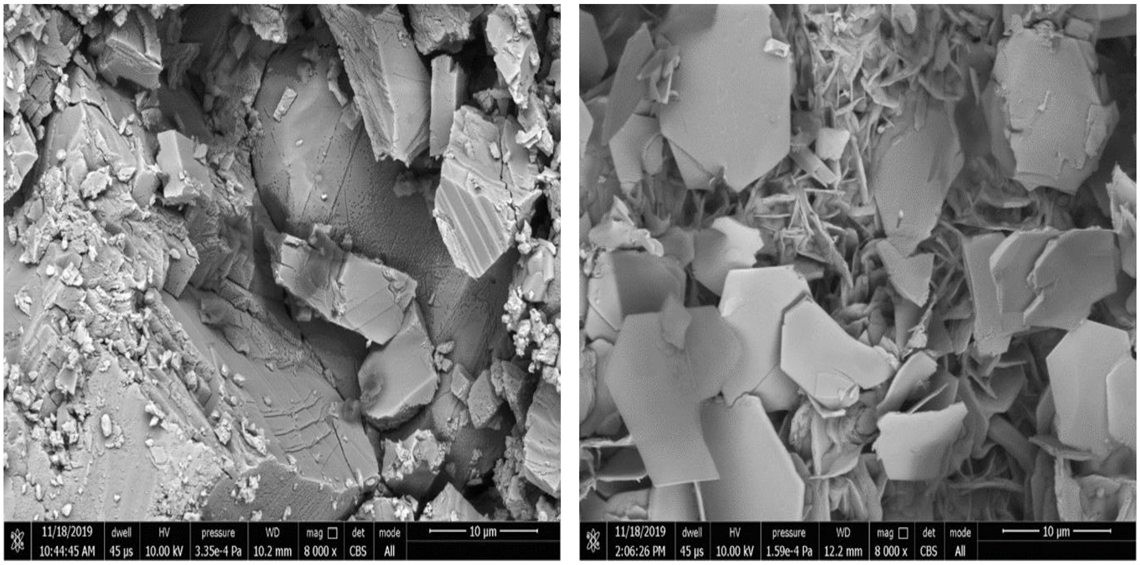

Figure 33: SEM images of Indiana limestone samples before and after treatment with zinc sulfate solution.

To define what elements compose these different crystals, EDS (Energy-dispersive X-ray spectroscopy) was run at different spots. The samples were covered by gold (Au) in the preparation for imaging. Thus, Au peak was expected to appear in the EDS. Two main crystal shapes were dominating the treated surface and both would be investigated.

The polygons were the first crystals to be investigated. An X mark was put in the centre of one of these nice polygons as illustrated in Figure 34.

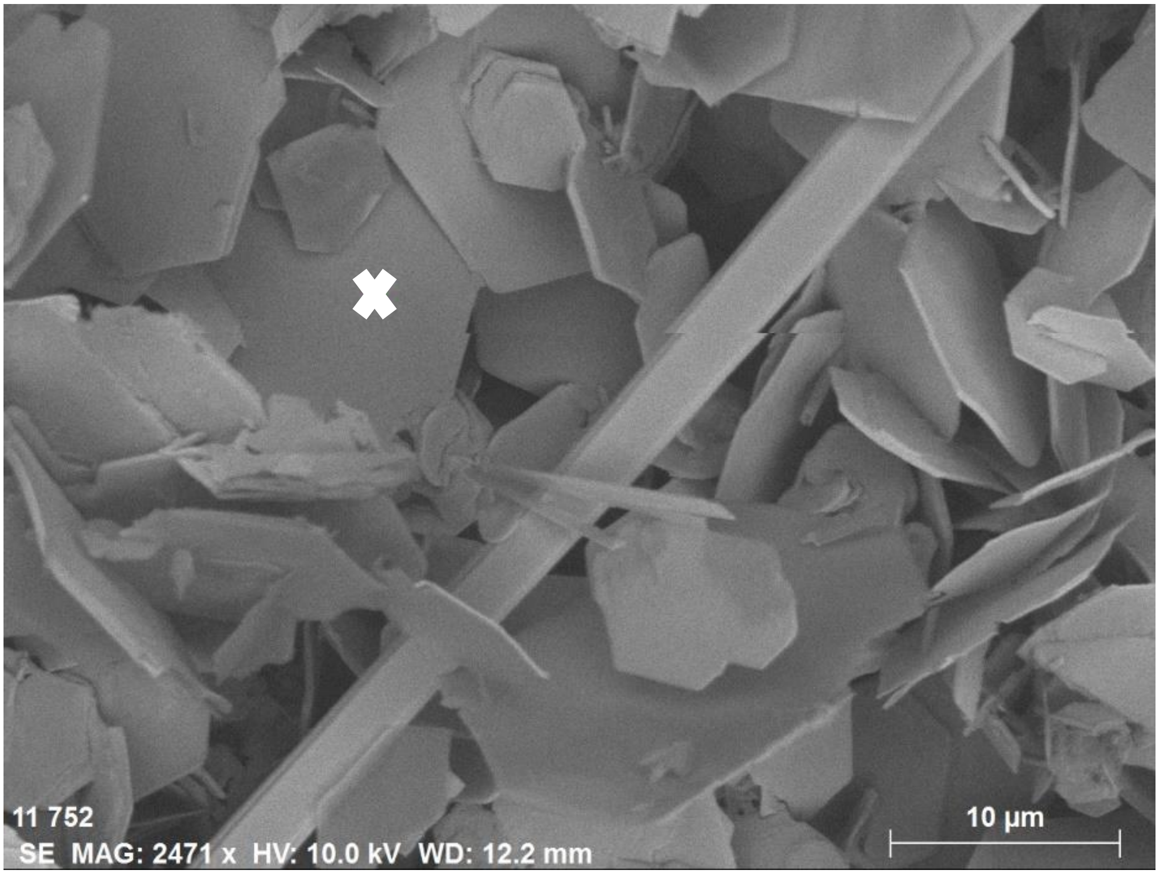

Figure 34: Sodium chloride crystal.

The two major alpha peaks belonged to the sodium and the chlorine (see Figure 35). Thus, these crystals were sodium chloride crystals. The reason for sodium chloride presence that the preparation of the zinc sulfate solution was done by mixing zinc chloride solution with a sodium sulfate solution.

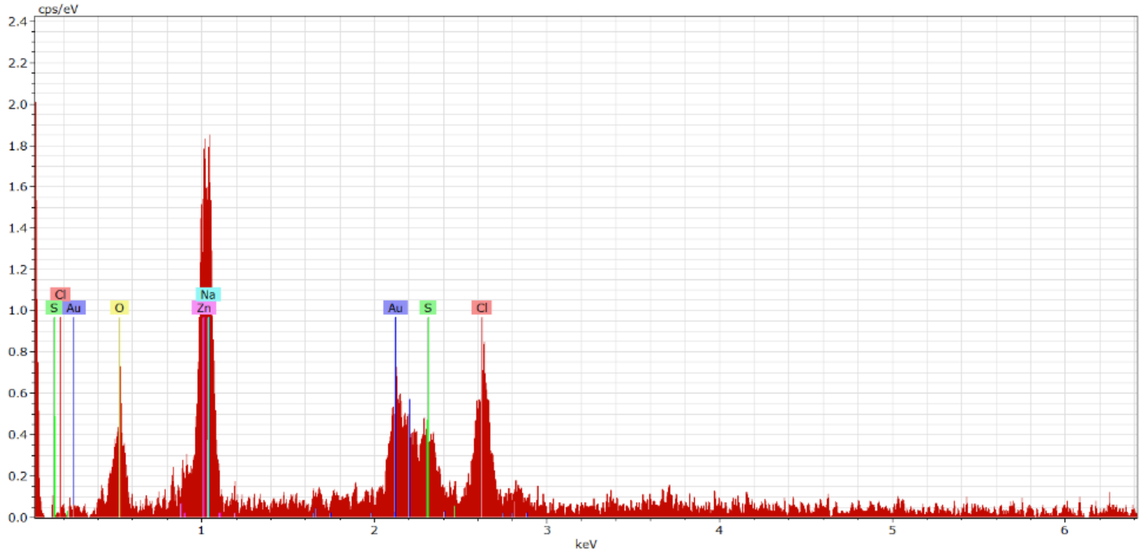

Figure 35: EDS at the X mark of figure 34.

Another X mark was put at one of the second dominating crystals as shown in Figure 36.

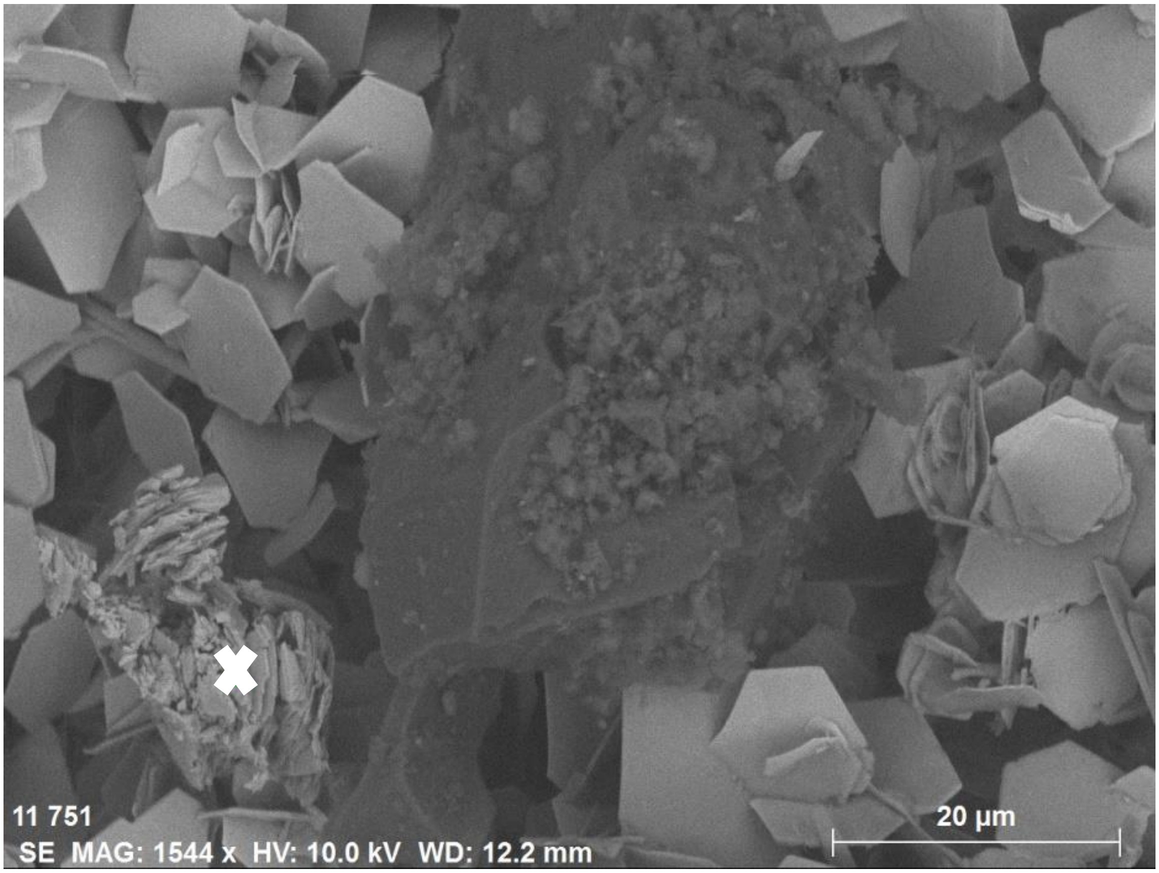

Figure 36: Calcium sulfate crystal.

EDS peaked at calcium, sulfur and oxygen as can be observed in Figure 37. Therefore the second crystals type was gypsum ($CaSO_4$). The gypsum is a by-product of zinc sulfate with calcite and its presence favours the formation of zinc carbonate. The XRF was run to confirm that the reaction has occurred and the smithsonite has been formed.

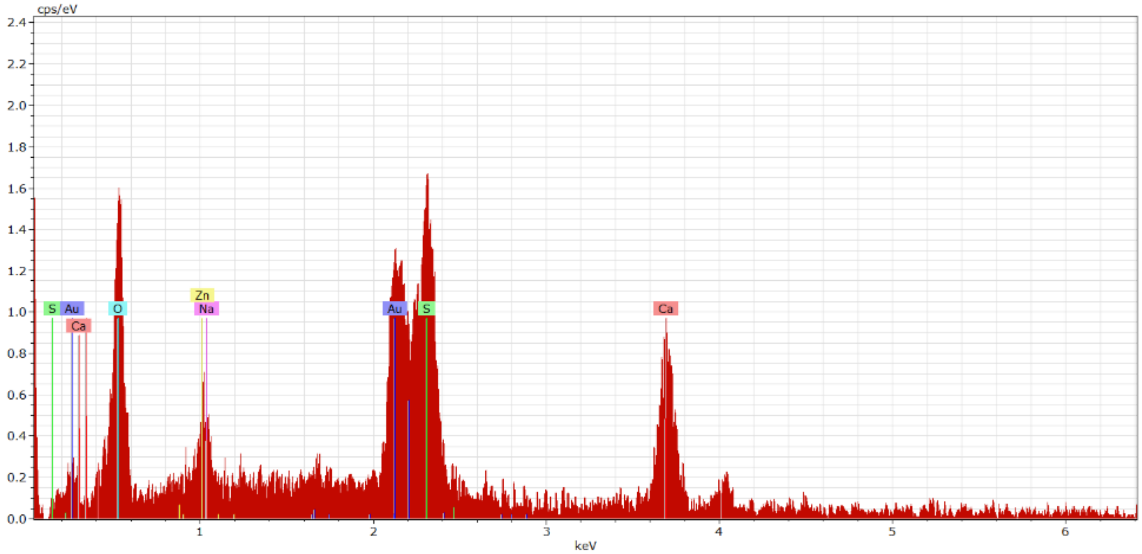

Figure 37: EDS at the cross mark of figure 36.

The elemental mapping by M4 Tornado as illustrated in Table 8 showed an increase in the zinc, sodium and chlorine elements while calcium and sulfur elements have decreased. M4 Tornado offers an option to quantify the elements carbonates in the scanned samples. This option could ensure the formation of the smithsonite after the treatment. First, the elements should be checked in the periodic table and the system will scan the surface to detect their carbonates. If not all elements attached to carbonate groups is checked, the system will normalize the elements carbonates amounts that are detected so that their sum will be 100%. Thus, this XRF option will be used only to investigate the change in elements carbonate. In other words, this is a comparative analysis not a quantitative. The chief element carbonate on the surface of Indiana limestone is calcium carbonate. Before the treatment, there was no zinc carbonate on the surface. After the treatment, the calcium carbonate decreased greatly while the zinc carbonate appeared. Based on this in addition to table 12, a conclusion can be drawn that the zinc sulfate was able to change calcite into smithsonite.

Table 12: Indiana limestone surface elements change after treatment with zinc sulfate.

2.5 in	Before	After
Ca		
Zn	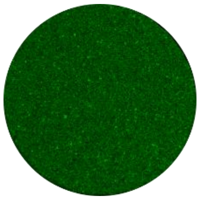	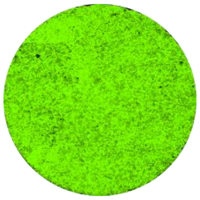
Na		
Cl	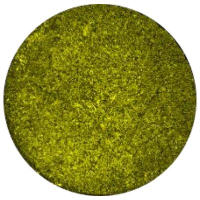	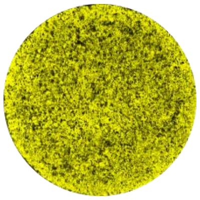
S	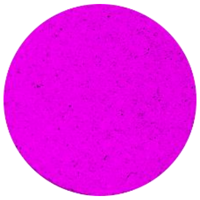	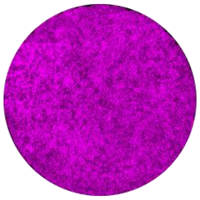

4.4 Tetraethyl Orthosilicate (TEOS)

Indiana limestone samples 5L, 5S and 8L were treated with TEOS. Sample 8L surface was treated with the solution without dilution which caused a rise in Young’s modulus mean value from 14.26 to 16.08 as revealed in Figure 38.

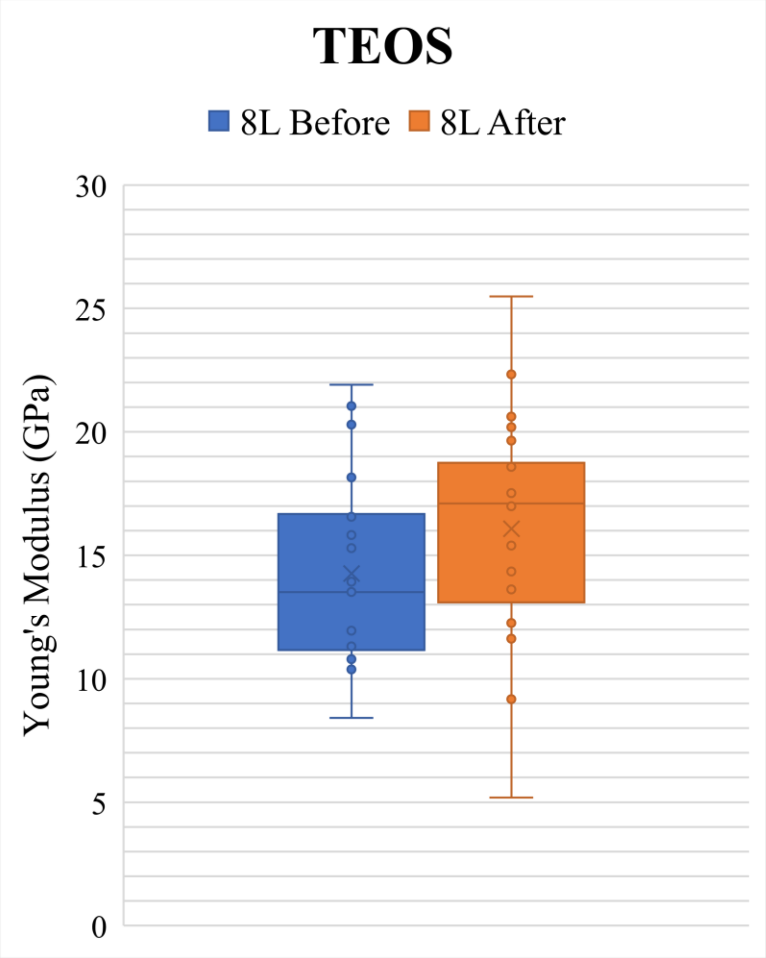

Figure 38: Indiana limestone sample Young's modulus before and after treatment with raw TEOS.

TEOS was diluted with water to 10% of the raw solution concentration. Small and large samples number five were dipped in the diluted TEOS which resulted in an increase in Young’s modulus by 6.13% and 18.99% respectively. Figure 39 illustrates the change of sample 5L measurements with treatment.

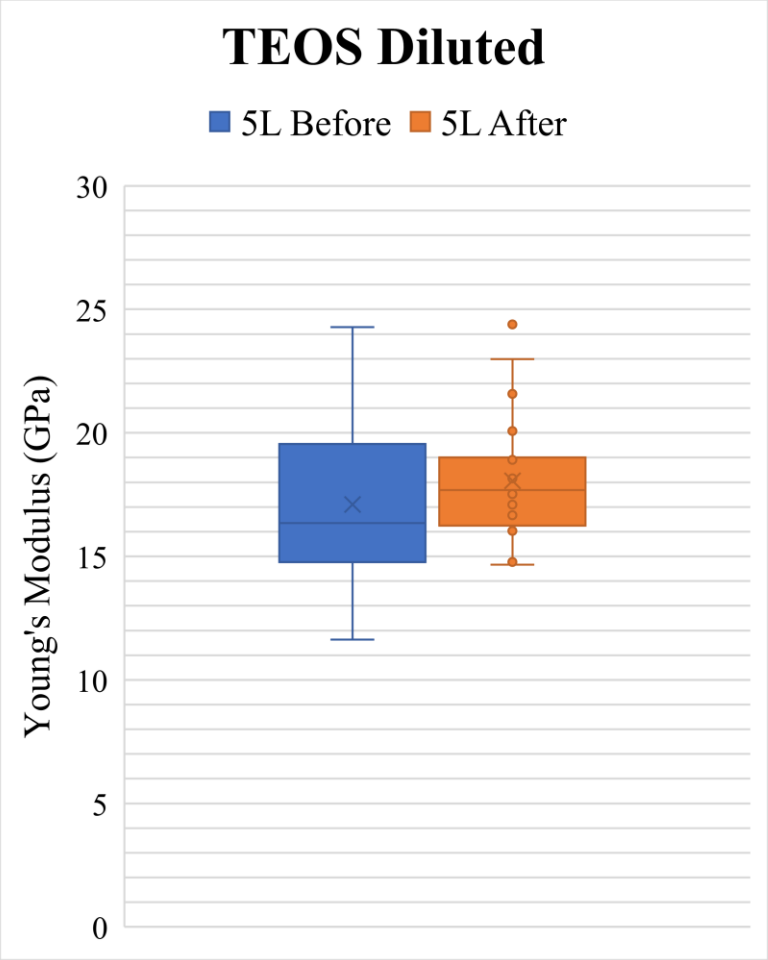

Figure 39: Indiana limestone sample Young’s modulus before and after treatment with diluted TEOS.

The TEOS reaction with carbonate is not fully understood. Also, the SEM images in Figure 40 do not show a clear distinction between the treated and the untreated samples.

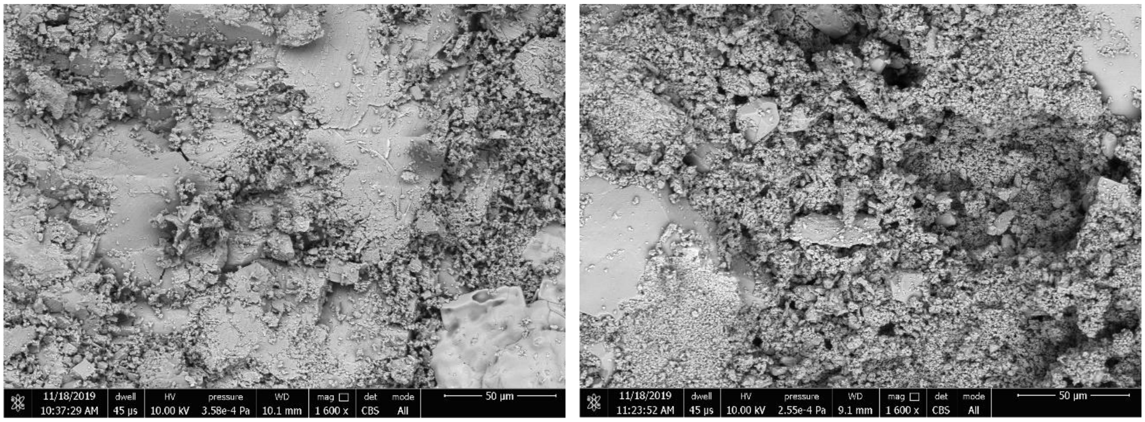

Figure 40: SEM images of Indiana limestone samples before and after treatment with TEOS solution.

The first two columns of Table 13 display the samples and their treatment systems. The next two columns show samples' Young's modulus before and after treatment. The last two columns give the change value and change percentage in Young's modulus for each sample. The strength of all samples was enhanced except for 1L, 1S and 5.1.

Table 13:Summary of Young’s modulus change for all samples after treatment.

Sample ID	Treatment Fluid	Young's (Gpa) Before	Young's (Gpa) After	Change	Change %
1L	**$ZnCl_2$**	17.64	16.13	-1.51	-8.53
1S	**$ZnCl_2$**	9.04	8.40	-0.64	-7.07
2L	**$ZnSo_4$**	14.31	14.73	0.42	2.95
2S	**$ZnSo_4$**	9.00	12.18	3.18	35.38
6L	**$ZnSo_4$ (Double)**	14.18	17.84	3.66	25.82
5.1	**Ethanol (Wet)**	5.99	5.71	-0.28	-4.68
3L	**Ethanol**	14.70	16.04	1.34	9.12
3S	**Ethanol**	8.10	8.88	0.77	9.56
5	**Isopropyl**	5.62	6.44	0.82	14.59
4L	**Isopropyl**	15.49	17.93	2.44	15.77
4S	**Isopropyl**	9.64	11.27	1.63	16.95
7L	**Isopropyl (Zero Humidity)**	14.98	17.00	2.02	13.48
6S	**Isopropyl (Zero Humidity)**	10.04	13.91	3.87	38.56
5L	**TEOS**	17.10	18.15	1.05	6.13
5S	**TEOS**	10.26	12.20	1.95	18.99
8L	**TEOS (Without Dilution)**	14.26	16.08	1.82	12.76

The summary of permeability changes of small and large Indiana limestone samples measured by AutoScan can be found in table 14. All treatments led to a decrease in permeability, but TEOS treatment showed the contrast. a hypothesis was proposed to justify this behaviour. It states that at grain defects e.g., grain contacts, it is most likely to have free hydroxyl groups in calcite lattice. Thus, TEOS will bind grains together leading to strength enhancement. Also, TEOS strips the rock throats from clays resulting in the increase in permeability value. This hypothesis needs to be tested to prove if it is true.

Table 14: Summary of the permeability change for Indiana limestone samples.

Sample ID	Treatment Fluid	K (mD) Before	K (mD) After	Change	Change %
1L	**$ZnCl_2$**	4.66	1.79	-2.88	-61.67
1S	**$ZnCl_2$**	6.45	2.23	-4.22	-65.47
2L	**$ZnSo_4$**	14.57	10.55	-4.01	-27.54
2S	**$ZnSo_4$**	4.62	2.26	-2.36	-51.08
6L	**$ZnSo_4$**	13.47	6.27	-7.20	-53.47
3L	**Ethanol**	10.04	4.80	-5.23	-52.14
3S	**Ethanol**	5.94	2.68	-3.26	-54.92
4L	**Isopropyl**	18.69	9.85	-8.84	-47.32
4S	**Isopropyl**	6.94	3.21	-3.74	-53.82
7L	**Isopropyl (0 Humidity)**	14.67	3.31	-11.36	-77.45
6S	**Isopropyl (0Humidity)**	5.94	3.24	-2.70	-45.48
5L	**TEOS**	11.57	13.00	1.43	12.35
5S	**TEOS**	6.94	10.04	3.10	44.67
8L	**TEOS (Without Dilution)**	16.01	20.52	4.51	28.18

Samples treated with TEOS exhibits an increase in permeability after treatment when measured with AutoScan. Thus, the small sample permeability measurement was repeated twice with the gas permeameter which confirmed that the permeability has not changed as can be seen in Figures 41 and 42.

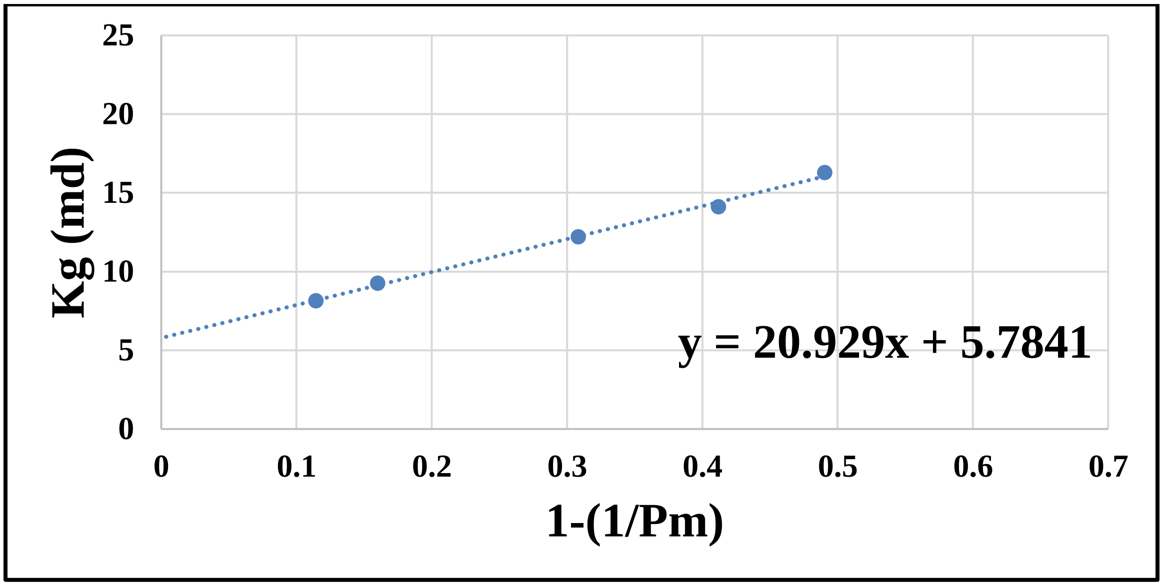

Figure 41: Sample 5S permeability before treatment.

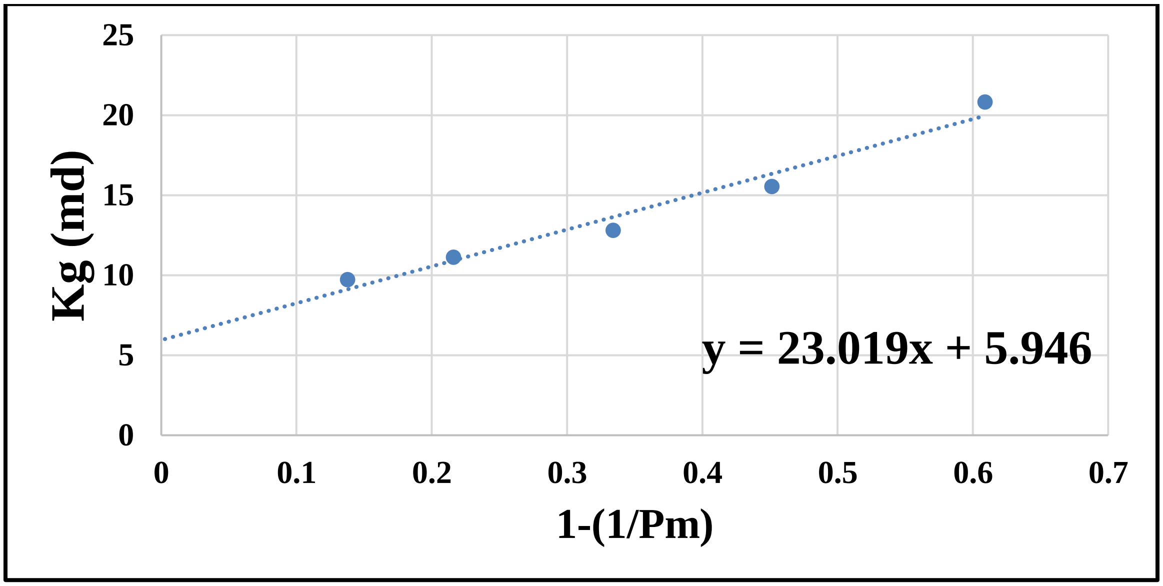

Figure 42: Sample 5S permeability after treatment.

Depending on how the AutoScan and the gas permeameter measure the permeability, their estimations for TEOS permeability were coherent. The TEOS might change only the surface where the AutoScan measures the sample permeability. The sample interior might be unchanged be TEOS treatment. Thus, the gas permeameter showed no change in permeability with treatment.

The porosity of the samples barely exhibited any change with the treatment except for those treated with zinc chloride as shown in Table 15. Permeability may be reduced dramatically while the porosity shows a slight decrease. This was the situation for most of the performed treatments, as a minute precipitates at throats lowered the permeability significantly while the porosity of these samples underwent a minor decrease.

Table 15: Summary of the porosity change for small Indiana limestone samples.

Sample ID	Treatment Fluid	Ø % Before	Ø % After	Change	Change %
1S	**$ZnCl_2$**	17.09	15.09	-2	-11.7
1S	**$ZnSo_4$**	17.05	16.79	-0.26	-1.5
2L	**Ethanol**	17.16	17.21	0.05	0.29
2S	**Isopropyl**	16.54	16.62	0.08	0.48
5S	**TEOS**	17.11	17.13	0.02	0.12

CHAPTER 5

CONDUCTIVITY PREDICTION USING MACHINE LEARNING TECHNIQUES (MODELLING RESULTS)

A successful design of an acid fracture job requires accurate prediction of fractured well productivity. Productivity estimation requires knowledge of both the acid penetration length and conductivity distribution for a given reservoir. The literature includes several models that were developed to predict the conductivity of acid fractured rock. Those models are based on empirical, semi-empirical, analytical, and numerical approaches. The most popular model is empirical and it is based on measuring the conductivity of 25 acid fracture experiments. Empirical models were developed that utilized machine learning techniques in this research using more than 140 experiments and 500 data points. The empirical models were developed utilizing machine learning workflow as illustrated in Figure 43.

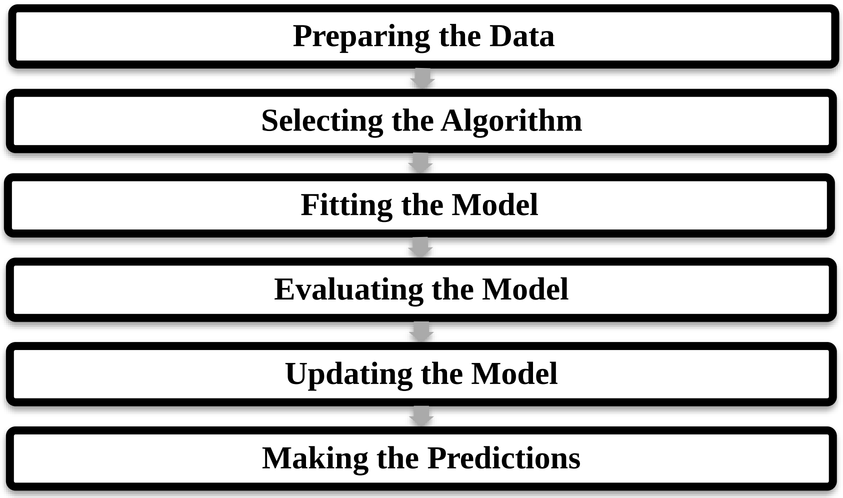

Figure 43: Modeling workflow.

Most of the derived models ignore the resulted etching pattern, original surface roughness and treatment conditions. Almomen (2013) showed that rough-surface fractures generate higher conductivity by an order of magnitude compared with a smooth-surface fracture at low-closure stress. Thus, ignoring such factors surely will give simple models but these models will be inaccurate and biased. In the sections below, the significance of considering the etching pattern on the accuracy of conductivity prediction is illustrated. It is also found that considering the rock type is as significant.

5.1 Modelling Workflow

5.1.1 Preparing the Data

An extensive literature review was conducted to collect the published data of acid fracture experiment. The objective of the acid fracture experiment is to measure the conductivity at different formation closure stresses, mimicking field conditions (e.g., rock type, acid type, injection rate, treatment volume, etc.). The conditions are scaled down to represent the field conditions experimentally. The rock types and their initial surface conditions were tabulated along with the treatment conditions (e.g., temperature, injection time, etc.). After that, the etching pattern and the conductivity at each load were compiled to complete the data set. Therefore, the gathered data should be consistent as it came from the same set up with the modified API RP-61 conductivity cell. Outliers and failed experiments were excluded to get the data in the proper shape to build a model. Table 16 is a subset of the gathered data and the full data set is included in Appendix C.

Table 16: Sample of the collected data.

X^1	X^2	X^3	X^4	X^5	X^6	X^7	X^8	X^9	Y
Chalk	GelledAcid	Rough	Channelling	175	1	30	15	3000	90
Chalk	Straight	Smooth	Turbulence	175	1	5	15	100	2778
Dolomite	GelledAcid	Smooth	Rough	130	0.5	20	15	500	127
Dolomite	GelledAcid	Smooth	Rough	130	0.5	20	15	1000	104
Limestone	GelledAcid	Rough	Rough	175	1	30	15	5000	72
Limestone	Emulsified	Smooth	Rough	200	1	15	15	1000	1597

The physical properties, meanings and measuring units of Xs are described in Table 17.

Table 17: The physical meaning of each feature.

X^1	**Rock Type**	Rocks etched by different acids.
X^2	**Acid Type**	Acid systems used to etch the rocks.
X^3	**Rock Surface**	Initial rock surface before acid etching.
X^4	**Etching Pattern**	Manner of rock surface behaviour after acid etching.
X^5	**Temperature**	The temperature of etching acid in F^o.
X^6	**Injection Rate**	Rate of pumping acid through API conductivity cell in litre per minute.
X^7	**Injection Time**	Time of pumping acid through API conductivity cell in minutes.
X^8	**Acid Concentration**	The concentration of etching acid pumped through API conductivity cell as a percentage.
X^9	**Stress**	Applied stress by the loading frame in psi.
Y	**Conductivity**	The resulting rock conductivity under stress in md-ft.

In Table 16 there were different types of predictors or features among the gathered data e.g., categorical and numerical. In the full data set, the different numerical features range differed. For instance, the range was from 100-275 F^o for the temperature to 0-7500 psi for stress. Stress range was roughly 43 times larger than temperature range. So, these two features were in very different ranges. When further analyses were to be conducted, like multivariate linear regression, the attributed stress would intrinsically influence the result more due to its larger value. But this did not necessarily mean it was more important as a predictor. The predictors were considered as $\{\boldsymbol{X^1}, \boldsymbol{X^2}, \ldots\ldots, \boldsymbol{X^n}\}$ (where the superscript is an index ranging from 1 to the total number of predictors $\boldsymbol{n}$). Each predictor $\boldsymbol{X}$ contained $\boldsymbol{m}$ of data points $\boldsymbol{x_i}$ (where the subscript $\boldsymbol{i}$ is an index ranging from 1 to the total number of points $\boldsymbol{m}$). The aim of normalization was to alter these $\boldsymbol{X}$s in the dataset to a common scale without deforming the differences in the values ranges. Therefore, prior to modelling, normalizing numeric features by subtracting their means and scaling it to unit variance was done as per the next equation:

$$\boldsymbol{z_i} = \frac{\boldsymbol{x_i - \mu}}{\boldsymbol{\sigma}} \tag{5.1}$$

Where $\boldsymbol{z_i}$ is the z-score or the normalized value of each data point, $\boldsymbol{\mu}$ is the mean value of each predictor $\boldsymbol{X}$ and $\boldsymbol{\sigma}$ is the standard deviation of this predictor.

The Pearson correlation coefficient between two different features is a measure of association degree between these features. They were calculated to better understand the data. The correlation coefficient between each numerical predictor and the conductivity values of all rock types is summarized in Table 18. the second column represents the correlation coefficients in case of considering all conductivity values of rock types. While the next three columns represent each rock type separately. For all the rock types, the conductivity is inversely proportional with the stress and directly proportional with the injection time, injection rate and temperature. The zero-correlation coefficient between the conductivity and any feature means that this feature was constant when measuring the conductivity. For instance, chalk conductivity measurement was taken at a single injection rate and acid concentration. The lower row indicates that chalk conductivity is most affected by stress then limestone and finally comes the dolomite. This goes in tandem with the rock strength as the chalk is the softest and the dolomite is the hardest. The temperature seems to increase the conductivity of all rock type equally.

Table 18: Summary of the correlation coefficients between conductivity and each feature.

Feature	All Rocks Conductivity	Chalk Conductivity	Dolomite Conductivity	Limestone Conductivity
Temperature	0.33	0.32	0.28	0.30
Injection Rate	0.12	0.00	0.27	0.00
Injection Time	0.11	0.19	0.10	0.01
Acid Concentration	0.00	0.00	-0.19	-0.04
Stress	-0.53	-0.76	-0.47	-0.67

Another way to visualize the correlations among the features and between each feature and the response is by using the heatmaps (see Figure 44). First, the absolute values of correlation coefficients were calculated. Then, the colour bar to the right was added to represent the degree of correlation(e.g., blue means no correlation, yellow means high correlation, green means moderate correlation, etc.). The data may contain highly correlated predictors so that only one of them needs to be included in the model. In high dimensional problems and when the data is gathered from different sources, this may help in avoiding highly correlated predictors. For example, length in mm as a predictor and length in ft as another predictor are regarded as redundant features. The diagonal represents the correlation between the feature with itself and it is always one. Any off-diagonal yellowish square represents a high correlation between features, but this was not present in this work. The correlation coefficients were moderate and there were no redundant features.

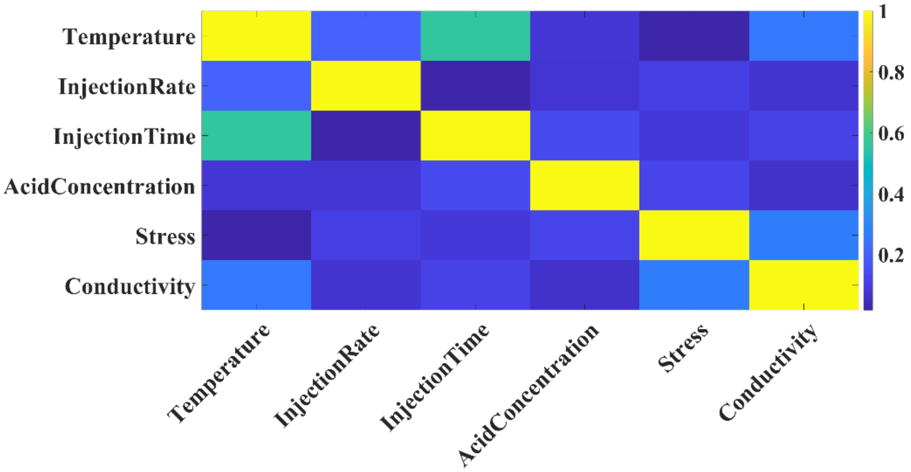

Figure 44: Correlation coefficients between each pair of numeric features

Pearson correlation coefficient and Spearman correlation coefficient are used for the numeric variables. Exploring the correlation between two categorical variables is different from the correlation between two numeric variables. For this purpose, the Chi-squared test is used. For investigating the correlation between the categorical and numerical variables, other methods like Z-test can be utilized.

5.1.2 Selecting the Algorithm

Machine learning methods are divided into supervised learning and unsupervised learning. In supervised learning, a data set is given, and the correct output is already known how it should look like, providing that there is a relationship between the input and the output. Problems of supervised learning are divided into "regression" and "classification". In a regression problem, trials are made to predict results of continuous values, and this is the case in prediction the acid fracture conductivity. For a classification problem, trials are made to predict results in discrete categories.

A lot of supervised machine learning techniques could be used. Size and type of data might help in selecting the proper algorithm. In some cases, following the gut feeling and doing a lot of trials are the way of getting a promising technique. Also, your knowledge about the problem becomes handy when coming to select the best candidate algorithm.

Conventional machine learning techniques can produce useful models for most of the problems. Starting with multivariate linear regression to form the base upon which the subsequent models will be evaluated. It measures how the predictors, usually more than one, are related to the response. The essence of used regression used here is to reduce the cost function $\boldsymbol{J(\vec{\theta})}$ through gradient descent. The cost function is a measure of how wrong the model when estimating the response from the predictors. While the gradient descent is simply taking the derivative with respect to theta $\boldsymbol{\frac{\partial}{\partial\theta_j}J(\vec{\theta})}$ considering adding the regularization term. The hypothesis $\boldsymbol{h_\theta}$ the definition will differentiate between the linear and non-linear regression. The hypothesis function is sensitive to slight changes in coefficients. Thus, regularized linear regression arises to tackle this problem. Regularization is used to drop features that do not contribute to a good prediction.

The regularization term has different forms and the regression is named based on it as ridge, Lasso or elastic net. Fitting a linear regression model to data can result in coefficients with large variance. Regularization reduces the variance of the coefficients and can create models with smaller prediction error. That is, the coefficients' values change by a large amount as the training data changes. Here, the ridge regression will be used, and the cost function is defined as:

$$\boldsymbol{J(\vec{\theta}) = \frac{1}{2m}\sum_{i=1}^{m}\left(h_\theta\left(x^{(i)}\right) - y^{(i)}\right)^2 + \lambda\sum_{j=1}^{n}\theta_j{}^2} \tag{5.2}$$

Where $\boldsymbol{J(\vec{\theta})}$ is the cost function, m is the number of data points, $\boldsymbol{y^{(i)}}$ is the actual response at the data point $\boldsymbol{i}$, $\boldsymbol{\lambda}$ is the regularization parameter, $\boldsymbol{n}$ the number of predictors, $\boldsymbol{\theta_j}$ is the weight multiplied by the feature $\boldsymbol{j}$ and $\boldsymbol{h_\theta\left(x^{(i)}\right)}$ is the hypothesis.

The hypothesis consists of a combination of $\boldsymbol{X}$s multiplied by $\boldsymbol{\theta}$s depending on the design matrix.

5.1.3 Fitting the Model

The models will be trained on 80% of the data. Another portion of 10% of the data set is reserved to test and selecting the regularization parameter that makes the testing set error minimum. Comparison of different learning algorithms or methods can be done by calculating the loss for each method and pick the method with minimum loss. The loss is a metric to evaluate model performance. Common regression loss is mean squared error

(MSE) or mean absolute error (MAE). However, the loss is calculated on specific test data. It is possible that a learning algorithm performs well on that particular test data but does not generalize well to other data. Also, error and noise are not equally distributed among the data points. As the training and testing sets are randomly selected, the loss of trained models will differ from one run to another. To reduce the dependency of the model on certain random sets, the model should be trained several times with different training sets. Also, the loss should be calculated each time by the corresponding test set. Averaging the loss values over the number of training times give a reliable estimation of loss. This concept is called cross-validation and when repeated ***k*** times it is called k-fold cross-validation.

5.1.4 Evaluating the Model

To assess the built model and how it learns from the data, the mean square error (MSE), the correlation coefficient between the actual and the predicted values, learning curve and residual plot will be the evaluation metrics. Figure 45 emphasizes how the algorithm learns from the data with increasing training points (Ng 2011). High bias issue arises when the model is too simple and it is marked by high training and testing errors. Remedial actions can be done by adding polynomial features, using a larger set of predictors or decreasing the regularization parameter $\boldsymbol{\lambda}$. High bias issue originates when the model is too complicated and it behaves well only on the training set. Curing this issue can be done by gathering training examples, using a smaller set of predictors or increasing the regularization parameter $\boldsymbol{\lambda}$.

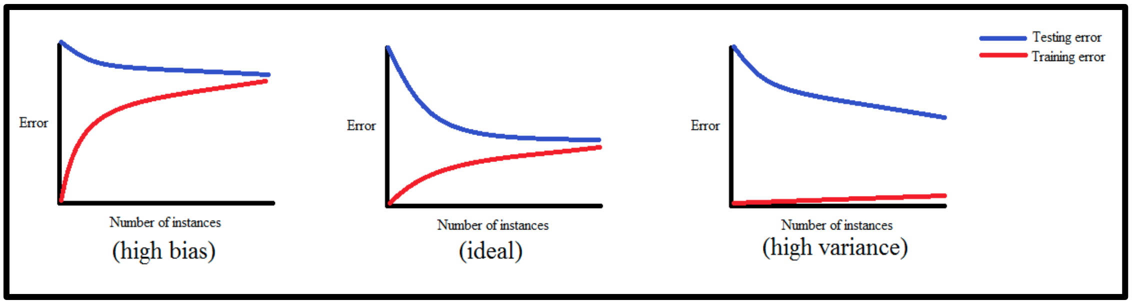

Figure 45: Underfitting (high bias), right fit and overfitting (high variance).

5.1.5 Updating the Model

Based on the mentioned metrics, the model will be updated by tweaking the regularization parameter and modifying the hypothesis. This process requires a lot of trials.

5.1.6 Making the Predictions

After developing the model, the last 10% of the data, which is never seen by the learning algorithm, is used to validate the model and give an insight into its performance.

5.2 Etching Patterns Classification

Having the treatment conditions only as tabulated in the first three columns of Table 19, it was possible to predict the etching pattern that would be generated.

Table 19: Categorical variables of acid fracture conductivity.

Rock Surface	Etching Acid	Rock Type	Etching Pattern
Chalk	GelledAcid	Rough	Channelling
Chalk	Straight	Smooth	Turbulence
Dolomite	GelledAcid	Smooth	Rough
Dolomite	GelledAcid	Smooth	Rough
Limestone	GelledAcid	Rough	Rough
Limestone	Emulsified	Smooth	Rough

The etching patterns occurrences and their probabilities are summarized in Table 20. Dolomite and chalk developed roughness after treatment more often than limestone which developed channels in less than have of the experiments. Also, limestone developed another three patterns with significant probabilities. This made the prediction of limestone conductivity a hard process.

Table 20: Frequency table to investigate the correlation between etching pattern and rock type.

	Channelling	Rough	Turbulence	Uniform	Total
Dolomite	5	125	8	0	138
	3.6%	90.6%	5.8%	0%	100%
Chalk	6	100	11	0	117
	5.1%	85.5%	9.4%	0%	100%
Limestone	85	142	33	30	290
	29.3%	49%	11.4%	10.3%	100%

The treatment conditions of the 97 acid fracture experiments were used as predictors to predict the corresponding etching pattern. Ensemble templates can be used to train a multiclass error-correcting output codes model (ECOC). The used template had three arguments which were the method, the number of learner and the learner. They have been specified in this way: the method as ‘GentleBoost”, the number of learner as 100, and the learner as decision trees. Rock surface, etching acid and rock type were used as predictors with 80% of the data (78 data points) to train the model. The last 20% of the data (19 data points) was used to test the classifier. The developed classifier had a test error of .0833. Also, the overall accuracy was 94.7% and all the precision and recall values are summarized in Figure 46. The corner square to the right of the figure shows the overall accuracy of the classifier. The rows are relevant to the output class (predicted) and the columns are relevant to the target class (actual). The diagonal squares represent the observations that were correctly classified. The off-diagonal squares refer to incorrectly classified observations. Observations count and their percentages are shown in each square. The rightmost column of the figure represents the percentages of all the observations predicted to belong to each class that were correctly and incorrectly classified. This metric is called precision. The bottom row of the figure represents the percentages of all the observations belonging to each class that are correctly and incorrectly classified. This metric is called the true positive rate (recall). The precision and the recall become more important when the data is skewed or unbalanced. For instance, the dolomite generated roughness etching pattern in 90.6% of the dolomite etching experiments. There was unbalance in the generated etching pattern. If an etching pattern classifier for dolomite only is set to always output roughness, the overall accuracy will be higher than 90%. Nevertheless, any other etching pattern is misclassified. Thus, the assessment of a classifier based on the overall accuracy only when having a severe class imbalance is not accurate.

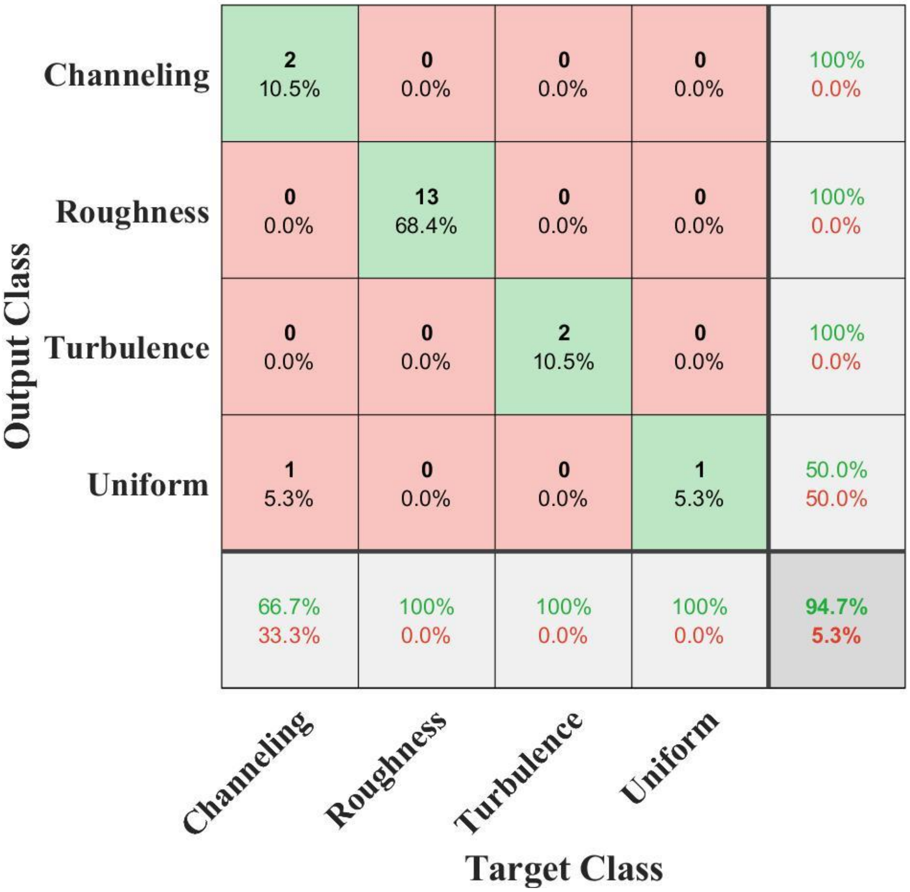

Output Class \ Target Class	Channeling	Roughness	Turbulence	Uniform	
Channeling	2 10.5%	0 0.0%	0 0.0%	0 0.0%	100% 0.0%
Roughness	0 0.0%	13 68.4%	0 0.0%	0 0.0%	100% 0.0%
Turbulence	0 0.0%	0 0.0%	2 10.5%	0 0.0%	100% 0.0%
Uniform	1 5.3%	0 0.0%	0 0.0%	1 5.3%	50.0% 50.0%
	66.7% 33.3%	100% 0.0%	100% 0.0%	100% 0.0%	**94.7%** **5.3%**

Figure 46: Confusion matrix of etching patterns classifier.

5.3 Conductivity Prediction

Fitting a linear model for all rock types and etching patterns resulted in inaccurate conductivity predictions. The correlation coefficient between the actual and predicted values was as low as 0.3726. Also, the residual plot confirmed that the model should be nonlinear as there is an obvious pattern (parabola) that can be seen in Figure 47 instead of randomly scattered points.

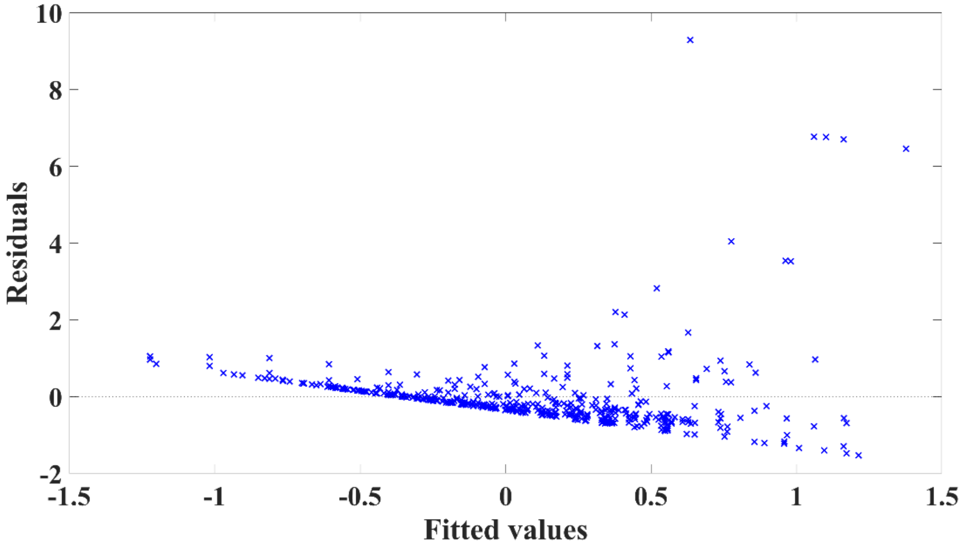

Figure 47: Residual plot of universal linear conductivity model.

Different rock types do not behave the same way even though the same treatment conditions are the same, thus each rock type conductivity will be studied separately.

A useful way of visualizing the data distribution and investigating the presence of outliers is the boxplot (Saleh et al., 2014; Li et al., 2017). The conductivity data sets of dolomite and chalk showed consistency and a few outliers whereas the limestone showed many distributed outliers as clarified in Figure 48.

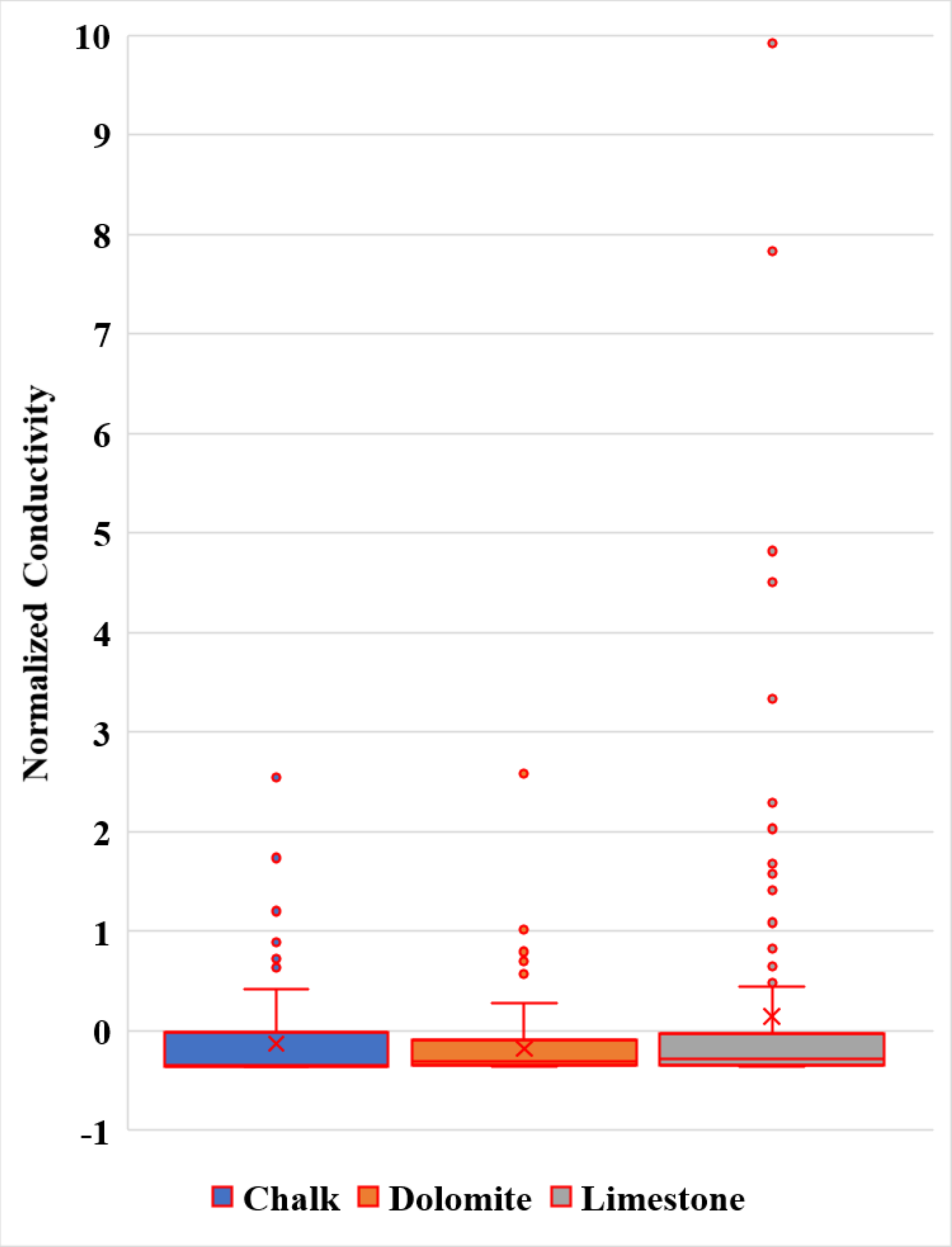

Figure 48: Boxplot of different rocks normalized conductivity values.

5.3.1 Conductivity Prediction of Dolomite

The data often contains predictors which do not have any relationship with the response. These predictors should not be included in the model. It is better to have a limited number of predictors yet nearly hold the complete variance of the data (Kazakov et al., 2011). Principal Component Analysis (PCA) converts a matrix into another of orthogonal components. Each component explains a percentage of the variation in the data. Then, the components are arranged descendingly based on this percentage. The first few predictors that hold a variance of a chosen threshold can be picked to reduce the number of predictors. These components do not have a physical meaning by themselves. Thus, the interpretation of the trained model with these components becomes harder.

Similarly, a way to pick the most relevant predictors to response is to train the model repeatedly while adding the predictors and monitoring the loss. At a specific point, adding more predictors does not increase the accuracy but increases the calculation time and memory consumption.

The acid type, rock surface and etching pattern were transformed into a dummy variable to make the whole data set homogeneous as numeric values. For instance, a categorical predictor that contains K categories will be transformed into K-1 predictors of zeros and ones.

Figure 51 shows the minimum number of predictors that are sufficient to get the lowest loss when training a polynomial model to predict conductivity for dolomite. Adding the temperature and the etching pattern decreased the loss significantly. Then the loss remained the same with adding rock surface and acid type.

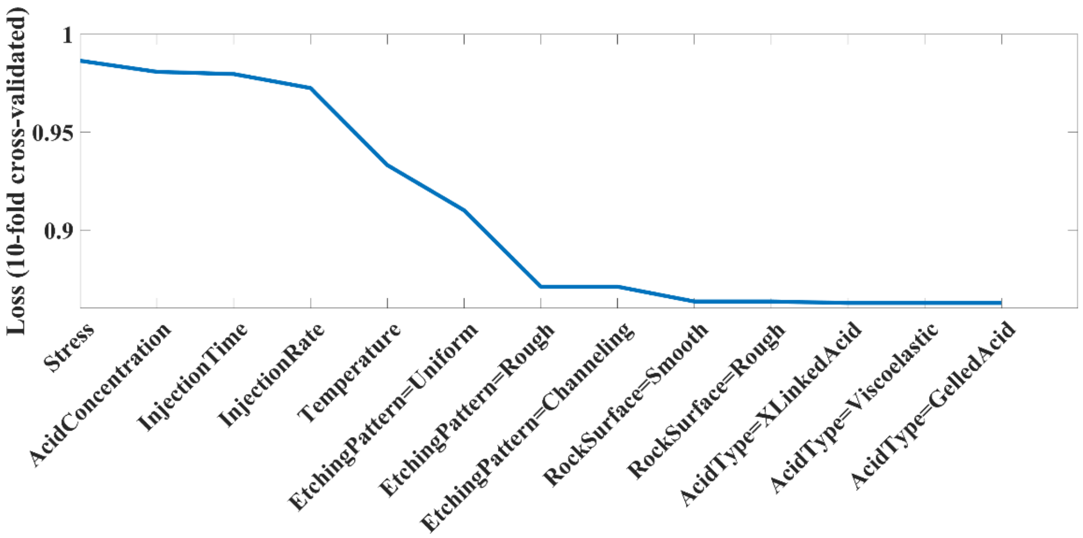

Figure 49: Lowest no. of predictors to get the least loss for dolomite.

The Pareto charts confirm this in another way as shown in Figure 50. The first 7 principal components explained more than 99% of data variance.

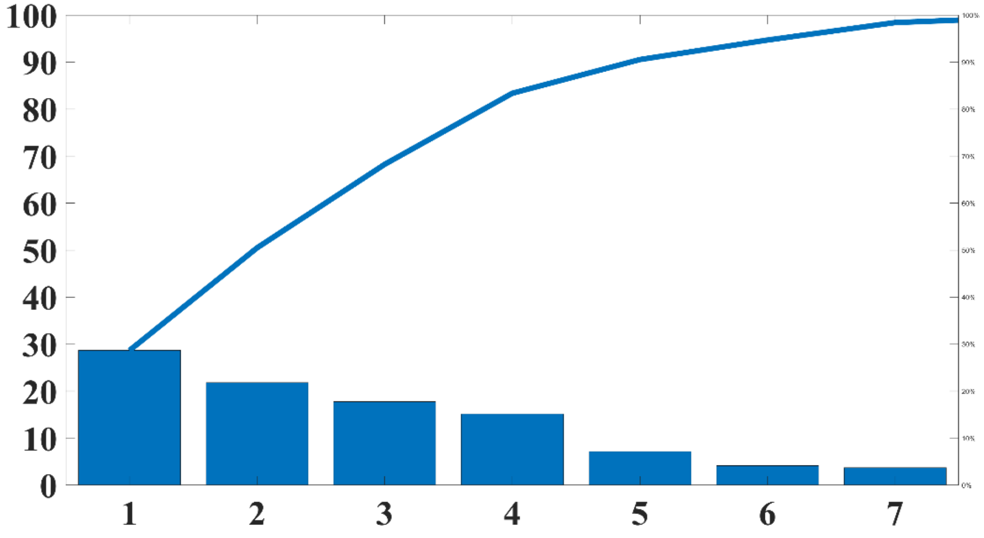

Figure 50: Principle component analysis of dolomite predictors.

The predictors that resulted in the least loss in Figure 49 were used to get the first dolomite model. The predictors starting from the “Stress” up to the “RockSurface=Roughness” were picked. The design matrix was built using the MATLAB software function “x2fx”. One of these four models: “linear”, “interactions”, “quadratic” and “purequadratic” should be specified first. These ten predictors matrix was converted to the design matrix by the model “quadratic”. The learning curve in Figure 51 shows high variance which cannot be addressed by regularization or simplifying the model. This means that more data is needed. The correlation coefficient between the fitted and the actual value was 0.9491 and the normalized MSE was 0.03. This model contained 52 parameters and would not be implemented easily. Thus, other models were trained with a different combination of predictors to get a simpler model with fair performance. Using the first four predictors starting with “stress” and ending with “InjectionRate”, a simpler model was obtained where the bais and weights are summarized in Table 21. The correlation coefficient between the fitted and the actual value was 0.9311 and the normalized MSE was 0.05.

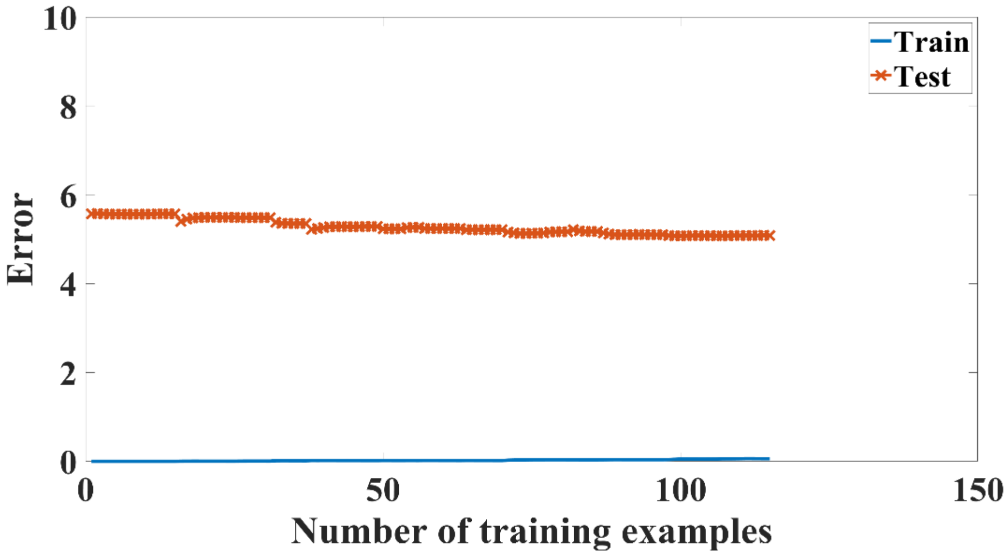

Figure 51: The learning curve of dolomite.

Another simpler model was developed by a fewer predictors

The predicted values of dolomite conductivity were drawn against each other in two different ways shown in Figures 55 and 56. The fitted values at high stresses are less than actual ones as usual.

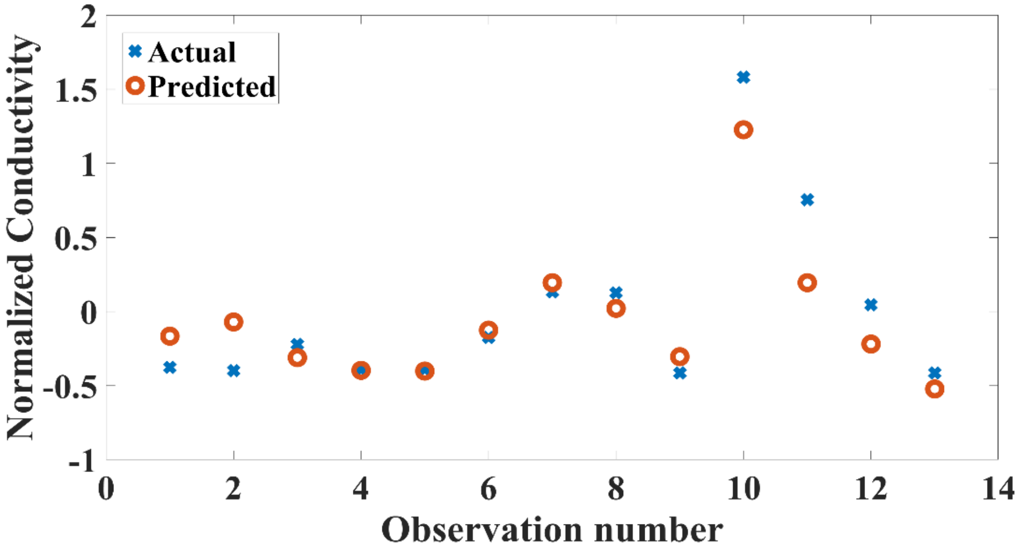

Figure 52: Actual vs predicted of dolomite.

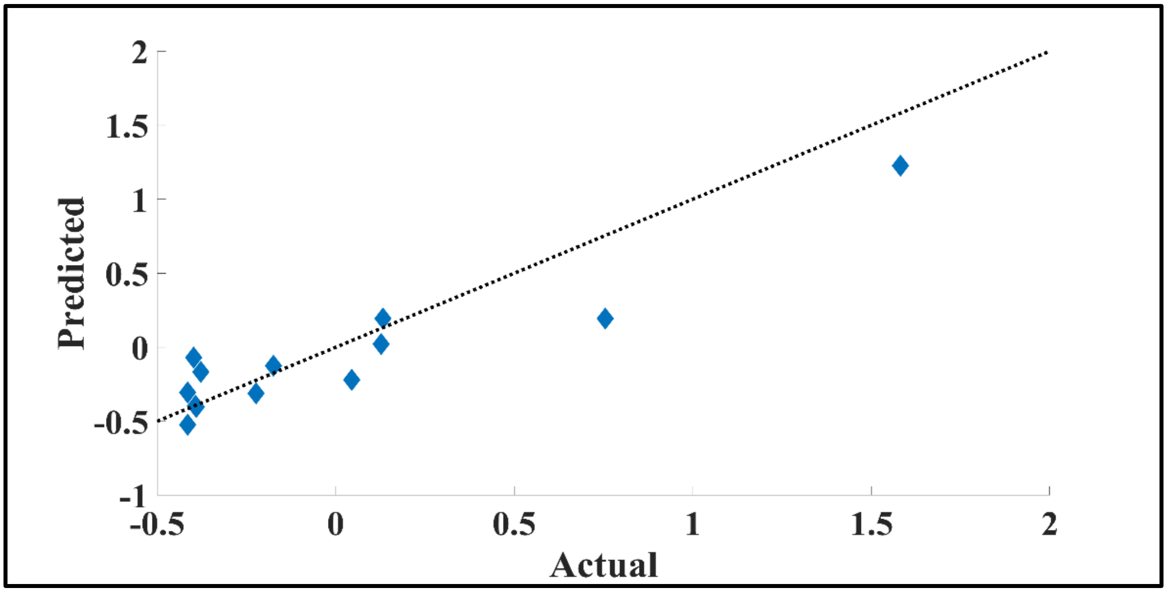

Figure 53: Actual vs predicted on 45-line of dolomite.

The error distribution is slightly asymmetric, and this is obvious in Figure 57.

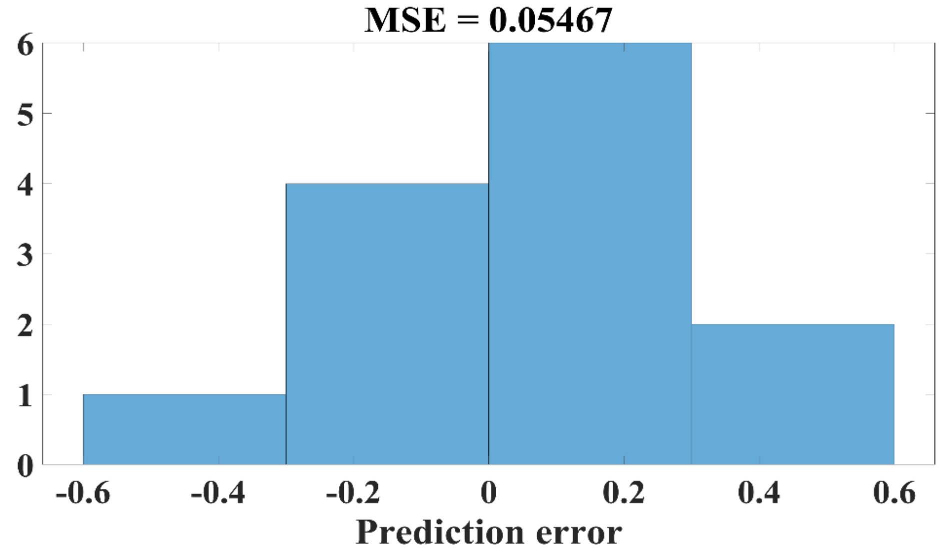

Figure 54: Error distribution of dolomite conductivity predictions.

Table 21: The detailed conductivity model of dolomite.

Bias	0.796903
Stress	0.110252
AcidConcentration	0.561581
InjectionTime	-0.01066
InjectionRate	-0.200212
Stress*AcidConcentration	0.33479
Stress*InjectionTime	-0.032495
Stress*InjectionRate	-0.073771
AcidConcentration*InjectionTime	-0.13047
AcidConcentration*InjectionRate	-0.054778
InjectionTime*InjectionRate	0.014519
Stress^2	-0.168597
AcidConcentration^2	-0.60156
InjectionTime^2	-0.040227
InjectionRate^2	0.030907

5.3.2 Conductivity Prediction of Chalk

Figure 55 shows the minimum number of predictors that are sufficient to get the lowest loss when training a polynomial model to predict conductivity for chalk. Thus, “EtchingPattern=Turbulence”, “Temperature”, “InlectionTime” and “Stress” were selected as predictors. The chalk conductivity model was created by training a polynomial regression model of the selected 4 predictors, their quadratic values and their interactions with each other.

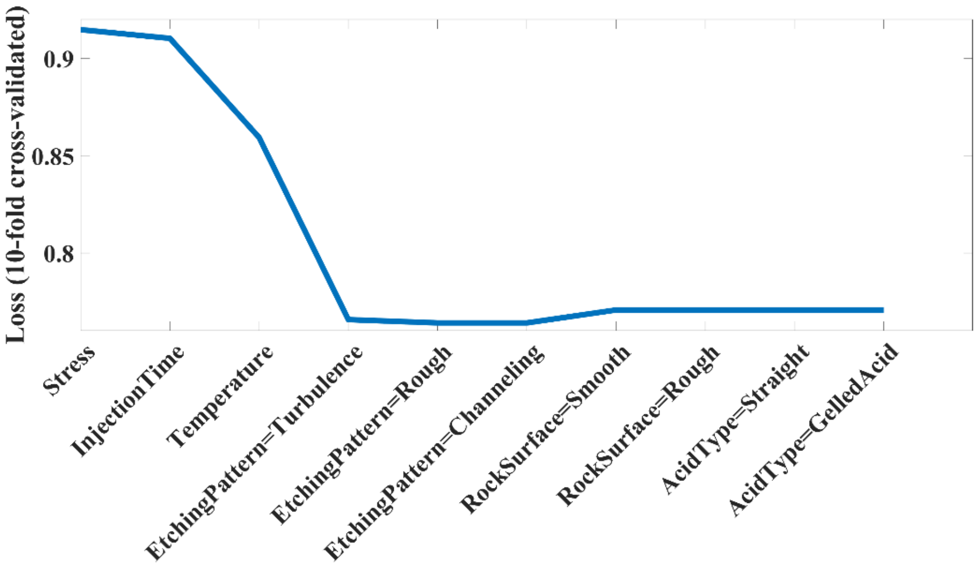

Figure 55: Lowest no. of predictors to get the least loss for chalk.

The Pareto charts of the first 5 principal components explained more than 99% of data variance as shown in Figure 56.

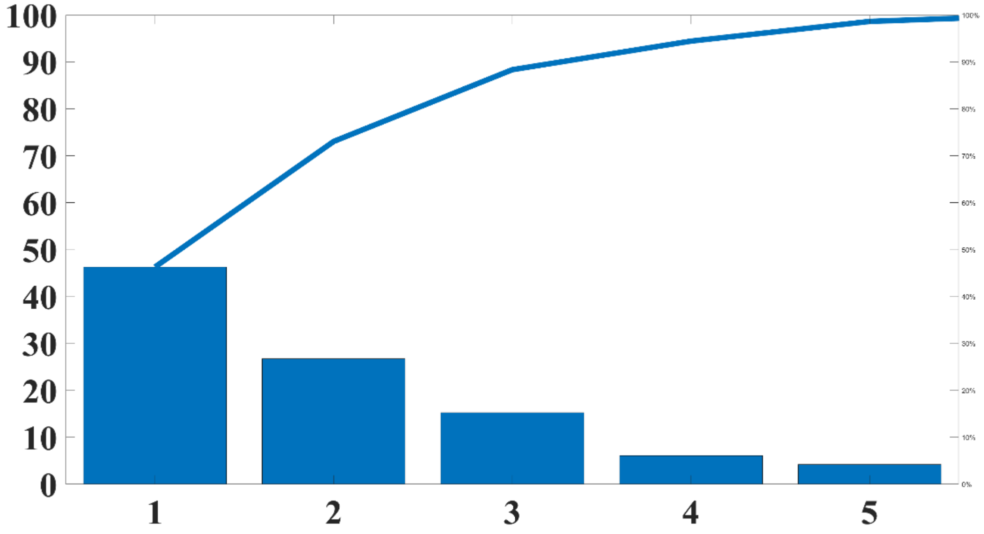

Figure 56: Principle component analysis of chalk predictors.

The learning curve in Figure 57 shows a good fit as the two curves plateau at low error value. The regularization parameter was selected to be 0.001 because the cross-validation error was minimum at this value.

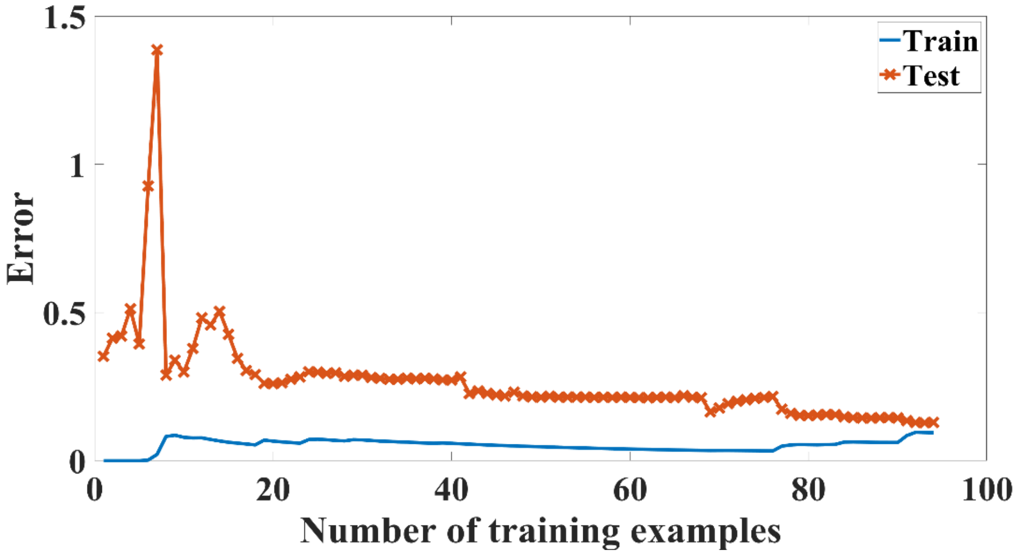

Figure 57: The learning curve of chalk.

The predicted values of chalk conductivity were drawn against each other in two different way shown in Figures 58 and 59. The correlation coefficient between the fitted and the actual value is 0.9056.

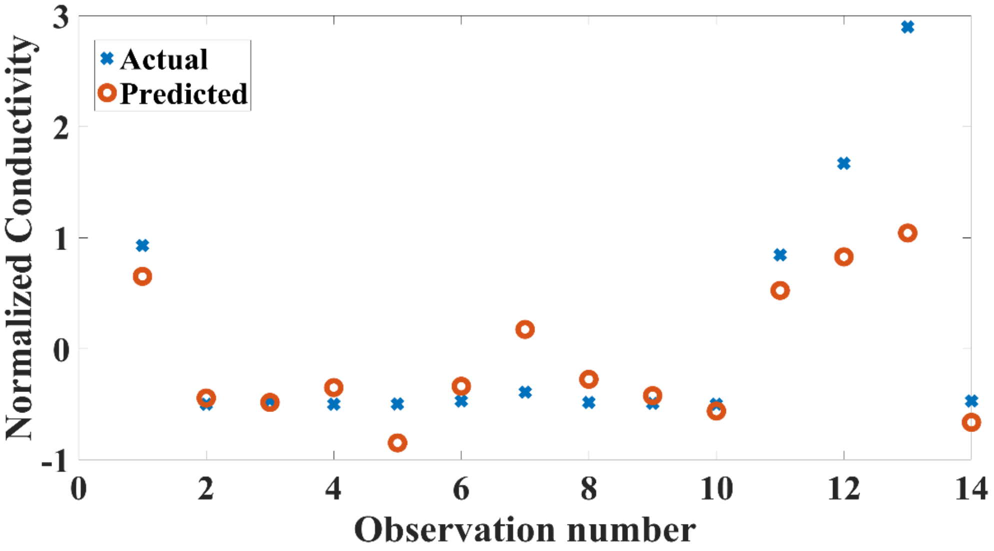

Figure 58: Actual vs predicted of chalk.

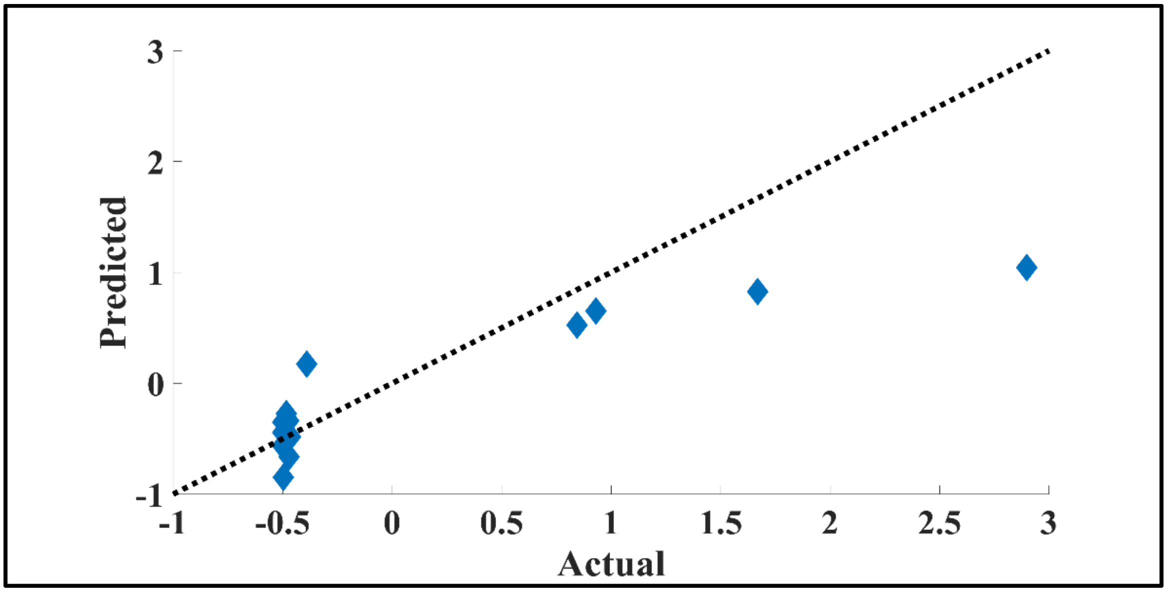

Figure 59: Actual vs Predicted on 45-line of Chalk

The error distribution of chalk conductivity indicates nearly symmetric behaviour as per Figure 61. Most of the errors were between [-1,0] and [0.1] with almost the same frequency.

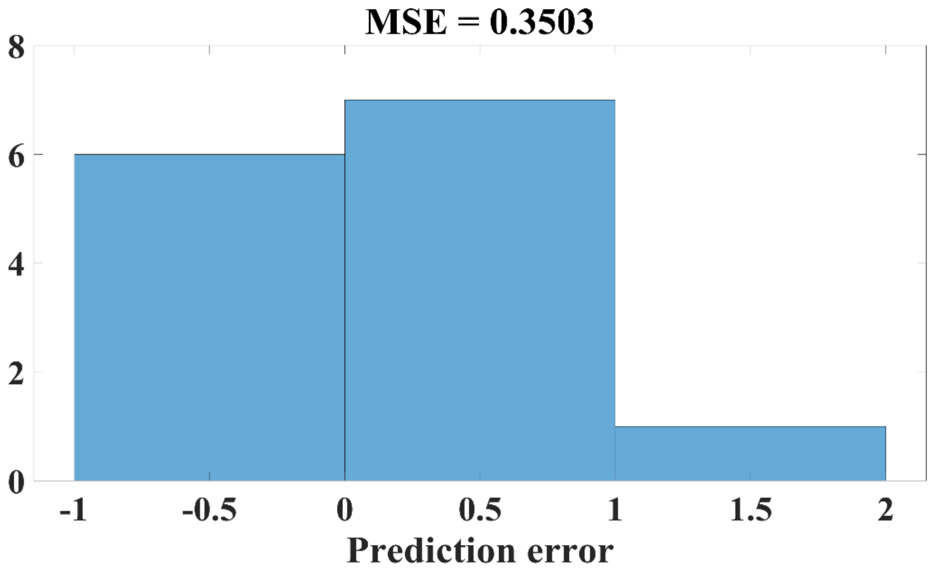

Figure 60: Error distribution of chalk.

For dolomite and chalk, it was possible to train simpler models with fewer predictors. The reason was that they often developed roughness etching pattern (see Table20). Thus, another simpler model for chalk conductivity with the same performance as the previous one is summarized in Table 22.

Table 22: The detailed conductivity model of chalk.

Bias	0.376942
Stress	-0.11794
InjectionTime	0.285134
Temperature	-0.33907
Stress*InjectionTime	-0.0672
Stress*Temperature	-0.08672
InjectionTime*Temperature	0.023183
Stress^2	-0.54759
InjectionTime^2	-0.05668
Temperature^2	0.145894

5.3.3 Conductivity Prediction of Limestone

Predicting limestone conductivity was problematic because it generates all kinds of etching patterns. Thus, for developing a reasonable conductivity model, high conductivity values should be expected first. To do so, a classifier was developed based on the treatment and original surface conditions using ensemble classification. The classifier accuracy reaches 93% (see Figure 61). The output of this classifier will be feed to the polynomial regression model as an additional predictor.

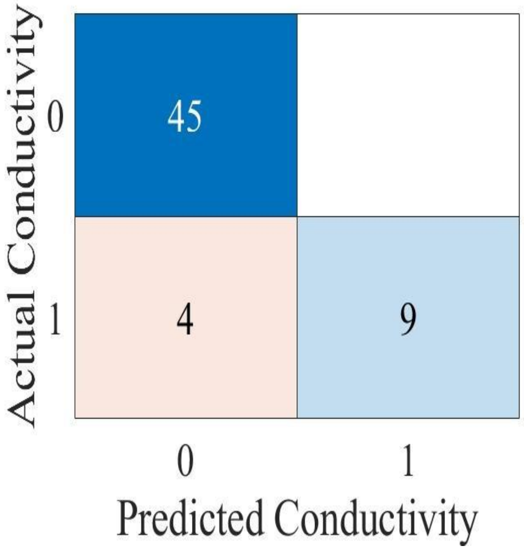

Figure 61: Confusion matrix.

The high conductivity values were labelled as 1 or "Conductivity=High" while the normal ones were labelled 0 or "Conductivity=Normal". The confusion matrix misclassified 4 high conductivity data points of the test data set. Error analysis was performed to investigate why the misclassification occurred. The channels could be considered as open slots and the conductivity of these channels depends on the width of the channel. Some channels were more conductive than the others as they were wider. The V-shape angle of the channel itself impacted the sustainability of the channel under the stress. For instance, if the angel of the V-shape was acute, it would collapse at higher stress than that of the obtuse angle channel.

Figure 62 shows the minimum number of predictors that are sufficient to get the lowest loss when training a polynomial model to predict conductivity for limestone. Thus, starting from predictor "AcidType=Straight" and ending by predictor "Stress" were selected. The loss curve started to increase with increasing the number of predictors because of overfitting the data by the training.

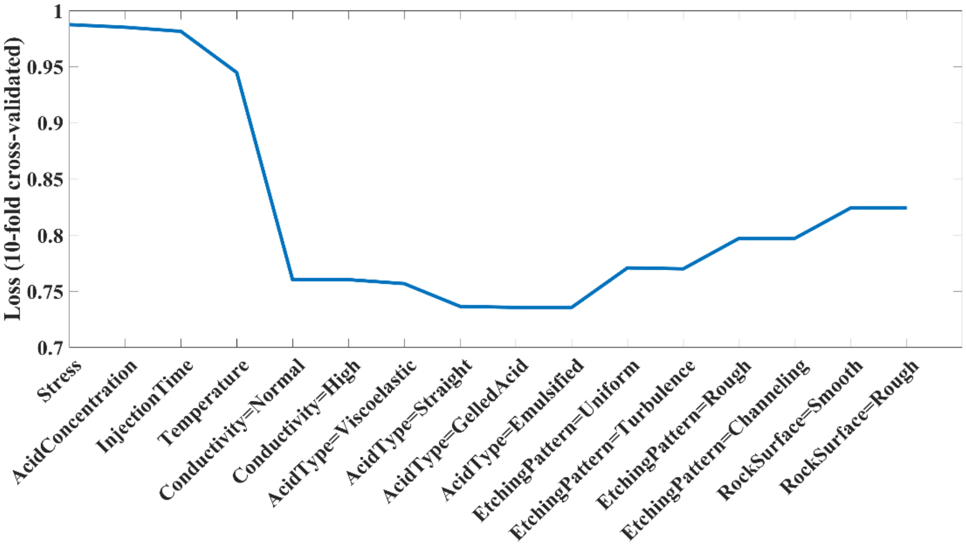

Figure 62: Lowest no. of predictors to get the least loss for limestone.

The principal component analysis of the limestone predictors matrix is shown in Figure 63. The variance was distributed among more principal components, unlike the dolomite and chalk.

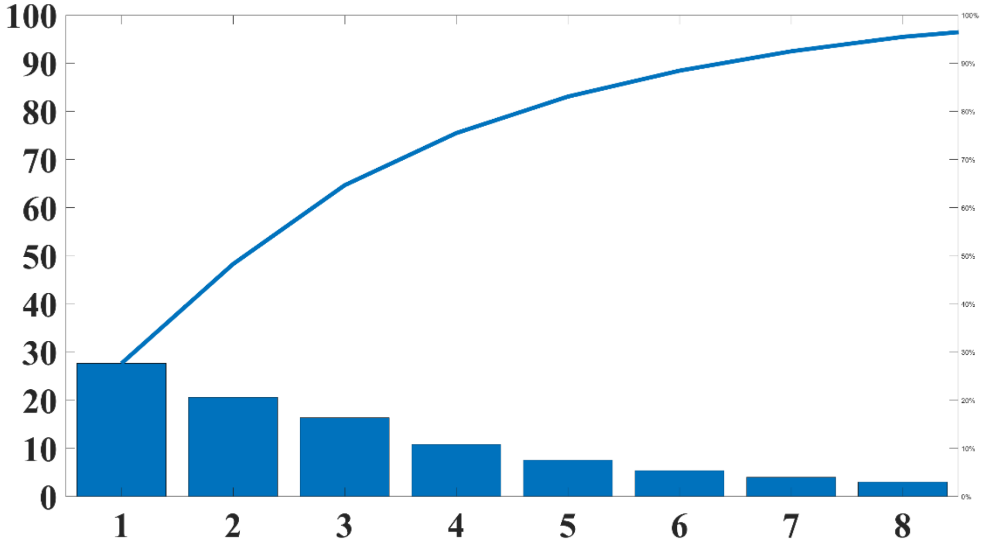

Figure 63: Principle component analysis of limestone predictors.

Several limestone conductivity models were created by training a polynomial regression model with different combinations of predictors. The simplest one was tabulated in Table 23. The learning curve in Figure 63 shows a slight high variance as the training curve plateaus whereas the test error has a higher value. The regularization parameter was selected to be 0.003 because the cross-validation error was minimum at this value.

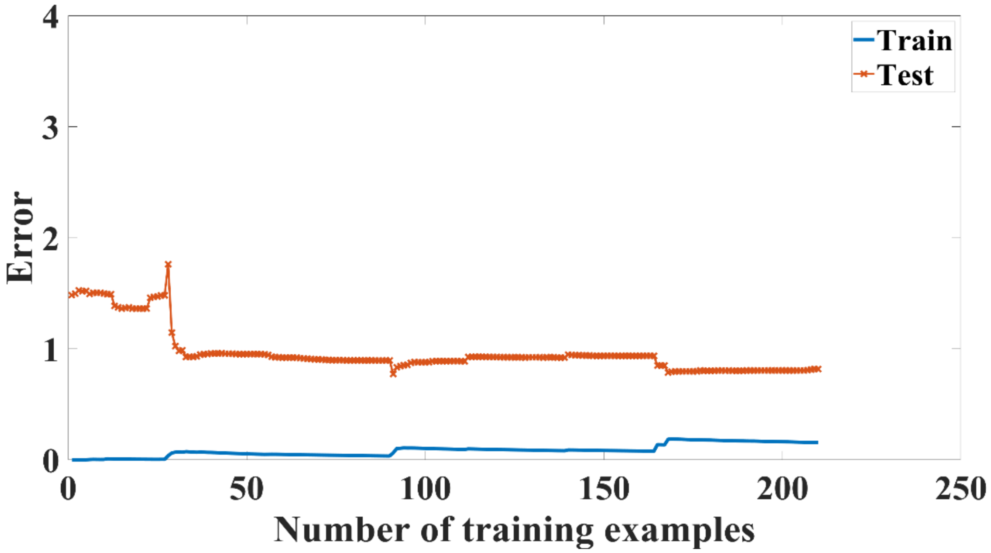

Figure 64: The learning curve of limestone.

The predicted values of chalk conductivity were drawn against each other in two different way in the next two Figures 65 and 66. The correlation coefficient between the fitted and the actual value is 0. 0.9185.

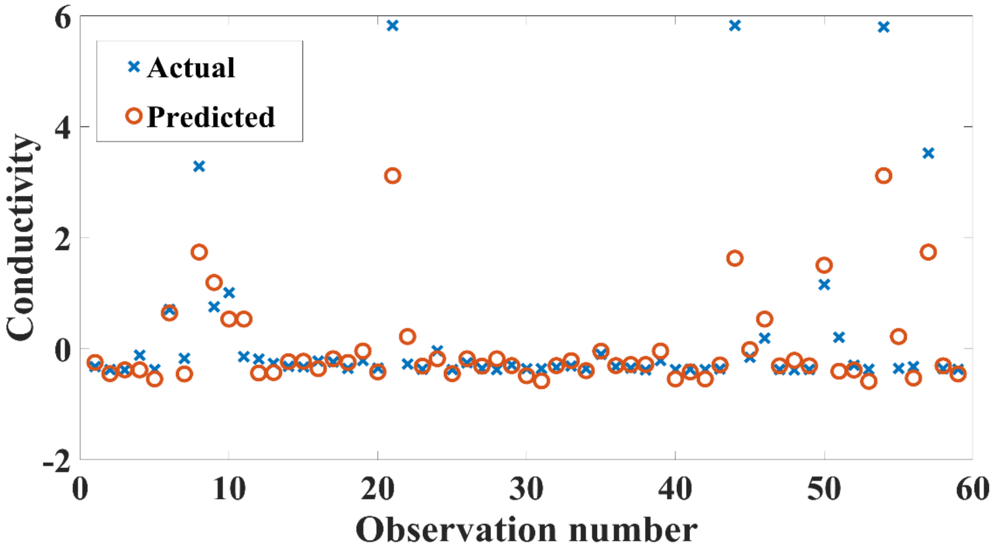

Figure 65: Actual vs predicted of limestone.

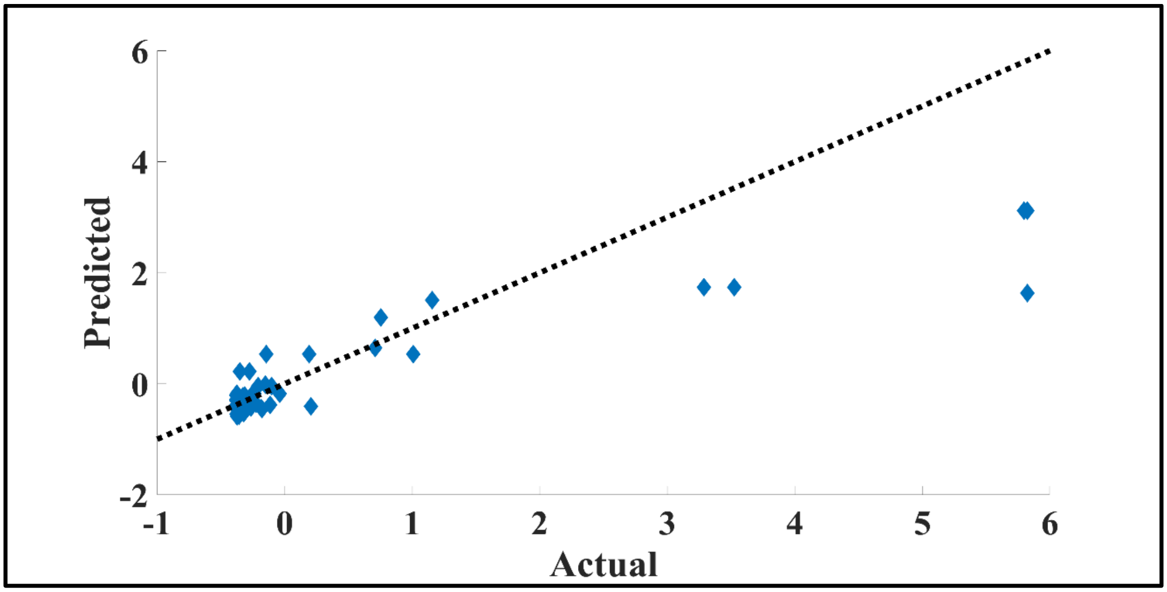

Figure 66: Actual vs Predicted on 45-line of Limestone.

The error distribution of the limestone conductivity was asymmetric as there were high conductivity points that could not be forecasted by the model (Figure 67). These extremely high conductivity values could not be expected by the classifier nor the conductivity model. Their values were 2 to 3 order of magnitude higher than the normal values. The overall error was amplified to 0.686 due to the presence of these points.

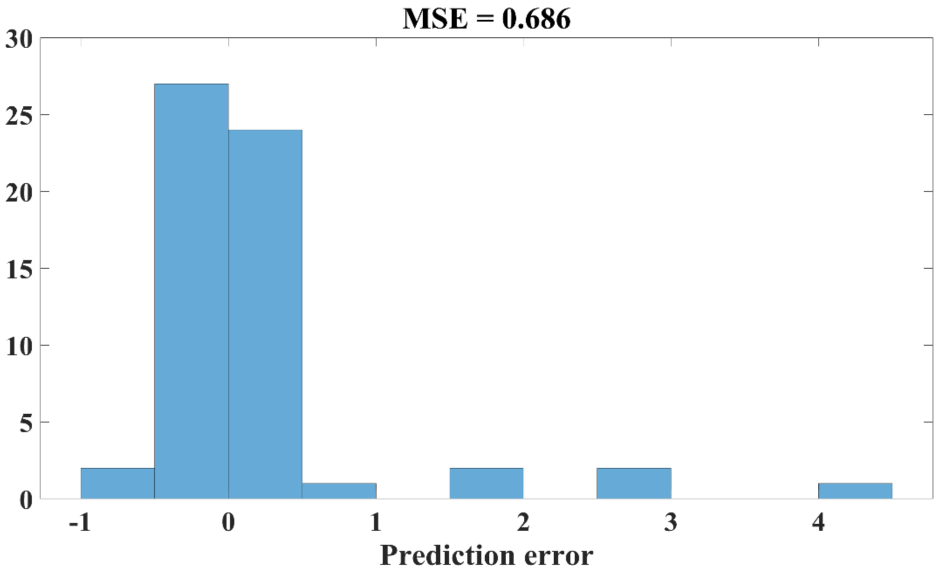

Figure 67: Error distribution of limestone.

Table 23: The detailed conductivity model of limestone.

Bias	0.237377
Conductivity=Normal	-0.545072
Temperature	0.497407
Stress	-0.859811
Conductivity=Normal* Temperature	-0.468028
Conductivity=Normal* Stress	0.724518
Stress*Temperature	-0.131667
AcidType=Viscoelastic	-0.070027
AcidType=Straight	0.110277
Stress^2	-0.000784

CHAPTER 6

CONCLUSIONS AND RECOMMENDATIONS

6.1 Conclusions

The acid fracture was proven in the literature to soften the rock after acid fracturing jobs and remedial actions should be taken to diminish the severity of production decline rate. Novel approaches to restore the rock strength or increase its hardness were experimentally tested. The first approach to increase the rock hardness was conducted by using consolidation agents of nanocrystals and tetraethyl orthosilicate solutions. The calcium hydroxide nanocrystals solution has the potential to elevate the rock strength by 15%, whereas the tetraethyl orthosilicate solution increased the rock strength up to 20% in one of the experiments.

The surface mineral alteration was the second approach to enhance rock surface strength as it is most affected by direct contact with acids. Zinc sulfate solution was employed to change the calcite into smithsonite on the limestone surface. Ideally, smithsonite is 50% harder than calcite. The zinc sulfate solution enhanced the rock hardness by a value of 25% to 35% by forming smithsonite on the sample's surface.

The permeability at least halved in most of the treatment operations except for treatment with tetraethyl orthosilicate solution where it remained at the same level before treatment. The porosity of all samples was kept unaltered with treatment solutions except zinc chloride treatment.

Etching pattern resulted from acid fracturing has a considerable impact on acid fracture conductivity, furthermore, it should be included in acid fracture conductivity estimation. Dolomite and chalk developed roughness etching pattern in more than 85% and 90% of the acid etching experiments. Limestone developed roughness etching pattern in less than 50% and channelling etching pattern in 30% of the acid etching experiments. Limestone extremely high conductivity channels could not be fitted by the model and increased the error. Most of the errors in acid fracture conductivity estimation happen at low stresses when the fracture behaves as an open slot or at high stresses when the rock fails unexpectedly under the closure stress.

6.2 Recommendations and Future Work

Performing confirmatory analyses either destructive or nondestructive to prove the effects of different treatment fluids on rock hardness such as ultrasonic velocity, scratch test, confined compressive strength.

Examining the samples that have been proven to be hardened with the modified API cell to test the effect of hardness increase in the fracture conductivity.

Gathering more conductivity data to test the developed model and address the problem of high variance whenever is found.

Trying different machine learning and artificial intelligence techniques such as neural networks to enhance the etching pattern classification and hydraulic fracture conductivity prediction.

References

Abass, H. H., Al-Mulhem, A. A., Alqam, M. H., & Khan, M. R. (2006, January). Acid fracturing or proppant fracturing in carbonate formation? A rock mechanics view. In *SPE Annual Technical Conference and Exhibition*. Society of Petroleum Engineers.

Aggistalis, G., Alivizatos, A., Stamoulis, D., & Stournaras, G. (1996). Correlating uniaxial compressive strength with Schmidt hardness, point load index, Young's modulus, and mineralogy of gabbros and basalts (Northern Greece). Bulletin of the International Association of Engineering Geology-Bulletin de l'Association Internationale de Géologie de l'Ingénieur, 54(1), 3-11.

Akbari, M., Javad Ameri, M., Kharazmi, S., Motamedi, Y., & Pournik, M. (2017). New correlations to predict fracture conductivity based on the rock strength. *Journal of Petroleum Science and Engineering*, *152*, 416–426.

Al Jawad, M. S. H. (2018). *Development of a Fully Integrated Acid Fracture Model* (Doctoral dissertation).

Almomen, A. M. (2013). *The Effects of Initial Condition of Fracture Surfaces, Acid Spending, and Type on Conductivity of Acid Fracture* (Doctoral dissertation).

Al-Momin, A., Zhu, D., & Hill, A. D. (2014, March). The effects of initial condition of fracture surfaces, acid spending and acid type on conductivity of acid fracture. In *Offshore Technology Conference-Asia*. Offshore Technology Conference.

Al-Mutairi, S. H., Hill, A. D., & Nasr-El-Din, H. A. (2008). Fracture conductivity using emulsified acids: effects of emulsifier concentration and acid volume fraction. *International Petroleum Technology Conference*. International Petroleum Technology Conference.

Anderson, M. S., & Fredrickson, S. E. (1987, January). Dynamic Etching Tests Aid Fracture Acidizing Treatment Design. In *Low Permeability Reservoirs Symposium*. Society of Petroleum Engineers.

Antelo, L. F., Zhu, D., & Hill, A. D. (2009, January). Surface characterization and its effect on fracture conductivity in acid fracturing. In *SPE Hydraulic Fracturing Technology Conference*. Society of Petroleum Engineers.

Asadollahpour, E., Baghbanan, A., Hashemolhosseini, H., & Mohtarami, E. (2018). The etching and hydraulic conductivity of acidized rough fractures. *Journal of Petroleum Science and Engineering*, *166*, 704-717.

Aziz, H. A., Adlan, M. N., & Ariffin, K. S. (2008). Heavy metals (Cd, Pb, Zn, Ni, Cu and Cr (III)) removal from water in Malaysia: post treatment by high quality limestone. *Bioresource technology*, *99*(6), 1578-1583.

Barri, A., Mahmoud, M., & Elkatatny, S. (2016). Evaluation of Rock Mechanical Properties Alteration During Matrix Stimulation With Chelating Agents. *Journal of Energy Resources Technology*, *138*(3), 032907.

Bartko, K. M., Conway, M. W., Krawietz, T. E., Marquez, R. B., & Oba, R. G. M. (1992, January). Field and laboratory experience in closed fracture acidizing the Lisburne field, Prudhoe bay, Alaska. In *SPE Annual Technical Conference and Exhibition*. Society of Petroleum Engineers.

Bartko, K. M., Nasr-El-Din, H. A., Rahim, Z., & Al-Muntasheri, G. A. (2003, January). Acid fracturing of a gas carbonate reservoir: the impact of acid type and lithology on fracture half length and width. In *SPE Annual Technical Conference and Exhibition*. Society of Petroleum Engineers.

Beg, M. S., Kunak, A. O., Gong, M., Zhu, D., & Hill, A. D. (1998). A Systematic Experimental Study of Acid Fracture Conductivity. *SPE Production & Facilities*, *13*(04), 267–271.

Bemer, E., & Lombard, J. M. (2010). From injectivity to integrity studies of CO2 geological storage-chemical alteration effects on carbonates petrophysical and geomechanical properties. *Oil & Gas Science and Technology–Revue de l'Institut Français du Pétrole*, *65*(3), 445-459.

Cash, R. J. (2016). *Acid fracturing carbonate-rich shale: a feasibility investigation of eagle ford formation* (Doctoral dissertation).

Chen, L., Kang, Q., Viswanathan, H. S., & Tao, W. Q. (2014). Pore-scale study of dissolution-induced changes in hydrologic properties of rocks with binary minerals. *Water resources research*, *50*(12), 9343-9365.

Cooke Jr, C. E. (1975). Effect of fracturing fluids on fracture conductivity. *Journal of Petroleum Technology*, *27*(10), 1-273.

Deng, J., Mou, J., Hill, A. D., & Zhu, D. (2012). A New Correlation of Acid-Fracture Conductivity Subject to Closure Stress. *SPE Production & Operations*, *27*(02), 158–169.

Van Domelen, M. S., Gdanski, R. D., & Finley, D. B. (1994, January). The application of core and well testing to fracture acidizing treatment design: a case study. In *European Production Operations Conference and Exhibition*. Society of Petroleum Engineers.

Eissa, E. A., & Kazi, A. (1988). Relation between static and dynamic Young's moduli of rocks. International Journal of Rock Mechanics and Mining & Geomechanics Abstracts, 25(6).

Eliebid, M., Hassan, A. M., Mahmoud, M., Abdulraheem, A., & Elkatatny, S. (2018, August). Intelligent Prediction of Acid-Fracturing Performance in Carbonates Reservoirs. In *SPE Kingdom of Saudi Arabia Annual Technical Symposium and Exhibition*. Society of Petroleum Engineers.

Gangi, A. F. (1978, October). Variation of whole and fractured porous rock permeability with confining pressure. In *International Journal of Rock Mechanics and Mining Sciences & Geomechanics Abstracts* (Vol. 15, No. 5, pp. 249-257). Pergamon.

Garrouch, A. A., & Jennings Jr, A. R. (2017). A contemporary approach to carbonate matrix acidizing. *Journal of Petroleum Science and Engineering*, *158*, 129-143.

Gomaa, A. M., & Nasr-El-Din, H. A. (2009, January). Acid fracturing: the effect of formation strength on fracture conductivity. In *SPE Hydraulic Fracturing Technology Conference*. Society of Petroleum Engineers.

Gong, M. (1997). *Mechanical and hydraulic behavior of acid fractures: experimental studies and mathematical modeling* (Doctoral dissertation, University of Texas at Austin).

Gou, B., Zeng, M., Guo, J., Lai, J., Liu, Z., Ma, H., … Liu, F. (2019, September 3). Effects of Hydrochloric Acid on the Mechanical and Elastic Properties of Tight Dolomite. American Rock Mechanics Association.

Graziani, G., Sassoni, E., & Franzoni, E. (2015). Consolidation of porous carbonate stones by an innovative phosphate treatment: mechanical strengthening and physical-microstructural compatibility in comparison with TEOS-based treatments. *Heritage Science*, *3*(1), 1.

Hill, A. D., Pournik, M., Zou, C., Malagon Nieto, C., Melendez, M. G., Zhu, D., & Weng, X. (2007, January). Small-scale fracture conductivity created by modern acid fracture fluids. In *SPE Hydraulic Fracturing Technology Conference*. Society of Petroleum Engineers.

Jafarpour, H., Moghadasi, J., Khormali, A., Petrakov, D.G., Ashena, R., 2019. Increasing the stimulation efficiency of heterogeneous carbonate reservoirs by developing a multi-bached acid system. J. Pet. Sci. Eng. 172, 50–59.

Jeon, J., Bashir, M. O., Liu, J., & Wu, X. (2016, August). Fracturing Carbonate Reservoirs: Acidising Fracturing or Fracturing with Proppants?. In *SPE Asia Pacific Hydraulic Fracturing Conference*. Society of Petroleum Engineers.

Joel, E. O., & Pournik, M. (2011, January). Does Rock Really Weaken During Acid Fracturing Operations?. In *SPE Production and Operations Symposium*. Society of Petroleum Engineers.

Kang, Q., Chen, L., Valocchi, A.J., Viswanathan, H.S., 2014. Pore-scale study of dissolution-induced changes in permeability and porosity of porous media. J. Hydrol. 517, 1049–1055.

Kamali, A., & Pournik, M. (2015, January). Rough Surface Closure–A Closer Look at Fracture Closure and Conductivity Decline. In *ISRM Regional Symposium-EUROCK 2015*. International Society for Rock Mechanics and Rock Engineering.

Kamali, A., & Pournik, M. (2016). Fracture closure and conductivity decline modeling – Application in unpropped and acid etched fractures. *Journal of Unconventional Oil and Gas Resources, 14*, 44–55.

Karadkar, P., Suzart, W., Sabhapondit, A., Buenrostro, A., & Jauregui, J. L. (2016, November). Novel High Viscus Acid System for Proppant Fracture Acidizing. In *Abu Dhabi International Petroleum Exhibition & Conference*. Society of Petroleum Engineers.

Kazakov, N., & Miskimins, J. L. (2011, January). Application of multivariate statistical analysis to slickwater fracturing parameters in unconventional reservoir systems. In *SPE Hydraulic Fracturing Technology Conference*. Society of Petroleum Engineers.

Li, Y., & Han, Y. (2017, November). Decline Curve Analysis for Production Forecasting Based on Machine Learning. In *SPE Symposium: Production Enhancement and Cost Optimisation*. Society of Petroleum Engineers.

Liu, M., Mostaghimi, P., 2017. Pore-scale simulation of dissolution-induced variations in rock mechanical properties. Int. J. Heat Mass Transf. 111, 842–851.

López-Arce, P., Gomez-Villalba, L. S., Pinho, L., Fernández-Valle, M. E., de Buergo, M. Á., & Fort, R. (2010). Influence of porosity and relative humidity on consolidation of dolostone with calcium hydroxide nanoparticles: effectiveness assessment with non-destructive techniques. *Materials Characterization, 61*(2), 168-184.

López-Arce, P., Gómez-Villalba, L. S., Martínez-Ramírez, S., De Buergo, M. Á., & Fort, R. (2011). Influence of relative humidity on the carbonation of calcium hydroxide nanoparticles and the formation of calcium carbonate polymorphs. *Powder technology*, *205*(1-3), 263-269.

Lu, C., Bai, X., Luo, Y., & Guo, J. (2017). New study of etching patterns of acid-fracture surfaces and relevant conductivity. *Journal of Petroleum Science and Engineering*, *159*, 135–147.

McDuff, D., Malhotra, S., Comeaux, B. A., & Quintero, B. W. (2018, September). Observations and Complexities in Experimental Measurement of Acid Fracture Conductivity for a Deep Carbonate Field in Kazakhstan. In *SPE Annual Technical Conference and Exhibition*. Society of Petroleum Engineers.

Melendez Castillo, M. G. (2009). *The effects of acid contact time and rock surfaces on acid fracture conductivity* (Doctoral dissertation).

Melendez, M. G., Pournik, M., Zhu, D., & Hill, A. D. (2007, January). The effects of acid contact time and the resulting weakening of the rock surfaces on acid fracture conductivity. In *European Formation Damage Conference*. Society of Petroleum Engineers.

Morsy. S, Hetherington. C J, Sheng. J J et al. 2015. Effect of Low-concentration HCl on The Mineralogy, Physical and Mechanical Properties, and Recovery Factors of Some Shales. Journal of Unconventional Oil & Gas Resources, 9: 94-102.

Motamedi-Ghahfarokhi, Y., Ameri Shahrabi, M. J., Akbari, M., & Pournik, M. (2018). New correlations to predict fracture conductivity based on the formation lithology. *Energy Sources, Part A: Recovery, Utilization, and Environmental Effects*, *40*(13), 1663-1673.

Nasr-El-Din, H. A., Al-Driweesh, S. M., Chesson, J. B., & Metcalf, A. S. (2006, January). Fracture acidizing: what role does formation softening play in production response?. In *SPE Annual Technical Conference and Exhibition*. Society of Petroleum Engineers.

Navarrete, R. C., Miller, M. J., & Gordon, J. E. (1998, January). Laboratory and theoretical studies for acid fracture stimulation optimization. In *SPE Permian Basin Oil and Gas Recovery Conference*. Society of Petroleum Engineers.

Nierode, D. E., & Kruk, K. F. (1973, January). An evaluation of acid fluid loss additives retarded acids, and acidized fracture conductivity. In *Fall Meeting of the Society of Petroleum Engineers of AIME*. Society of Petroleum Engineers.

Nieto, C. M., Pournik, M., & Hill, A. D. (2008). The texture of acidized fracture surfaces: implications for acid fracture conductivity. *SPE Production & Operations*, *23*(03), 343-352.

Ng, A. (2011). Advice for applying machine learning. In *Machine learning*.

Ossola, F., Tomasin, P., De Zorzi, C., El Habra, N., Chiurato, M., & Favaro, M. (2012). New calcium alkoxides for consolidation of carbonate rocks. Influence of precursors' characteristics on morphology, crystalline phase and consolidation effects. *New Journal of Chemistry*, *36*(12), 2618-2624.

Pinto, A. P. F., & Rodrigues, J. D. (2012). Consolidation of carbonate stones: Influence of treatment procedures on the strengthening action of consolidants. *Journal of Cultural Heritage*, *13*(2), 154-166.

Pournik, M. (2008). *Laboratory-scale fracture conductivity created by acid etching*. Texas A&M University.

Pournik, M., Zhu, D., & Hill, A. D. (2009, January). Acid-fracture conductivity correlation development based on acid-etched fracture characterization. In *8th European Formation Damage Conference*. Society of Petroleum Engineers.

Pournik, M., Gomaa, A. M., & Nasr-El-Din, H. A. (2010, January). Influence of acid-fracture fluid properties on acid-etched surfaces and resulting fracture conductivity. In *SPE International Symposium and Exhibition on Formation Damage Control*. Society of Petroleum Engineers.

Pournik, M., Li, L., Smith, B. T., & Nasr-El-Din, H. A. (2013). Effect of acid spending on etching and acid-fracture conductivity. *SPE Production & Operations*, *28*(01), 46-54.

Railsback, L. B. (1999). Patterns in the compositions, properties, and geochemistry of carbonate minerals. *Carbonates and Evaporites*, *14*(1), 1.

Ruffet, C., Fery, J. J., & Onaisi, A. (1998). Acid Fracturing Treatment: a Surface Topography Analysis of Acid Etched Fractures to Determine Residual Conductivity. *SPE Journal*, *3*(02), 155–162.

Saleh, L. D., Wei, M., & Bai, B. (2014). Data analysis and updated screening criteria for polymer flooding based on oilfield data. *SPE Reservoir Evaluation & Engineering*, *17*(01), 15-25.

Smith, M. B., Deng, J. Y., Sajid, B., Mokhtar, A. A. Y., & Taramov, M. (2018, October). Simulation, Design and Application of Acid+ Proppant Stimulation in a Carbonate

Reservoir. In *SPE International Hydraulic Fracturing Technology Conference and Exhibition*. Society of Petroleum Engineers.

Suleimenova, A., Wang, X., Zhu, D., & Hill, A. D. (2016, May). Comparative study of acid fracturing and propped hydraulic fracturing for a tight carbonate formation. In *SPE Europec featured at 78th EAGE Conference and Exhibition*. Society of Petroleum Engineers.

Teklu, T. W., Abass, H. H., Hanashmooni, R., Carratu, J. C., & Ermila, M. (2017). Experimental investigation of acid imbibition on matrix and fractured carbonate rich shales. *Journal of Natural Gas Science and Engineering*, *45*, 706-725.

Walsh, J. B. (1981, October). Effect of pore pressure and confining pressure on fracture permeability. In *International Journal of Rock Mechanics and Mining Sciences & Geomechanics Abstracts* (Vol. 18, No. 5, pp. 429-435). Pergamon.

Williams, B. B., Gidley, J. L., & Schechter, R. S. (1979). Acidizing Fundamentals, Henry L. *Doherty Memorial Fund of AIME, Society of Petroleum Engineers of AIME, New York*.

Zhang, H., Zhong, Y., Zhang, J., Zhang, Y., Kuang, J., & Yang, B. (2019). Experimental research on deterioration of mechanical properties of carbonate rocks under acidified conditions. *Journal of Petroleum Science and Engineering*, 106612.

Zhang, L., Zhou, F., Mou, J., Xu, G., Zhang, S., & Li, Z. (2018). A new method to improve long-term fracture conductivity in acid fracturing under high closure stress. *Journal of Petroleum Science and Engineering*, *171*, 760–770.

Zhizhaev, A. M., & Merkulova, E. N. (2008). Interaction of sulfate solutions of zinc with natural calcium carbonates. *Russian Journal of Applied Chemistry*, *81*(6), 946-951.

Zhizhaev, A. M., & Merkulova, E. N. (2014). Interaction of copper (II) and zinc (II) in coprecipitation from sulfate solutions with natural calcium carbonate. *Russian Journal of Applied Chemistry*, *87*(1), 16-22.

Zhong, Y., Kuru, E., Zhang, H., Kuang, J., & She, J. (2019). Effect of fracturing fluid/shale rock interaction on the rock physical and mechanical properties, the proppant embedment depth and the fracture conductivity. *Rock Mechanics and Rock Engineering*, *52*(4), 1011-1022.

APPENDIX A

PMI Gas Permeameter Calculations

Modification of Darcy's Equation for compressible fluids to measure the permeability:

$$K_n = \frac{2 \times 10^3 \times Q_n \times \mu_n \times L \times P_m}{A \times (P_1^2 - P_2^2)}$$

Where:

K_n = Nitrogen permeability, md.

Q_n = Nitrogen flow rate, cc/sec.

μ_n = Nitrogen viscosity, cp.

A = Plug cross-sectional area, sq.cm.

L = Length, cm.

P_m = Mean pressure, atm.

P_1 = Upstream pressures, atm.

P_2 = downstream pressure, atm.

Klinkenberg Effect Verification

Many gas permeability values, at different pressures, are plotted against one over the mean pressure ($1/P_m$). The intercept of the best fitted straight line resulted with the gas permeability axis at zero ($1/P_m$) is equal to the liquid state permeability of gas as this represents that the gas is pressurized to a liquid phase.

Klinkenberg used the following relationship to determine the slip effect of gases and the liquid permeability:

$$K_l = \frac{K_g}{1 + b/P_m}$$

Where:

K_l = Non-reactive liquid permeability

K_g = Gas permeability

P_m = Mean pressure

b = Klinkenberg constant for a given gas in a given porous media.

Rearranging Klinkenberg relationship as:

$$K_g = K_l + K_l \times b/P_m$$

K_l = The intercept of the line with gas permeability axis.

$K_l \times b$ = The slope of the resulted straight line.

APPENDIX B

TPI-219 helium porosimeter Calculations

The system reference volume is calculated by the following Equation:

$$V_{REF} = \frac{V_{REMBIL}}{\left(\frac{P_{REFREM}}{P_{CUPREM}}\right) - \left(\frac{P_{REFFULL}}{P_{CUPFULL}}\right)}$$

Where:

V_{REF} = System reference volume, cm^3.

V_{REMBIL} = Volume of the removed billets, cm^3.

$P_{REFFULL}$ = Full cup reference pressure, psi.

$P_{CUPFULL}$ = Full cup pressure, psi.

P_{REFREM} = Removed billet reference pressure, psi.

P_{CUPREM} = Removed billet cup pressure, psi.

Grain Volume:

Grain volume can be determined from the following formula:

$$V_g = V_{REMBIL} - \left|\left[\left(\frac{P_{REFFULL}}{P_{CUPFULL}}\right)\left(\frac{P_{REFSAMPLE}}{P_{CUPSAMPLE}}\right)\right] \times V_{REF}\right|$$

Where:

V_g = Grain Volume, cm^3.

V_{REMBIL} = Volume of the removed billets, cm^3.

$P_{REFFULL}$ = Full cup reference pressure, psi.

$P_{CUPFULL}$ = Full cup pressure, psi.

$P_{REFSAMPLE}$ = Sample reference pressure, psi.

$P_{CUPSAMPLE}$ = Sample cup pressure, psi.

V_{REF} = System reference volume, cm^3.

APPENDIX C

The gathered data from acid fracture conductivity experiments.

X^1	X^2	X^3	X^4	X^5	X^6	X^7	X^8	X^9	Y
Chalk	GelledAcid	Rough	Channeling	175	1	20	15	100	2252
Chalk	GelledAcid	Rough	Channeling	175	1	20	15	1000	21
Chalk	GelledAcid	Rough	Channeling	175	1	30	15	100	3243
Chalk	GelledAcid	Rough	Channeling	175	1	30	15	1000	2878
Chalk	GelledAcid	Rough	Channeling	175	1	30	15	2000	2615
Chalk	GelledAcid	Rough	Channeling	175	1	30	15	3000	90
Chalk	GelledAcid	Rough	Rough	175	1	20	15	100	4650
Chalk	GelledAcid	Rough	Rough	175	1	20	15	1000	4600
Chalk	GelledAcid	Rough	Rough	175	1	20	15	2000	3470
Chalk	GelledAcid	Rough	Rough	175	1	20	15	3000	34
Chalk	GelledAcid	Rough	Rough	175	1	30	15	100	2682
Chalk	GelledAcid	Rough	Rough	175	1	30	15	1000	1506
Chalk	GelledAcid	Rough	Rough	175	1	30	15	2000	38
Chalk	GelledAcid	Rough	Rough	175	1	30	15	3000	19
Chalk	GelledAcid	Rough	Rough	175	1	30	15	4000	22
Chalk	GelledAcid	Rough	Rough	175	1	10	15	100	572
Chalk	GelledAcid	Rough	Rough	175	1	10	15	1000	201
Chalk	GelledAcid	Rough	Rough	175	1	10	15	2000	83
Chalk	GelledAcid	Rough	Rough	175	1	10	15	3000	21
Chalk	GelledAcid	Smooth	Rough	175	1	5	15	100	2388
Chalk	GelledAcid	Smooth	Rough	175	1	5	15	1000	182
Chalk	GelledAcid	Smooth	Rough	175	1	5	15	2000	84
Chalk	GelledAcid	Smooth	Rough	175	1	5	15	3000	65
Chalk	GelledAcid	Smooth	Rough	175	1	5	15	4000	25
Chalk	GelledAcid	Smooth	Rough	175	1	10	15	100	5000
Chalk	GelledAcid	Smooth	Rough	175	1	10	15	1000	3053
Chalk	GelledAcid	Smooth	Rough	175	1	10	15	2000	149
Chalk	GelledAcid	Smooth	Rough	175	1	10	15	3000	21
Chalk	GelledAcid	Smooth	Rough	175	1	15	15	100	2532
Chalk	GelledAcid	Smooth	Rough	175	1	15	15	1000	47
Chalk	GelledAcid	Smooth	Rough	175	1	15	15	2000	34
Chalk	GelledAcid	Smooth	Rough	175	1	15	15	3000	28
Chalk	GelledAcid	Smooth	Rough	175	1	15	15	4000	22
Chalk	GelledAcid	Smooth	Rough	175	1	20	15	100	2335

Chalk	GelledAcid	Smooth	Rough	175	1	20	15	1000	1472
Chalk	GelledAcid	Smooth	Rough	175	1	20	15	2000	38
Chalk	GelledAcid	Smooth	Rough	175	1	20	15	3000	19
Chalk	GelledAcid	Smooth	Rough	175	1	30	15	100	3661
Chalk	GelledAcid	Smooth	Rough	175	1	30	15	1000	2878
Chalk	GelledAcid	Smooth	Rough	175	1	30	15	2000	2615
Chalk	GelledAcid	Smooth	Rough	175	1	30	15	3000	91
Chalk	GelledAcid	Smooth	Rough	100	1	5	15	0	263
Chalk	GelledAcid	Smooth	Rough	100	1	5	15	500	82
Chalk	GelledAcid	Smooth	Rough	100	1	5	15	1000	63
Chalk	GelledAcid	Smooth	Rough	100	1	5	15	1500	58
Chalk	GelledAcid	Smooth	Rough	100	1	5	15	2000	50
Chalk	GelledAcid	Smooth	Rough	100	1	5	15	2500	41
Chalk	GelledAcid	Smooth	Rough	100	1	5	15	3000	19
Chalk	GelledAcid	Smooth	Rough	100	1	5	15	3500	2
Chalk	GelledAcid	Smooth	Rough	100	1	10	15	0	255
Chalk	GelledAcid	Smooth	Rough	100	1	10	15	500	95
Chalk	GelledAcid	Smooth	Rough	100	1	10	15	1000	72
Chalk	GelledAcid	Smooth	Rough	100	1	10	15	1500	32
Chalk	GelledAcid	Smooth	Rough	100	1	10	15	2000	24
Chalk	GelledAcid	Smooth	Rough	100	1	10	15	2500	20
Chalk	GelledAcid	Smooth	Rough	100	1	10	15	3000	18
Chalk	GelledAcid	Smooth	Rough	100	1	10	15	3500	12
Chalk	GelledAcid	Smooth	Rough	100	1	10	15	4000	4
Chalk	GelledAcid	Smooth	Rough	100	1	5	15	0	413
Chalk	GelledAcid	Smooth	Rough	100	1	5	15	500	124
Chalk	GelledAcid	Smooth	Rough	100	1	5	15	1000	97
Chalk	GelledAcid	Smooth	Rough	100	1	5	15	1500	77
Chalk	GelledAcid	Smooth	Rough	100	1	5	15	2000	63
Chalk	GelledAcid	Smooth	Rough	100	1	5	15	2500	42
Chalk	GelledAcid	Smooth	Rough	100	1	5	15	3000	18
Chalk	GelledAcid	Smooth	Rough	100	1	5	15	3500	4
Chalk	GelledAcid	Smooth	Rough	100	1	10	15	0	386
Chalk	GelledAcid	Smooth	Rough	100	1	10	15	500	120
Chalk	GelledAcid	Smooth	Rough	100	1	10	15	1000	88
Chalk	GelledAcid	Smooth	Rough	100	1	10	15	1500	60
Chalk	GelledAcid	Smooth	Rough	100	1	10	15	2000	43
Chalk	GelledAcid	Smooth	Rough	100	1	10	15	2500	30
Chalk	GelledAcid	Smooth	Rough	100	1	10	15	3000	14

Chalk	GelledAcid	Smooth	Rough	100	1	10	15	3500	5
Chalk	GelledAcid	Smooth	Rough	130	1	5	15	0	3216
Chalk	GelledAcid	Smooth	Rough	130	1	5	15	500	1430
Chalk	GelledAcid	Smooth	Rough	130	1	5	15	1000	692
Chalk	GelledAcid	Smooth	Rough	130	1	5	15	1500	523
Chalk	GelledAcid	Smooth	Rough	130	1	5	15	2000	374
Chalk	GelledAcid	Smooth	Rough	130	1	5	15	2500	106
Chalk	GelledAcid	Smooth	Rough	130	1	5	15	3000	22
Chalk	GelledAcid	Smooth	Rough	130	1	5	15	3500	7
Chalk	GelledAcid	Smooth	Rough	130	1	10	15	0	7647
Chalk	GelledAcid	Smooth	Rough	130	1	10	15	500	5468
Chalk	GelledAcid	Smooth	Rough	130	1	10	15	1000	4373
Chalk	GelledAcid	Smooth	Rough	130	1	10	15	1500	2719
Chalk	GelledAcid	Smooth	Rough	130	1	10	15	2000	1352
Chalk	GelledAcid	Smooth	Rough	130	1	10	15	2500	213
Chalk	GelledAcid	Smooth	Rough	130	1	10	15	3000	72
Chalk	GelledAcid	Smooth	Rough	130	1	10	15	3500	13
Chalk	GelledAcid	Smooth	Rough	130	1	5	15	0	7032
Chalk	GelledAcid	Smooth	Rough	130	1	5	15	500	4373
Chalk	GelledAcid	Smooth	Rough	130	1	5	15	1000	2876
Chalk	GelledAcid	Smooth	Rough	130	1	5	15	1500	1788
Chalk	GelledAcid	Smooth	Rough	130	1	5	15	2000	841
Chalk	GelledAcid	Smooth	Rough	130	1	5	15	2500	186
Chalk	GelledAcid	Smooth	Rough	130	1	5	15	3000	31
Chalk	GelledAcid	Smooth	Rough	130	1	5	15	3500	4
Chalk	GelledAcid	Smooth	Rough	130	1	10	15	0	10997
Chalk	GelledAcid	Smooth	Rough	130	1	10	15	500	8794
Chalk	GelledAcid	Smooth	Rough	130	1	10	15	1000	7436
Chalk	GelledAcid	Smooth	Rough	130	1	10	15	1500	3497
Chalk	GelledAcid	Smooth	Rough	130	1	10	15	2000	1352
Chalk	GelledAcid	Smooth	Rough	130	1	10	15	2500	275
Chalk	GelledAcid	Smooth	Rough	130	1	10	15	3000	72
Chalk	GelledAcid	Smooth	Rough	130	1	10	15	3500	13
Chalk	Straight	Smooth	Turbulence	175	1	5	15	100	2778
Chalk	Straight	Smooth	Turbulence	175	1	5	15	1000	1873
Chalk	Straight	Smooth	Turbulence	175	1	5	15	2000	127
Chalk	Straight	Smooth	Turbulence	175	1	5	15	3000	53
Chalk	Straight	Smooth	Turbulence	175	1	10	15	1000	20444
Chalk	Straight	Smooth	Turbulence	175	1	10	15	2000	700

Chalk	Straight	Smooth	Turbulence	175	1	10	15	3000	24
Chalk	Straight	Smooth	Turbulence	175	1	15	15	100	14801
Chalk	Straight	Smooth	Turbulence	175	1	15	15	1000	14784
Chalk	Straight	Smooth	Turbulence	175	1	15	15	2000	700
Chalk	Straight	Smooth	Turbulence	175	1	15	15	3000	6
Dolomite	Viscoelastic	Smooth	Channeling	200	1	10	15	1000	276
Dolomite	Viscoelastic	Smooth	Channeling	200	1	10	15	2000	176
Dolomite	Viscoelastic	Smooth	Channeling	200	1	10	15	3000	140
Dolomite	Viscoelastic	Smooth	Channeling	200	1	10	15	4000	87
Dolomite	Viscoelastic	Smooth	Channeling	200	1	10	15	5000	73
Dolomite	GelledAcid	Smooth	Rough	130	0.5	20	15	500	127
Dolomite	GelledAcid	Smooth	Rough	130	0.5	20	15	1000	104
Dolomite	GelledAcid	Smooth	Rough	130	0.5	20	15	1500	94
Dolomite	GelledAcid	Smooth	Rough	130	0.5	20	15	2000	92
Dolomite	GelledAcid	Smooth	Rough	130	0.5	20	15	2500	76
Dolomite	GelledAcid	Smooth	Rough	130	0.5	20	15	3000	74
Dolomite	GelledAcid	Smooth	Rough	130	0.5	20	15	3500	57
Dolomite	GelledAcid	Smooth	Rough	130	0.5	20	15	4000	54
Dolomite	GelledAcid	Smooth	Rough	130	0.5	20	15	4500	51
Dolomite	GelledAcid	Smooth	Rough	130	0.5	20	15	5000	40
Dolomite	GelledAcid	Smooth	Rough	130	0.5	20	15	6000	30
Dolomite	GelledAcid	Smooth	Rough	130	0.5	20	15	7000	26
Dolomite	GelledAcid	Smooth	Rough	130	1	10	15	0	1117
Dolomite	GelledAcid	Smooth	Rough	130	1	10	15	1000	150
Dolomite	GelledAcid	Smooth	Rough	130	1	10	15	1500	132
Dolomite	GelledAcid	Smooth	Rough	130	1	10	15	2000	100
Dolomite	GelledAcid	Smooth	Rough	130	1	10	15	2500	87
Dolomite	GelledAcid	Smooth	Rough	130	1	10	15	3000	77
Dolomite	GelledAcid	Smooth	Rough	130	1	10	15	3500	71
Dolomite	GelledAcid	Smooth	Rough	130	1	10	15	4000	65
Dolomite	GelledAcid	Smooth	Rough	130	1	10	15	5000	58
Dolomite	GelledAcid	Smooth	Rough	130	1	10	15	6000	51
Dolomite	GelledAcid	Smooth	Rough	130	1	10	15	7000	46
Dolomite	GelledAcid	Rough	Rough	130	0.5	20	15	1000	776
Dolomite	GelledAcid	Rough	Rough	130	0.5	20	15	1500	602
Dolomite	GelledAcid	Rough	Rough	130	0.5	20	15	2000	529
Dolomite	GelledAcid	Rough	Rough	130	0.5	20	15	2500	430
Dolomite	GelledAcid	Rough	Rough	130	0.5	20	15	4000	134
Dolomite	GelledAcid	Rough	Rough	130	0.5	20	15	5000	98

Dolomite	GelledAcid	Rough	Rough	130	0.5	20	15	6000	102
Dolomite	GelledAcid	Rough	Rough	130	0.5	20	15	7500	70
Dolomite	GelledAcid	Rough	Rough	130	1	10	15	1000	2664
Dolomite	GelledAcid	Rough	Rough	130	1	10	15	1500	1909
Dolomite	GelledAcid	Rough	Rough	130	1	10	15	2500	850
Dolomite	GelledAcid	Rough	Rough	130	1	10	15	3000	524
Dolomite	GelledAcid	Rough	Rough	130	1	10	15	4000	231
Dolomite	GelledAcid	Rough	Rough	130	1	10	15	5000	63
Dolomite	GelledAcid	Rough	Rough	130	1	10	15	6000	21
Dolomite	GelledAcid	Rough	Rough	130	1	10	15	0	2371
Dolomite	GelledAcid	Rough	Rough	130	1	10	15	500	772
Dolomite	GelledAcid	Rough	Rough	130	1	10	15	1000	366
Dolomite	GelledAcid	Rough	Rough	130	1	10	15	1500	175
Dolomite	GelledAcid	Rough	Rough	130	1	10	15	2500	55
Dolomite	GelledAcid	Rough	Rough	130	1	10	15	4000	1
Dolomite	GelledAcid	Rough	Rough	130	0.5	20	15	1000	900
Dolomite	GelledAcid	Rough	Rough	130	0.5	20	15	1500	377
Dolomite	GelledAcid	Rough	Rough	130	0.5	20	15	3000	343
Dolomite	GelledAcid	Rough	Rough	130	0.5	20	15	4000	329
Dolomite	GelledAcid	Rough	Rough	130	0.5	20	15	5000	260
Dolomite	GelledAcid	Rough	Rough	130	0.5	20	15	6000	138
Dolomite	GelledAcid	Rough	Rough	130	0.5	20	15	7000	69
Dolomite	GelledAcid	Rough	Rough	130	1	10	15	0	7486
Dolomite	GelledAcid	Rough	Rough	130	1	10	15	500	1938
Dolomite	GelledAcid	Rough	Rough	130	1	10	15	1500	738
Dolomite	GelledAcid	Rough	Rough	130	1	10	15	2500	219
Dolomite	GelledAcid	Rough	Rough	130	1	10	15	3500	65
Dolomite	GelledAcid	Rough	Rough	100	1	10	15	1000	181
Dolomite	GelledAcid	Rough	Rough	100	1	10	15	2000	60
Dolomite	GelledAcid	Rough	Rough	100	1	10	15	3000	28
Dolomite	X_linkedAcid	Rough	Rough	100	1	10	15	1000	1736
Dolomite	X_linkedAcid	Rough	Rough	100	1	10	15	2000	419
Dolomite	X_linkedAcid	Rough	Rough	100	1	10	15	3000	226
Dolomite	X_linkedAcid	Rough	Rough	100	1	10	15	4000	165
Dolomite	X_linkedAcid	Rough	Rough	100	1	10	15	5000	97
Dolomite	X_linkedAcid	Rough	Rough	100	1	10	15	6000	82
Dolomite	X_linkedAcid	Rough	Rough	100	1	10	15	7000	75
Dolomite	X_linkedAcid	Rough	Rough	130	1	10	15	1000	1754
Dolomite	X_linkedAcid	Rough	Rough	130	1	10	15	2000	426

Dolomite	X_linkedAcid	Rough	Rough	130	1	10	15	3000	222
Dolomite	X_linkedAcid	Rough	Rough	130	1	10	15	4000	166
Dolomite	X_linkedAcid	Rough	Rough	130	1	10	15	5000	98
Dolomite	X_linkedAcid	Rough	Rough	130	1	10	15	6000	82
Dolomite	X_linkedAcid	Rough	Rough	130	1	10	15	7000	73
Dolomite	GelledAcid	Rough	Rough	130	1	10	15	0	9704
Dolomite	GelledAcid	Rough	Rough	130	1	10	15	1000	6570
Dolomite	GelledAcid	Rough	Rough	130	1	10	15	2000	4096
Dolomite	GelledAcid	Rough	Rough	130	1	10	15	3000	4189
Dolomite	GelledAcid	Rough	Rough	130	1	10	15	4000	4189
Dolomite	GelledAcid	Rough	Rough	130	1	10	15	5000	3887
Dolomite	GelledAcid	Rough	Rough	130	1	10	15	6000	2592
Dolomite	GelledAcid	Rough	Rough	130	1	10	15	7000	1300
Dolomite	GelledAcid	Rough	Rough	130	1	10	15	1000	2838
Dolomite	GelledAcid	Rough	Rough	130	1	10	15	2000	1867
Dolomite	GelledAcid	Rough	Rough	130	1	10	15	3000	1777
Dolomite	GelledAcid	Rough	Rough	130	1	10	15	4000	1255
Dolomite	GelledAcid	Rough	Rough	130	1	10	15	5000	1157
Dolomite	GelledAcid	Rough	Rough	130	1	10	15	6000	979
Dolomite	GelledAcid	Rough	Rough	130	1	10	15	7000	742
Dolomite	GelledAcid	Rough	Rough	130	1	10	15	0	8125
Dolomite	GelledAcid	Rough	Rough	130	1	10	15	1000	225
Dolomite	GelledAcid	Rough	Rough	130	1	10	15	2000	30
Dolomite	GelledAcid	Rough	Rough	130	1	10	15	3000	12
Dolomite	GelledAcid	Rough	Rough	175	1	30	15	100	1995
Dolomite	GelledAcid	Rough	Rough	175	1	30	15	1000	2114
Dolomite	GelledAcid	Rough	Rough	175	1	30	15	2000	1823
Dolomite	GelledAcid	Rough	Rough	175	1	30	15	3000	1125
Dolomite	GelledAcid	Rough	Rough	175	1	30	15	4000	1114
Dolomite	GelledAcid	Rough	Rough	175	1	30	15	5000	43
Dolomite	GelledAcid	Rough	Rough	175	1	10	15	100	2220
Dolomite	GelledAcid	Rough	Rough	175	1	10	15	1000	2210
Dolomite	GelledAcid	Rough	Rough	175	1	10	15	2000	1779
Dolomite	GelledAcid	Rough	Rough	175	1	10	15	3000	206
Dolomite	GelledAcid	Rough	Rough	175	1	10	15	4000	206
Dolomite	GelledAcid	Rough	Rough	175	1	10	15	5000	55
Dolomite	GelledAcid	Rough	Rough	175	1	20	15	100	2792
Dolomite	GelledAcid	Rough	Rough	175	1	20	15	1000	4230
Dolomite	GelledAcid	Rough	Rough	175	1	20	15	2000	3959

Dolomite	GelledAcid	Rough	Rough	175	1	20	15	3000	3193
Dolomite	GelledAcid	Rough	Rough	175	1	20	15	4000	4468
Dolomite	GelledAcid	Rough	Rough	175	1	20	15	5000	2143
Dolomite	GelledAcid	Rough	Rough	175	1	30	15	100	1490
Dolomite	GelledAcid	Rough	Rough	175	1	30	15	1000	943
Dolomite	GelledAcid	Rough	Rough	175	1	30	15	2000	1019
Dolomite	GelledAcid	Rough	Rough	175	1	30	15	3000	808
Dolomite	GelledAcid	Rough	Rough	175	1	30	15	4000	122
Dolomite	GelledAcid	Rough	Rough	175	1	30	15	5000	151
Dolomite	GelledAcid	Rough	Rough	175	1	10	15	1000	20745
Dolomite	GelledAcid	Rough	Rough	175	1	10	15	2000	2447
Dolomite	GelledAcid	Rough	Rough	175	1	10	15	3000	2341
Dolomite	GelledAcid	Rough	Rough	175	1	10	15	4000	2097
Dolomite	GelledAcid	Rough	Rough	175	1	10	15	5000	1047
Dolomite	GelledAcid	Smooth	Rough	175	1	20	15	1000	4230
Dolomite	GelledAcid	Smooth	Rough	175	1	20	15	2000	3959
Dolomite	GelledAcid	Smooth	Rough	175	1	20	15	3000	3193
Dolomite	GelledAcid	Smooth	Rough	175	1	20	15	4000	4468
Dolomite	GelledAcid	Smooth	Rough	175	1	20	15	5000	2143
Dolomite	GelledAcid	Smooth	Rough	175	1	20	15	6000	141
Dolomite	GelledAcid	Smooth	Rough	175	1	30	15	1000	2745
Dolomite	GelledAcid	Smooth	Rough	175	1	30	15	2000	2447
Dolomite	GelledAcid	Smooth	Rough	175	1	30	15	3000	2341
Dolomite	GelledAcid	Smooth	Rough	175	1	30	15	4000	2097
Dolomite	GelledAcid	Smooth	Rough	175	1	30	15	5000	1047
Dolomite	GelledAcid	Smooth	Rough	175	1	30	15	6000	331
Dolomite	GelledAcid	Smooth	Rough	125	1	10	20	500	954
Dolomite	GelledAcid	Smooth	Rough	125	1	10	20	1000	349
Dolomite	GelledAcid	Smooth	Rough	125	1	10	20	2000	108
Dolomite	GelledAcid	Smooth	Rough	125	1	10	20	3000	73
Dolomite	GelledAcid	Smooth	Rough	125	1	10	20	4000	55
Dolomite	GelledAcid	Smooth	Rough	125	1	10	20	5000	46
Dolomite	GelledAcid	Smooth	Rough	125	1	10	20	6000	32
Dolomite	GelledAcid	Smooth	Rough	125	1	10	20	7000	24
Dolomite	Viscoelastic	Smooth	Uniform	200	1	20	15	1000	6765
Dolomite	Viscoelastic	Smooth	Uniform	200	1	20	15	2000	1020
Dolomite	Viscoelastic	Smooth	Uniform	200	1	20	15	3000	101
Dolomite	Viscoelastic	Smooth	Uniform	200	1	20	15	4000	73
Dolomite	Viscoelastic	Smooth	Uniform	200	1	30	15	1000	406

Dolomite	Viscoelastic	Smooth	Uniform	200	1	30	15	2000	288
Dolomite	Viscoelastic	Smooth	Uniform	200	1	30	15	3000	170
Dolomite	Viscoelastic	Smooth	Uniform	200	1	30	15	4000	66
Dolomite	Viscoelastic	Smooth	Uniform	200	1	30	15	5000	45
Limestone	GelledAcid	Rough	Channeling	175	1	20	15	100	1994
Limestone	GelledAcid	Rough	Channeling	175	1	20	15	1000	1208
Limestone	GelledAcid	Rough	Channeling	175	1	20	15	2000	523
Limestone	GelledAcid	Rough	Channeling	175	1	20	15	3000	266
Limestone	GelledAcid	Rough	Channeling	175	1	20	15	4000	191
Limestone	GelledAcid	Rough	Channeling	175	1	20	15	5000	55
Limestone	GelledAcid	Rough	Channeling	175	1	10	15	100	4314
Limestone	GelledAcid	Rough	Channeling	175	1	10	15	1000	48
Limestone	GelledAcid	Rough	Channeling	175	1	10	15	2000	38
Limestone	GelledAcid	Rough	Channeling	175	1	10	15	3000	31
Limestone	GelledAcid	Rough	Channeling	175	1	10	15	4000	15
Limestone	GelledAcid	Rough	Channeling	175	1	20	15	100	3736
Limestone	GelledAcid	Rough	Channeling	175	1	20	15	1000	3264
Limestone	GelledAcid	Rough	Channeling	175	1	20	15	2000	2709
Limestone	GelledAcid	Rough	Channeling	175	1	20	15	3000	3348
Limestone	GelledAcid	Rough	Channeling	175	1	20	15	4000	2484
Limestone	GelledAcid	Rough	Channeling	175	1	20	15	5000	644
Limestone	Emulsified	Smooth	Channeling	200	1	30	15	1000	4557
Limestone	Emulsified	Smooth	Channeling	200	1	30	15	2000	230
Limestone	Emulsified	Smooth	Channeling	200	1	30	15	3000	136
Limestone	Emulsified	Smooth	Channeling	200	1	30	15	4000	85
Limestone	Emulsified	Smooth	Channeling	200	1	30	15	5000	35
Limestone	Emulsified	Smooth	Channeling	200	1	60	15	1000	119
Limestone	Emulsified	Smooth	Channeling	200	1	60	15	2000	59
Limestone	Emulsified	Smooth	Channeling	200	1	60	15	3000	158
Limestone	Emulsified	Smooth	Channeling	200	1	60	15	4000	72
Limestone	Emulsified	Smooth	Channeling	200	1	60	15	5000	61
Limestone	Viscoelastic	Smooth	Channeling	200	1	15	15	1000	16838
Limestone	Viscoelastic	Smooth	Channeling	200	1	15	15	2000	12991
Limestone	Viscoelastic	Smooth	Channeling	200	1	15	15	3000	10189
Limestone	Viscoelastic	Smooth	Channeling	200	1	15	15	4000	7179
Limestone	Viscoelastic	Smooth	Channeling	200	1	15	15	5000	1903
Limestone	Viscoelastic	Smooth	Channeling	200	1	15	15	6000	38
Limestone	Viscoelastic	Smooth	Channeling	200	1	30	15	1000	34273
Limestone	Viscoelastic	Smooth	Channeling	200	1	30	15	2000	10606

Limestone	Viscoelastic	Smooth	Channeling	200	1	30	15	3000	1633
Limestone	Viscoelastic	Smooth	Channeling	200	1	30	15	4000	189
Limestone	Viscoelastic	Smooth	Channeling	200	1	30	15	5000	100
Limestone	GelledAcid	Smooth	Channeling	200	1	30	15	1000	14346
Limestone	GelledAcid	Smooth	Channeling	200	1	30	15	3000	12972
Limestone	GelledAcid	Smooth	Channeling	200	1	30	15	4000	2881
Limestone	GelledAcid	Smooth	Channeling	200	1	30	15	5000	402
Limestone	GelledAcid	Smooth	Channeling	200	1	60	15	1000	72483
Limestone	GelledAcid	Smooth	Channeling	200	1	60	15	2000	10739
Limestone	GelledAcid	Smooth	Channeling	200	1	60	15	3000	2201
Limestone	GelledAcid	Smooth	Channeling	200	1	60	15	4000	256
Limestone	GelledAcid	Smooth	Channeling	200	1	60	15	5000	98
Limestone	Viscoelastic	Smooth	Channeling	200	1	15	15	1000	16838
Limestone	Viscoelastic	Smooth	Channeling	200	1	15	15	2000	12991
Limestone	Viscoelastic	Smooth	Channeling	200	1	15	15	3000	10489
Limestone	Viscoelastic	Smooth	Channeling	200	1	15	15	4000	7179
Limestone	Viscoelastic	Smooth	Channeling	200	1	15	15	5000	1903
Limestone	Straight	Smooth	Channeling	140	1	20	20	1000	5656
Limestone	Straight	Smooth	Channeling	140	1	20	20	1500	1823
Limestone	Straight	Smooth	Channeling	140	1	20	20	2000	1089
Limestone	Straight	Smooth	Channeling	140	1	20	20	2500	800
Limestone	Straight	Smooth	Channeling	140	1	20	20	3000	738
Limestone	Straight	Smooth	Channeling	140	1	20	20	3500	291
Limestone	Straight	Smooth	Channeling	140	1	20	20	4000	193
Limestone	Straight	Smooth	Channeling	140	1	20	20	4500	132
Limestone	Straight	Smooth	Channeling	140	1	20	20	5000	86
Limestone	Straight	Smooth	Channeling	140	1	20	20	5500	59
Limestone	Straight	Smooth	Channeling	140	1	20	20	6000	40
Limestone	Viscoelastic	Smooth	Channeling	140	1	20	15	1000	13676
Limestone	Viscoelastic	Smooth	Channeling	140	1	20	15	1500	6141
Limestone	Viscoelastic	Smooth	Channeling	140	1	20	15	2000	2184
Limestone	Viscoelastic	Smooth	Channeling	140	1	20	15	2500	898
Limestone	Viscoelastic	Smooth	Channeling	140	1	20	15	3000	616
Limestone	Viscoelastic	Smooth	Channeling	140	1	20	15	3500	482
Limestone	Viscoelastic	Smooth	Channeling	140	1	20	15	4000	355
Limestone	Viscoelastic	Smooth	Channeling	140	1	20	15	4500	173
Limestone	Viscoelastic	Smooth	Channeling	140	1	20	15	5000	81
Limestone	Viscoelastic	Smooth	Channeling	140	1	20	15	5500	52
Limestone	Viscoelastic	Smooth	Channeling	140	1	20	15	6000	30

Limestone	GelledAcid	Smooth	Channeling	140	1	20	15	1000	3017
Limestone	GelledAcid	Smooth	Channeling	140	1	20	15	1500	2303
Limestone	GelledAcid	Smooth	Channeling	140	1	20	15	2000	1462
Limestone	GelledAcid	Smooth	Channeling	140	1	20	15	2500	1428
Limestone	GelledAcid	Smooth	Channeling	140	1	20	15	3000	904
Limestone	GelledAcid	Smooth	Channeling	140	1	20	15	3500	367
Limestone	GelledAcid	Smooth	Channeling	140	1	20	15	4000	190
Limestone	GelledAcid	Smooth	Channeling	140	1	20	15	4500	54
Limestone	GelledAcid	Smooth	Channeling	140	1	20	15	5000	50
Limestone	GelledAcid	Smooth	Channeling	140	1	20	15	5500	42
Limestone	GelledAcid	Smooth	Channeling	140	1	20	15	6000	31
Limestone	GelledAcid	Rough	Rough	175	1	10	15	1000	2987
Limestone	GelledAcid	Rough	Rough	175	1	10	15	3000	119
Limestone	GelledAcid	Rough	Rough	175	1	10	15	4000	6
Limestone	GelledAcid	Rough	Rough	175	1	10	15	5000	4
Limestone	GelledAcid	Rough	Rough	175	1	30	15	100	3088
Limestone	GelledAcid	Rough	Rough	175	1	30	15	1000	1352
Limestone	GelledAcid	Rough	Rough	175	1	30	15	2000	248
Limestone	GelledAcid	Rough	Rough	175	1	30	15	3000	44
Limestone	GelledAcid	Rough	Rough	175	1	30	15	4000	42
Limestone	GelledAcid	Rough	Rough	175	1	30	15	5000	72
Limestone	Emulsified	Smooth	Rough	200	1	15	15	1000	1597
Limestone	Emulsified	Smooth	Rough	200	1	15	15	2000	651
Limestone	Emulsified	Smooth	Rough	200	1	15	15	3000	512
Limestone	Emulsified	Smooth	Rough	200	1	15	15	4000	304
Limestone	Emulsified	Smooth	Rough	200	1	15	15	5000	48
Limestone	Emulsified	Smooth	Rough	275	1	15	15	1000	57962
Limestone	Emulsified	Smooth	Rough	275	1	15	15	2000	7117
Limestone	Emulsified	Smooth	Rough	275	1	15	15	3000	12498
Limestone	Emulsified	Smooth	Rough	275	1	15	15	4000	2136
Limestone	Emulsified	Smooth	Rough	275	1	15	15	5000	969
Limestone	GelledAcid	Smooth	Rough	175	1	5	15	100	18711
Limestone	GelledAcid	Smooth	Rough	175	1	5	15	1000	8696
Limestone	GelledAcid	Smooth	Rough	175	1	5	15	2000	4890
Limestone	GelledAcid	Smooth	Rough	175	1	5	15	3000	5180
Limestone	GelledAcid	Smooth	Rough	175	1	5	15	4000	103
Limestone	GelledAcid	Smooth	Rough	175	1	10	15	1000	2987
Limestone	GelledAcid	Smooth	Rough	175	1	10	15	3000	119
Limestone	GelledAcid	Smooth	Rough	175	1	10	15	4000	6

Limestone	GelledAcid	Smooth	Rough	175	1	15	15	100	14579
Limestone	GelledAcid	Smooth	Rough	175	1	15	15	1000	3187
Limestone	GelledAcid	Smooth	Rough	175	1	15	15	2000	208
Limestone	GelledAcid	Smooth	Rough	175	1	15	15	3000	69
Limestone	GelledAcid	Smooth	Rough	175	1	15	15	4000	125
Limestone	GelledAcid	Smooth	Rough	175	1	15	15	5000	25
Limestone	GelledAcid	Smooth	Rough	175	1	20	15	100	1994
Limestone	GelledAcid	Smooth	Rough	175	1	20	15	1000	1208
Limestone	GelledAcid	Smooth	Rough	175	1	20	15	2000	523
Limestone	GelledAcid	Smooth	Rough	175	1	20	15	3000	266
Limestone	GelledAcid	Smooth	Rough	175	1	20	15	4000	191
Limestone	GelledAcid	Smooth	Rough	175	1	20	15	5000	55
Limestone	GelledAcid	Smooth	Rough	175	1	30	15	100	4314
Limestone	GelledAcid	Smooth	Rough	175	1	30	15	1000	45
Limestone	GelledAcid	Smooth	Rough	175	1	30	15	2000	38
Limestone	GelledAcid	Smooth	Rough	175	1	30	15	3000	31
Limestone	GelledAcid	Smooth	Rough	175	1	30	15	4000	15
Limestone	Emulsified	Smooth	Rough	185	1	30	15	100	1817
Limestone	Emulsified	Smooth	Rough	185	1	30	15	1000	1440
Limestone	Emulsified	Smooth	Rough	185	1	30	15	3000	862
Limestone	Emulsified	Smooth	Rough	185	1	30	15	4000	419
Limestone	Emulsified	Smooth	Rough	185	1	30	15	5000	208
Limestone	Emulsified	Smooth	Rough	185	1	30	15	6000	200
Limestone	GelledAcid	Smooth	Rough	185	1	20	15	100	2630
Limestone	GelledAcid	Smooth	Rough	185	1	20	15	1000	1370
Limestone	GelledAcid	Smooth	Rough	185	1	20	15	2000	978
Limestone	GelledAcid	Smooth	Rough	185	1	20	15	3000	425
Limestone	GelledAcid	Smooth	Rough	185	1	20	15	4000	256
Limestone	GelledAcid	Smooth	Rough	185	1	20	15	5000	136
Limestone	GelledAcid	Smooth	Rough	185	1	20	15	6000	122
Limestone	GelledAcid	Smooth	Rough	185	1	20	15	100	2149
Limestone	GelledAcid	Smooth	Rough	185	1	20	15	1000	767
Limestone	GelledAcid	Smooth	Rough	185	1	20	15	2000	619
Limestone	GelledAcid	Smooth	Rough	185	1	20	15	3000	265
Limestone	GelledAcid	Smooth	Rough	185	1	20	15	4000	213
Limestone	GelledAcid	Smooth	Rough	185	1	30	15	100	2596
Limestone	GelledAcid	Smooth	Rough	185	1	30	15	1000	1449
Limestone	GelledAcid	Smooth	Rough	185	1	30	15	2000	869
Limestone	GelledAcid	Smooth	Rough	185	1	30	15	3000	555

Limestone	GelledAcid	Smooth	Rough	185	1	30	15	4000	330
Limestone	GelledAcid	Smooth	Rough	185	1	30	15	5000	128
Limestone	GelledAcid	Smooth	Rough	185	1	30	15	6000	126
Limestone	Viscoelastic	Smooth	Rough	185	1	20	15	100	4847
Limestone	Viscoelastic	Smooth	Rough	185	1	20	15	1000	1692
Limestone	Viscoelastic	Smooth	Rough	185	1	20	15	2000	803
Limestone	Viscoelastic	Smooth	Rough	185	1	20	15	3000	680
Limestone	Viscoelastic	Smooth	Rough	185	1	20	15	4000	277
Limestone	Viscoelastic	Smooth	Rough	185	1	20	15	5000	129
Limestone	Viscoelastic	Smooth	Rough	185	1	20	15	100	3010
Limestone	Viscoelastic	Smooth	Rough	185	1	20	15	1000	2590
Limestone	Viscoelastic	Smooth	Rough	185	1	20	15	2000	2510
Limestone	Viscoelastic	Smooth	Rough	185	1	20	15	3000	4250
Limestone	Viscoelastic	Smooth	Rough	185	1	20	15	4000	10
Limestone	Emulsified	Smooth	Rough	200	1	15	28	1000	1597
Limestone	Emulsified	Smooth	Rough	200	1	15	28	2000	651
Limestone	Emulsified	Smooth	Rough	200	1	15	28	3000	512
Limestone	Emulsified	Smooth	Rough	200	1	15	28	4000	304
Limestone	Emulsified	Smooth	Rough	200	1	15	28	5000	48
Limestone	Emulsified	Smooth	Rough	200	1	30	28	1000	4557
Limestone	Emulsified	Smooth	Rough	200	1	30	28	2000	230
Limestone	Emulsified	Smooth	Rough	200	1	30	28	3000	136
Limestone	Emulsified	Smooth	Rough	200	1	30	28	4000	85
Limestone	Emulsified	Smooth	Rough	200	1	30	28	5000	35
Limestone	Emulsified	Smooth	Rough	200	1	60	28	3000	158
Limestone	Emulsified	Smooth	Rough	200	1	60	28	4000	72
Limestone	Emulsified	Smooth	Rough	200	1	60	28	5000	61
Limestone	GelledAcid	Smooth	Rough	200	1	15	15	1000	2823
Limestone	GelledAcid	Smooth	Rough	200	1	15	15	2000	1133
Limestone	GelledAcid	Smooth	Rough	200	1	15	15	3000	937
Limestone	GelledAcid	Smooth	Rough	200	1	15	15	4000	397
Limestone	GelledAcid	Smooth	Rough	200	1	15	15	5000	104
Limestone	Emulsified	Smooth	Rough	200	1	15	28	1000	57962
Limestone	Emulsified	Smooth	Rough	200	1	15	28	3000	12498
Limestone	Emulsified	Smooth	Rough	200	1	15	28	4000	2136
Limestone	Emulsified	Smooth	Rough	200	1	15	28	5000	969
Limestone	Emulsified	Smooth	Rough	200	1	30	28	1000	57721
Limestone	Emulsified	Smooth	Rough	200	1	30	28	2000	5948
Limestone	Emulsified	Smooth	Rough	200	1	30	28	3000	5349

Limestone	Emulsified	Smooth	Rough	200	1	30	28	4000	1494
Limestone	Emulsified	Smooth	Rough	200	1	30	28	5000	262
Limestone	Emulsified	Smooth	Rough	200	1	60	28	2000	2296
Limestone	Emulsified	Smooth	Rough	200	1	60	28	3000	2383
Limestone	Emulsified	Smooth	Rough	200	1	60	28	4000	548
Limestone	Emulsified	Smooth	Rough	200	1	60	28	5000	174
Limestone	GelledAcid	Smooth	Rough	150	1	10	20	1000	4919
Limestone	GelledAcid	Smooth	Rough	150	1	10	20	2000	1630
Limestone	GelledAcid	Smooth	Rough	150	1	10	20	3000	597
Limestone	GelledAcid	Smooth	Rough	150	1	10	20	4000	350
Limestone	GelledAcid	Smooth	Rough	150	1	10	20	5000	198
Limestone	GelledAcid	Smooth	Rough	150	1	10	20	6000	112
Limestone	GelledAcid	Smooth	Rough	150	1	10	20	7000	72
Limestone	GelledAcid	Smooth	Rough	125	1	10	20	500	7350
Limestone	GelledAcid	Smooth	Rough	125	1	10	20	1000	4024
Limestone	GelledAcid	Smooth	Rough	125	1	10	20	2000	1166
Limestone	GelledAcid	Smooth	Rough	125	1	10	20	3000	387
Limestone	GelledAcid	Smooth	Rough	125	1	10	20	4000	268
Limestone	GelledAcid	Smooth	Rough	125	1	10	20	5000	98
Limestone	GelledAcid	Smooth	Rough	125	1	10	20	6000	41
Limestone	GelledAcid	Smooth	Rough	125	1	10	20	7000	16
Limestone	GelledAcid	Smooth	Rough	125	1	10	20	500	2693
Limestone	GelledAcid	Smooth	Rough	125	1	10	20	1000	1128
Limestone	GelledAcid	Smooth	Rough	125	1	10	20	2000	157
Limestone	GelledAcid	Smooth	Rough	125	1	10	20	3000	42
Limestone	GelledAcid	Smooth	Rough	125	1	10	20	4000	25
Limestone	GelledAcid	Smooth	Rough	125	1	10	20	5000	15
Limestone	GelledAcid	Smooth	Rough	125	1	10	20	6000	7
Limestone	GelledAcid	Smooth	Rough	125	1	10	20	7000	3
Limestone	GelledAcid	Smooth	Rough	125	1	10	20	500	2268
Limestone	GelledAcid	Smooth	Rough	125	1	10	20	1000	120
Limestone	GelledAcid	Smooth	Rough	125	1	10	20	2000	101
Limestone	GelledAcid	Smooth	Rough	125	1	10	20	3000	57
Limestone	GelledAcid	Smooth	Rough	125	1	10	20	4000	42
Limestone	GelledAcid	Smooth	Rough	125	1	10	20	5000	36
Limestone	GelledAcid	Smooth	Rough	125	1	10	20	6000	27
Limestone	GelledAcid	Smooth	Rough	125	1	10	20	7000	20
Limestone	Straight	Smooth	Turbulence	175	1	5	15	100	14354
Limestone	Straight	Smooth	Turbulence	175	1	5	15	1000	8375

Limestone	Straight	Smooth	Turbulence	175	1	5	15	2000	4607
Limestone	Straight	Smooth	Turbulence	175	1	5	15	3000	1010
Limestone	Straight	Smooth	Turbulence	175	1	5	15	4000	172
Limestone	Straight	Smooth	Turbulence	175	1	10	15	1000	26056
Limestone	Straight	Smooth	Turbulence	175	1	10	15	2000	14037
Limestone	Straight	Smooth	Turbulence	175	1	10	15	3000	12696
Limestone	Straight	Smooth	Turbulence	175	1	10	15	4000	5476
Limestone	Straight	Smooth	Turbulence	175	1	10	15	5000	174
Limestone	Straight	Smooth	Turbulence	175	1	10	15	6000	112
Limestone	Straight	Smooth	Turbulence	175	1	15	15	1000	1367
Limestone	Straight	Smooth	Turbulence	175	1	15	15	2000	1244
Limestone	Straight	Smooth	Turbulence	175	1	15	15	3000	807
Limestone	Straight	Smooth	Turbulence	175	1	15	15	4000	401
Limestone	Straight	Smooth	Turbulence	175	1	15	15	5000	139
Limestone	Straight	Smooth	Turbulence	175	1	15	15	6000	74
Limestone	Straight	Smooth	Turbulence	175	1	20	15	100	2069
Limestone	Straight	Smooth	Turbulence	175	1	20	15	1000	236
Limestone	Straight	Smooth	Turbulence	175	1	20	15	2000	19
Limestone	Straight	Smooth	Turbulence	185	1	20	15	1000	967
Limestone	Straight	Smooth	Turbulence	185	1	20	15	2000	594
Limestone	Straight	Smooth	Turbulence	185	1	20	15	3000	460
Limestone	Straight	Smooth	Turbulence	185	1	20	15	4000	169
Limestone	Straight	Smooth	Turbulence	185	1	20	15	5000	162
Limestone	Straight	Smooth	Turbulence	185	1	20	15	6000	112
Limestone	Straight	Smooth	Turbulence	185	1	20	15	1000	3132
Limestone	Straight	Smooth	Turbulence	185	1	20	15	2000	2050
Limestone	Straight	Smooth	Turbulence	185	1	20	15	3000	21
Limestone	Straight	Smooth	Turbulence	185	1	30	15	1000	407
Limestone	Straight	Smooth	Turbulence	185	1	30	15	2000	323
Limestone	Straight	Smooth	Turbulence	185	1	30	15	3000	111
Limestone	Straight	Smooth	Turbulence	185	1	30	15	4000	98
Limestone	Emulsified	Smooth	Uniform	275	1	30	15	1000	57721
Limestone	Emulsified	Smooth	Uniform	275	1	30	15	2000	5948
Limestone	Emulsified	Smooth	Uniform	275	1	30	15	3000	5349
Limestone	Emulsified	Smooth	Uniform	275	1	30	15	4000	1494
Limestone	Emulsified	Smooth	Uniform	275	1	30	15	5000	262
Limestone	Emulsified	Smooth	Uniform	275	1	60	15	1000	411
Limestone	Emulsified	Smooth	Uniform	275	1	60	15	2000	2296
Limestone	Emulsified	Smooth	Uniform	275	1	60	15	3000	2383

Limestone	Emulsified	Smooth	Uniform	275	1	60	15	4000	548
Limestone	Emulsified	Smooth	Uniform	275	1	60	15	5000	174
Limestone	Viscoelastic	Smooth	Uniform	200	1	60	15	1000	36500
Limestone	Viscoelastic	Smooth	Uniform	200	1	60	15	2000	1910
Limestone	Viscoelastic	Smooth	Uniform	200	1	60	15	3000	461
Limestone	Viscoelastic	Smooth	Uniform	200	1	60	15	4000	127
Limestone	Viscoelastic	Smooth	Uniform	200	1	60	15	5000	104
Limestone	Viscoelastic	Smooth	Uniform	200	1	60	15	6000	20
Limestone	Viscoelastic	Smooth	Uniform	200	1	30	15	1000	34273
Limestone	Viscoelastic	Smooth	Uniform	200	1	30	15	2000	10606
Limestone	Viscoelastic	Smooth	Uniform	200	1	30	15	3000	1633
Limestone	Viscoelastic	Smooth	Uniform	200	1	30	15	4000	189
Limestone	Viscoelastic	Smooth	Uniform	200	1	30	15	5000	100
Limestone	Viscoelastic	Smooth	Uniform	200	1	60	15	1000	36500
Limestone	Viscoelastic	Smooth	Uniform	200	1	60	15	2000	1910
Limestone	Viscoelastic	Smooth	Uniform	200	1	60	15	3000	461
Limestone	Viscoelastic	Smooth	Uniform	200	1	60	15	4000	127
Limestone	Viscoelastic	Smooth	Uniform	200	1	60	15	5000	104
Limestone	Straight	Smooth	Uniform	140	1	20	15	1000	890
Limestone	Straight	Smooth	Uniform	140	1	20	15	1500	396
Limestone	Straight	Smooth	Uniform	140	1	20	15	2000	196
Limestone	Straight	Smooth	Uniform	140	1	20	15	2500	106

Vitae

Name	Mahmoud Hassan Desouky
Nationality	Egyptian
Date of Birth	5/28/1991
Email	mahmoudhassan1001@yahoo.com
Address	Qalubia, Greater Cairo, Egypt
Postal Code	13754
Academic Background	Master of Science in Petroleum Engineering
Research Interests	Fracturing, Reservoir Engineering and Machine Learning
Publications	Aljawad, M. S., Aljulaih, H., Hughes, B., & Desouky, M. (2019). Integration of field, laboratory, and modeling aspects of acid fracturing: A comprehensive review. *Journal of Petroleum Science and Engineering*. https://doi.org/10.1016/j.petrol.2019.06.022
Educational Background	MSc. Petroleum Engineering – 2019 King Fahd University of Petroleum & Minerals, Saudi Arabia. B.E Petroleum Engineering – 2013 Suez University, Egypt.